



HAL
open science

Interplay between magnetic ordering and ferroelectricity in multiferroics with quadruple perovskite structure

Marine Verseils

► To cite this version:

Marine Verseils. Interplay between magnetic ordering and ferroelectricity in multiferroics with quadruple perovskite structure. Physics [physics]. Université Pierre et Marie Curie - Paris VI; Università degli studi (Parma, Italie), 2017. English. NNT: 2017PA066457. tel-01798069

HAL Id: tel-01798069

<https://theses.hal.science/tel-01798069>

Submitted on 23 May 2018

HAL is a multi-disciplinary open access archive for the deposit and dissemination of scientific research documents, whether they are published or not. The documents may come from teaching and research institutions in France or abroad, or from public or private research centers.

L'archive ouverte pluridisciplinaire **HAL**, est destinée au dépôt et à la diffusion de documents scientifiques de niveau recherche, publiés ou non, émanant des établissements d'enseignement et de recherche français ou étrangers, des laboratoires publics ou privés.



UNIVERSITÀ
ITALIANO
FRANCESE



UNIVERSITÉ PIERRE ET MARIE CURIE
UNIVERSITÀ DEGLI STUDI DI PARMA

Ecole Doctorale 397: Physique et chimie des matériaux

PH.D THESIS in PHYSICS

Presented by Marine VERSEILS on Thursday, October 19th, 2017

Interplay between magnetic ordering and ferroelectricity in multiferroics with quadruple perovskite structure

Jury

Isabelle Mirebeau (Research Director) - LLB (CEA-CNRS) - *Reviewer*

Maxim Mostovoy (Professor) - University of Groningen - *Reviewer*

Valia Voliotis (Professor) - Institut des Nanosciences de Paris (UPMC) - *Examiner*

Gianluca Calestani (Professor) - Chemistry Department (Parma Univ.) - *Examiner*

Andrea Gauzzi (Professor) - IMPMC/UPMC - *Director*

Edi Gilioli (Researcher) - IMEM-CNR (Parma) - *Co-director*

Abstract

In the present Thesis, we address the open issue of the unusually large ferroelectricity induced by magnetism, recently reported in $(AMn_3)Mn_4O_{12}$ quadruple perovskites. To do so, we focus our study on the isostructural and isoelectronic compounds $(LaMn_3)Mn_4O_{12}$ (LMO) and $(Y Mn_3)Mn_4O_{12}$ (YMO), for they display single-valent Mn^{3+} properties and a commensurate C -type antiferromagnetic structure of the B -site Mn^{3+} ions. These simple features offer an ideal playground to elucidate the controversial contribution of the exchange striction and of the antisymmetric exchange to the electric polarization. YMO and LMO are both metastable phases stabilized under high-pressure; YMO is a new phase, not reported before, where the comparatively small Y^{3+} ion exerts a large chemical pressure, which is expected to enhance the exchange interaction and, thus, the spontaneous polarization, as compared to LMO.

According to this expectation, in YMO we find an ordering temperature, $T_{N,B} = 108$ K, of the B -sites, 30 K higher than in LMO. On the other hand, we surprisingly find identical values of the spontaneous polarization, $P = 0.54 \mu C cm^{-2}$, in both compounds. To the best of our knowledge, this is a record value for magnetic ferroelectrics, two times larger than the previous record value reported in $(CaMn_3)Mn_4O_{12}$. This result is very promising for multiferroic applications considering that it is obtained in polycrystalline samples and 6-10 times larger values are expected in single crystals of epitaxial films.

In spite of the similar structural and electronic properties and the identical polarization found, the properties of magnetic ferroelectricity appear to be very different in the two compounds. Namely, in LMO, ferroelectricity occurs at the magnetic transition at $T_{N,B}=78$ K, although no indication of inversion symmetry breaking is detected either by x-ray diffraction or by a combined Raman and IR study. We argue that this puzzling observation is consistent with Levanyuk and Sannikov' prediction of domain structure corresponding to degenerate solutions of the multi-component order parameter, which is characteristic of improper ferroelectrics. On the other hand, in YMO, the observation of ferroelectricity at $T^*=70$ K is consistent with a polar structural modulation below $T_s=200$ K, however T^* does not correspond to any long-range magnetic order. Indeed, the ordering of the B -sites occurs well above, at $T_{N,B}=108$ K, while T^* marks a magnetic anomaly consistent with short-range magnetic correlations and suggesting a latent magnetic phase. We put forward the hypothesis that the above polar distortion of the crystal structure occurring at T_s may force the alignment of polar domains that would be otherwise randomly oriented because of the random orientation of the magnetic domains.

The above results prompt us to carry out further work that may: (i) lead to the achievement of even larger polarizations well above $1 \mu C cm^{-2}$ in single crystals or epitaxial films, which is a prerequisite of multiferroic applications; (ii) provide further hints as to the role of polar and magnetic domains and of short-range magnetic correlations in the stabilization of such large polarizations in improper ferroelectrics.

Résumé

Cette Thèse traite de la question ouverte de la ferroélectricité magnétiquement induite dans les pérovskites quadruples de manganèse $(AMn_3)Mn_4O_{12}$. Notre étude se concentre sur deux composés isostructuraux et isoélectroniques $(LaMn_3)Mn_4O_{12}$ (LMO) et $(YMn_3)Mn_4O_{12}$ (YMO) qui possèdent une monovalence Mn^{3+} ainsi qu'une structure antiferromagnétique commensurable de type C des sites B . Ces caractéristiques simples, par rapport à d'autres composés de la même famille, font de ces composés des systèmes modèles pour élucider la controverse autour de la contribution des interactions d'échange symétrique et/ou antisymétrique à la polarisation. YMO et LMO sont des composés métastables, stabilisés grâce à la haute pression, et YMO est une nouvelle phase dans laquelle l'ion Y^{3+} , relativement petit par rapport au La^{3+} exerce une forte pression chimique censée augmenter l'interaction d'échange et par conséquent la polarisation spontanée du système.

Comme attendu, nous avons trouvé dans YMO une température d'orientation magnétique des sites B , $T_{N,B} = 108$ K, supérieure de 30 degrés à celle reportée dans LMO. En revanche, de façon surprenante, nous avons mesuré une valeur de la polarisation, $P = 0.54 \mu C \text{ cm}^{-2}$, identique dans les deux composés. Il s'agit d'une valeur record dans les ferroélectriques magnétiques puisqu'elle est deux fois plus grande que la précédente valeur record reportée dans $(CaMn_3)Mn_4O_{12}$. Ce résultat est très prometteur dans la mesure où il a été obtenu avec des polycristaux et que des valeurs 6 à 10 fois plus grandes sont attendues dans des mono-cristaux ou des couches minces. En dépit d'une structure et de propriétés électroniques similaires, ainsi que d'une même valeur de P , les propriétés de ferroélectricité magnétique semblent très différentes dans les deux composés. Plus précisément, dans LMO, la ferroélectricité apparaît à la transition magnétique des sites B , à $T_{N,B} = 78$ K bien qu'aucune indication de brisure du centre d'inversion n'ait pu être reportée par diffraction de rayons X ou par spectroscopie Raman et infrarouge. Nous montrons que ce résultat inattendu est en accord avec la théorie de Levanyuk et Sannikov, qui prévoit l'apparition d'une structure de domaines polarisés du fait de la dégénérescence des solutions pour le paramètre d'ordre dans le cas des ferroélectriques impropres. D'un autre côté, l'observation de la ferroélectricité à $T^* = 70$ K dans YMO est cohérente avec la modulation structurale apparaissant à $T_s = 200$ K. Cependant, T^* ne correspond pas à l'apparition d'un ordre magnétique à longue portée. En effet, l'orientation des sites B a lieu bien plus haut, à $T_{N,B} = 108$ K, et à T^* il apparaît seulement une anomalie magnétique qui peut être expliquée par des corrélations magnétiques, ce qui suggère l'existence d'un ordre magnétique latent. Nous émettons l'hypothèse que la distorsion polaire de la structure qui a lieu à T_s est responsable de l'alignement des domaines ferroélectriques qui seraient sans cela aléatoirement orientés du fait de l'absence d'orientation à longue portée des domaines magnétiques.

Nos résultats nous poussent à poursuivre l'étude de ces composés pour donner un éclairage sur le rôle des domaines polaires et magnétiques ainsi que celui des corrélations magnétiques à courte portée dans le mécanisme d'apparition d'une forte P dans certains

ferroélectriques impropres.

Riassunto

La presente Tesi tratta della ferroelettricità indotta dal magnetismo nelle perovskiti quaduple $(AMn_3)Mn_4O_{12}$. Il nostro lavoro si concentra sui due composti isostrutturali e isoelettronici $(LaMn_3)Mn_4O_{12}$ (LMO) e $(YMn_3)Mn_4O_{12}$ (YMO). Entrambi sono monovalenti Mn^{3+} e presentano una struttura antiferromagnetica e commensurata di tipo C dei siti B . Queste caratteristiche semplici rispetto a quelle di altri composti della stessa famiglia fanno di LMO e YMO due sistemi ideali per chiarire il contributo controverso delle interazioni di scambio simmetrica e antisimmetrica alla polarizzazione elettrica. LMO e YMO sono fasi metastabili stabilizzate sotto alta pressione; YMO è una nuova fase nella quale la dimensione ridotta dello ione Y^{3+} , rispetto a La^{3+} , esercita una pressione chimica notevole. Ci si attende che questo fatto causi un aumento significativo dell'interazione di scambio e dunque della polarizzazione elettrica spontanea indotta dal magnetismo.

Come previsto, in YMO la temperatura d'ordine dei siti B , $T_{N,B} = 108$ K, risulta essere più alta di 30 gradi rispetto a quella di LMO. D'altra parte, abbiamo misurato lo stesso valore di polarizzazione, $P = 0.54 \mu C cm^{-2}$, nei due composti. A nostra conoscenza, si tratta del valore più alto mai riportato in letteratura nei ferroelettrici impropri, due volte maggiore del valore record precedentemente riportato in $(CaMn_3)Mn_4O_{12}$. Questo risultato è particolarmente promettente considerando che è stato ottenuto in campioni policristallini; quindi dei valori 6 a 10 volte più alti sono attesi in campioni monocristallini o in film epitassiali.

È sorprendente che i due composti presentino proprietà magnetiche completamente diverse nonostante la struttura cristallina, le proprietà elettroniche e il valore della polarizzazione spontanea, P , siano identiche. In LMO, la ferroelettricità è indotta dalla transizione magnetica dei siti B , a $T_{N,B} = 78$ K; purtroppo, non abbiamo trovato traccia di rottura del centro d'inversione né per diffrazione dei raggi x o neutroni, né per spettroscopia Raman o infrarossa. La nostra analisi indica che questo risultato sorprendente è spiegato dalla previsione di una struttura a domini della teoria fenomenologica sviluppata da Levanyuk e Sannikov per i ferroelettrici impropri. Una tale struttura è dovuta all'esistenza di soluzioni degeneri per il parametro d'ordine multi-componente. D'altra parte, l'osservazione della ferroelettricità a $T^* = 70$ K in YMO è coerente con l'osservazione di una modulazione strutturale a $T_s = 200$ K. Invece, T^* non corrisponde a nessun ordine magnetico a lungo raggio che avviene a temperatura ben più alta ($T_{N,B} = 108$ K) per i siti B . A T^* si nota però un'anomalia magnetica che indica un ordine magnetico latente. Proponiamo quindi che la distorsione polare della struttura a T_s conduca all'allineamento dei domini ferroelettrici che sarebbero altrimenti orientati in modo casuale a causa dell'assenza d'ordinamento a lungo raggio dei domini magnetici.

I risultati susposti ci stimolano a proseguire lo studio fin qui svolto al fine di chiarire il ruolo dei domini polari e magnetici e delle correlazioni magnetiche a corto raggio sul meccanismo della ferroelettricità impropria.

Contents

Abstract	3
Résumé	4
Riassunto	6
1 Introduction	12
1.1 Generalities about magnetoelectric multiferroics	14
1.2 Magnetically induced ferroelectricity	15
1.2.1 Classification of multiferroics	15
1.2.2 Phenomenological theory	17
1.2.3 Microscopic theories	18
1.3 $(AMn_3)Mn_4O_{12}$ quadruple perovskites	21
1.3.1 Open questions and strategy for the Thesis	23
2 Experimental methods	28
2.1 High-pressure/high-temperature syntheses	29
2.2 Diffraction techniques	33
2.3 Thermodynamics measurements	34
2.3.1 Transport properties	34
2.3.2 Magnetization	36
2.3.3 Heat capacity	36
2.4 Spectroscopy techniques	38
2.4.1 Difference between Infrared and Raman spectroscopy	38
2.4.2 Sample preparation for spectroscopy	40

2.4.3	Fourier Transform InfraRed (FTIR) Spectrometer	41
2.4.4	Triple-stage Raman spectrometer	43
2.5	Ferroelectric characterizations	45
2.5.1	Pyroelectric currents	45
2.5.2	Dielectric constant	46
3	Multiferroic properties of (LaMn₃)Mn₄O₁₂	48
3.1	Introduction	48
3.2	Article I: Large ferroelectricity induced by collinear magnetism in the quadruple perovskite (LaMn ₃)Mn ₄ O ₁₂	50
	<i>Fig. 3.1 Cell-parameters vs temperature</i>	54
	<i>Fig. 3.2 Pyrocurrents vs Temperature</i>	55
	<i>Fig. 3.3 Remnant polarization vs T</i>	56
	<i>Fig. 3.4 Magnetoelectric coupling measurements</i>	57
4	Raman and IR spectroscopy study of the spin-lattice coupling in (LaMn₃)Mn₄O₁₂	62
4.1	Introduction	62
4.2	Article II: Evidence of strong magnetoelastic coupling driving magnetic ferroelectricity	63
	<i>Fig 4.1 Infrared spectra</i>	69
	<i>Fig 4.2 Raman spectrum</i>	70
	<i>Fig 4.3 Infrared frequencies vs temperature</i>	73
	<i>Fig 4.4 Raman frequencies vs temperature</i>	75
	<i>Fig 4.5 Dielectric constant vs frequency</i>	77
	<i>Fig 4.6 Specific heat vs magnetic field</i>	78
5	Effect of the chemical pressure (La³⁺/Y³⁺ substitution)	80
5.1	Introduction	80
5.2	Article III: Effect of chemical pressure induced by the La ³⁺ /Y ³⁺ substitution on the magnetic ordering of (AMn ₃)Mn ₄ O ₁₂ quadruple perovskites	81
5.3	Supplementary information on article III	102

6	Multiferroic properties of the new quadruple perovskite $(\text{YMn}_3)\text{Mn}_4\text{O}_{12}$	106
6.1	Motivations	106
6.2	Article IV: Evidence of centrosymmetry breaking in the magnetic ferro- electric $(\text{YMn}_3)\text{Mn}_4\text{O}_{12}$	107
	<i>Fig. 6.1 Pyroelectric currents vs temperature</i>	112
	<i>Fig. 6.2 Remnant polarization vs temperature</i>	113
	<i>Fig. 6.3 Remnant polarization vs poling electric field</i>	114
	<i>Fig. 6.4 Capacitance vs temperature</i>	115
	<i>Fig. 6.5 Electrical resistivity vs temperature</i>	116
	<i>Fig. 6.6 Single-crystal diffraction patterns</i>	117
	<i>Fig. 6.7 Scheme of the super-cell</i>	117
	Conclusions and perspectives	122
	Bibliography	128

Chapter 1

Introduction

The history of humanity is intimately linked to materials used in common life, to such an extent that prehistorical periods (stone-, bronze-, iron-ages) are named after materials that drove technology towards new directions. More recently, steel and silicon marked the novel technologies of the 19th and 20th centuries.

Nowadays, the need for novel functional materials is of increasing importance for future technological developments, especially in the energy and electronics sectors. The broad context of the present Thesis concerns the possibility of realizing novel concepts of electronic devices, such as magnetic memories, where magnetic domains are manipulated by an electric field, or viceversa. This would open the field towards the development of fast and low-power consumption nonvolatile memories (see figure 1.1). Actually, the performance of the electronic devices used in our daily life would be greatly enhanced if the same memory used for data processing could serve also for data storage. It is recalled that, at present, non-volatile memories, such as magnetic disks or MOSFET-based memories, are much slower than volatile RAM memories and also dissipate a significant amount of energy due to the generation of magnetic field, the mechanical motion of the disk and the biasing of the gate during the reading/writing process.

In this context, magnetoelectric materials, where magnetic and electric orders are coupled, have attracted a great deal of interest. Two routes towards the effective magnetoelectric materials have been hitherto considered: i) piezoelectric/magnetostrictive (or ferroelectric/magnetostrictive) composites. ii) single-phase materials exhibiting both ferroelectric and magnetic orders, called multiferroics. In the latter case, the chal-

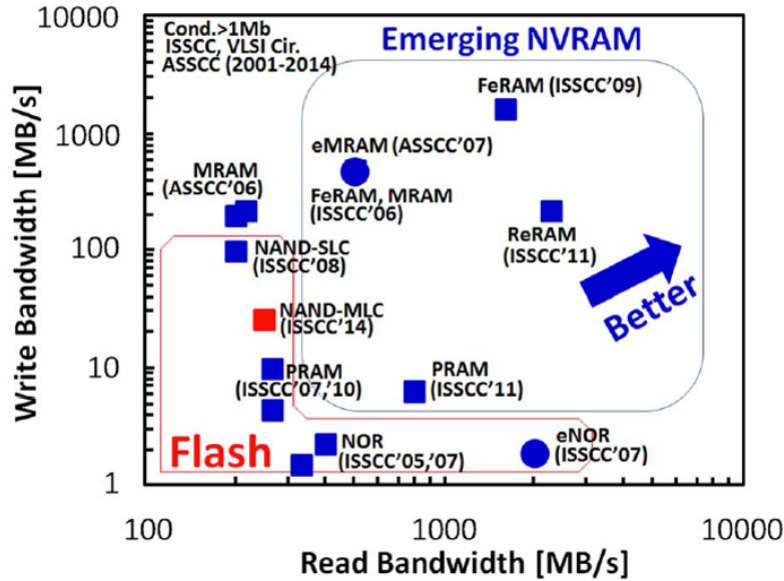


Figure 1.1: Electronic devices for data storage as a function of speed of writing and reading. Illustration from International Solid State Circuit conference 2014 with permission.

lenge is to develop materials with an effective tunability of the magnetization by an electric field. This requires both, a sizable electric polarization P and a large magnetoelectric coupling, which is defined as a generalized susceptibility $\alpha = \partial P / \partial H$. At present, no multiferroic material meets both requirements, so the search for new materials is an active research direction. The aim of the present Thesis is to contribute to the understanding of the structure-property relationships in multiferroic materials, which is required to master the multiferroic performances of these materials. Specifically, our strategy is to study novel metastable phases that display unusual structural and electronic characteristics not found in ordinary phases stable at ambient pressure conditions.

1.1 Generalities about magnetoelectric multiferroics

The possibility of magnetoelectricity in a crystalline phase, namely a coupling between remnant polarization P and remnant magnetization M , was predicted in 1894 by P. Curie [1]. Using symmetry arguments, the "magnetoelectric" term was later (1926) proposed by Debye. The effect remained a matter of scientific curiosity until 1960 when it was first reported in Cr_2O_3 by Astrov [2] following a theoretical prediction by Dzyaloshinskii [3]. Landau and Lifshitz proposed to account phenomenologically for the magnetoelectric effect by introducing an additional $-\alpha_{ij}E_iH_j$ term in the free energy, where α_{ij} is a tensor describing the strength of the magnetoelectric coupling [4]. More recently, the term "multiferroic" was introduced by H. Schmid in 1994 [5] to denote a more general category of materials displaying at least two ferroic orders, such as ferroelasticity, ferroelectricity or ferromagnetism.

The search of novel magnetoelectric multiferroics is challenging because of the following considerations. [6, 7]:

1. *Symmetry constraints*: ferroelectricity and magnetism require inversion- and time-reversal- symmetry breaking, respectively. It turns out that only a few of the 233 Shubnikov magnetic point groups meet both requirements. These groups are as follows: 1 , 2 , $2'$, m , m' , 3 , $3m'$, 4 , $4m'm'$, $m'm2'$, $m'm'2'$, 6 and $6m'm'$.
2. *Electronic constraints*: in transition metal (TM) oxides, ferroelectricity typically occurs in TMs with d^0 configuration, such as Ti^{1+} , Zr^{4+} and Nb^{5+}). This is explained by the fact that the ferroelectric distortion (off-centering shift of the TM cation) occurring at low temperature typically requires the hybridization of the TM d orbitals with the oxygen $2p$ orbitals; this hybridization is stronger for d orbitals close to the oxygen $2p$, which occurs in the case of the d^0 configuration. On the other hand, magnetism requires TM ions with partially filled d (or f) shell.
3. *Electrical constraints*: ferroelectrics need to be insulators, otherwise an applied electric field would produce a flow of electric current rather than an electrical

polarization. On the other hand, strong magnetic materials such as ferromagnets are usually metals. Materials that display simultaneously insulating and magnetic behavior, typically are either ferrimagnetic or weakly ferromagnetic (i.e. with a canted antiferromagnetic structure).

4. *Structural constraints*: ferroelectricity requires the off-centered displacement of an ion in the cell, while in typical d^n TM magnetic ions such as Fe or Mn, the presence of unpaired d electrons induces a competing Jahn-Teller distortion.

1.2 Magnetically induced ferroelectricity

1.2.1 Classification of multiferroics

The renewed interest in magnetoelectric multiferroics is due to the discovery in 2003 of the coexistence of a strong spontaneous polarization ($P_r \sim 55 \mu\text{C cm}^{-2}$) at high temperature ($T_c = 1103 \text{ K}$) and of an antiferromagnetic order ($T_N \sim 643 \text{ K}$) in BiFeO_3 thin films [8]. The large value of polarization was confirmed later in high-quality single-crystals ($\sim 60 \mu\text{C cm}^{-2}$ along the [001] direction and $\sim 90\text{--}100 \mu\text{C cm}^{-2}$ along the [111] axis [9]). A multiferroic behavior characterized by a strong magnetoelectric coupling was reported at the same time in orthorhombic TbMnO_3 [10] and in TbMn_2O_5 one year later [11]. These promising results stimulated the discovery of several other multiferroics. Many of them are TM oxides with a perovskitelike structure. Following Khomskii, multiferroics materials can be classified into two categories [12]:

- *Type-I multiferroics*: Ferroelectricity and magnetism have a different origin; thus the two orders are weakly coupled (e.g. BiFeO_3). From the point of view of symmetry, type-I multiferroics undergo two distinct 2nd order phase transitions with temperature:
 1. The ferroelectric transition concomitant to an inversion-symmetry breaking ($\vec{r} \rightarrow -\vec{r}$).
 2. The magnetic transition concomitant to a time-reversal symmetry breaking ($t \rightarrow -t$).

- *Type-II multiferroics (or magnetic ferroelectrics)*: the ferroelectric order is induced by the magnetic one, which is appealing as this implies an inherently strong coupling between the two orders. Examples are TbMnO_3 or TbMn_2O_5 .

According to the terminology introduced by Levanyuk [13] and later adopted by most authors [14], type-II multiferroics are a particular case of the so-called *improper ferroelectrics*, where the main order parameter is not the polarization, as in the case of ordinary (or proper) ferroelectrics, hence ferroelectricity occurs as a secondary effect induced by the main order parameter.

In type-I multiferroics with perovskitelike ABO_3 structure, proper ferroelectricity is driven by the polar properties of A -cations, such as Bi^{3+} or Pb^{3+} , characterized by the presence of $6s^2$ lone-pair electrons. In this way, the B -sites are available to host the magnetic TM magnetic ions.

In the case of improper ferroelectrics, in addition to the case of magnetic ferroelectricity (MF), it is believed that ferroelectricity can be also driven by the following two mechanisms: i) geometric frustration (ex. in hexagonal RMnO_3); ii) charge/orbital ordering (ex. in LuFe_2O_4 [15, 16, 17] [18]). These mechanisms have been discussed in detail by Wang *et al.* [7].

In spite of the large P -values reported, potential applications of type-I multiferroics are limited by the usually weak magnetoelectric coupling. Indeed, as mentioned previously, in these multiferroics, the mechanisms driving the ferroelectric order and the magnetic one are different. Opposite situation typically occurs in type-II multiferroics, where the magnetoelectric coupling is inherently strong but the values of spontaneous polarization are typically smaller than $0.1 \mu\text{C cm}^{-2}$ ($\sim 0.06\text{-}0.08 \mu\text{C cm}^{-2}$ in orthorhombic TbMnO_3 [10], where ferroelectricity is induced by an incommensurate magnetic structure).

One of the motivations of the present Thesis is to investigate the origin of such modest spontaneous polarizations and whether this limitation can be overcome by stabilizing suitable crystal structures. In order to justify the research strategy adopted in the Thesis, in the following we shall provide a brief review of the state of the art on magnetic ferroelectrics (MFs).

1.2.2 Phenomenological theory

The phenomenological models of magnetic ferroelectricity are based on the Ginzburg-Landau theory of second order phase transition [19]. According to this theory, the magnetically ordered phase is described by one irreducible representation (different from the unitary representation) of the paramagnetic group.

A first model, developed by Goshen *et al.*, considers the case of ferroelectricity driven by antiferromagnetism in a prototype centrosymmetric system with $Pmma$ symmetry applicable to BiMn_2O_5 and TbCrO_3 [20]. The authors predicted the magnetic structure as well as the magnetically induced polar distortion of the lattice and were able to estimate P -values $\sim 0.01\mu\text{C cm}^{-2}$.

A second approach by Mostovoy [21] considers the case of ferroelectricity induced by a non uniform magnetic order, such as a spiral spin wave or an incommensurate structure, observed experimentally in TbMnO_3 [22] and $\text{Ni}_3\text{V}_2\text{O}_8$ [23]. The reason is that, in the uniform case, the lowest-order invariant in the thermodynamic potential describing a magnetoelectric coupling term must be quadratic in both, \vec{M} and \vec{P} (P^2M^2), as the invariant is required to obey time-reversal and inversion symmetries. This term represents a small correction leading to a weak multiferroic behavior and thus is not interesting for applications. On the other hand, the non uniform case ($\vec{M} = \vec{M}(\vec{r})$) allows the existence of a lower-order invariant containing the magnetization \vec{M} and its gradient and more pronounced multiferroic effects are to be expected. By adopting the Einstein's convention for the summation over i and j indices, this magnetoelectric term can be written as follows:

$$P_i[M_i \frac{\partial M_j}{\partial x_j} - M_j \frac{\partial M_i}{\partial x_j}] \quad (1.1)$$

In fact, the existence of a non uniform magnetic structure provides a necessary - but not sufficient - condition for the occurrence of multiferroicity. For example, the average polarization is zero for the sinusoidal spin density wave observed in TbMnO_3 in the 21 - 41 K range, while it is non zero for the helical wave stable below 21 K. The above term accounts for the lock-in transition at 21 K concomitant to the occurrence of ferroelectricity ($P_{10K}=0.08 \mu\text{C cm}^{-2}$) [10] and also explains the orientation of \vec{P} , which

turns out to be orthogonal to both, the rotation axis and the propagation vector of the helical wave [22].

Several microscopic mechanisms have been hitherto proposed to explain magnetic ferroelectricity and no consensus as to their general validity has been reached yet. In the following section, I limit myself to present briefly the most popular mechanisms which will be recalled later to discuss the experimental results of the present Thesis. They are based on two interactions:

- Spin-orbit coupling via the antisymmetric exchange interaction (or inverse Dzyaloshinskii-Moriya Interaction, DMI).
- Symmetric exchange interaction (or exchange-striction).

1.2.3 Microscopic theories

Antisymmetric exchange interaction

This interaction is a relativistic correction to the superexchange interaction that couples two non-collinear spins \vec{S}_i, \vec{S}_j . It can be shown that this term appears in the absence of inversion-center symmetry with respect to the middle point of the two spins and takes the form $\vec{D} \cdot \vec{S}_i \times \vec{S}_j$ [24, 25], where \vec{D} is the Dzyaloshinskii-Moriya vector. This interaction accounts for the stabilization of canted antiferromagnetism in buckled perovskitelike structures, where the buckling of the B - O - B bonds breaks the B - B axis rotation symmetry.

The role played by this interaction in magnetic ferroelectrics was first considered by Katsura, Nagaosa and Balatsky [26], following a previous study by Bruno *et al.* on the spin currents generated at equilibrium conditions in inhomogeneous magnetic structures [27]. Katsura *et al.* predict that, the spin currents produced in these structures induce a polarization of the electronic orbitals (spin-current model) described by:

$$\vec{P} \propto e_{i,j} \vec{e}_{i,j} \times (\vec{S}_i \times \vec{S}_j) \quad (1.2)$$

In this case, contrary to the case of ordinary ferroelectrics, no phonon anomaly is expected at the ferroelectric transition, as the magnetoelectric coupling would be provided

by an hybrid magnetoelectric excitation called electromagnon [28] whose observation remains elusive.

Following an approach similar to that followed by Goshen *et al.* [20] and including both, exchange striction and DMI interaction, Sergienko and Dagotto [29], showed that the latter mechanism is responsible for a polar distortion of the lattice induced by incommensurate magnetism in the aforementioned compounds TbMnO_3 and $\text{Ni}_3\text{V}_2\text{O}_8$. By including an explicit dependence of the Dzyaloshinskii-Moriya vector on the atomic positions, the authors find a polar distortion of the oxygen ions responsible for the electric polarization (see Fig.1.2) described by an expression similar to the above Eq. 1.2.

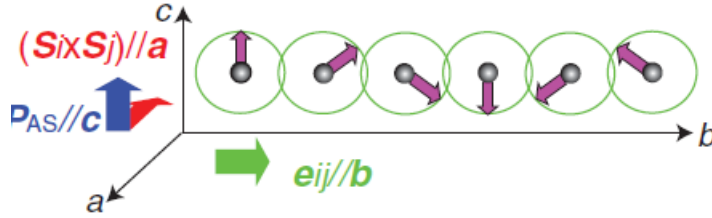


Figure 1.2: Orientation of the spontaneous polarization P for the bc -plane spiral spin structure predicted by the electronic spin-current model. After [30]

..

Several authors [31, 32, 33, 14] have discussed the possibility that non uniform or incommensurate magnetic structures that can host the DMI interaction would be favored by geometric frustration. We shall not discuss further this open issue which goes beyond the scope of the present thesis. Finally, the coexistence of both polarizations of the lattice and of the electronic orbitals has been supported by *ab initio* calculations within density functional theory [34].

Exchange striction

Magnetic ferroelectricity has been observed also in collinear or quasi-collinear magnetic structures, where the DMI interaction is absent by symmetry. This is the case of orthorhombic perovskite manganites like HoMnO_3 with E -type magnetic structure [35]. This observation strongly indicates that ferroelectricity is driven by the symmetric exchange interaction. Sergienko *et al.* [36] developed a realistic microscopic model that

1.2. Magnetically induced ferroelectricity

includes the exchange interaction between nearest-neighbor spins ($\vec{S}_i \cdot \vec{S}_j$) forming the collinear E-type magnetic structure shown in Fig. 1.3 and a spin-phonon coupling. The model was studied by means of Monte Carlo calculations and successfully accounts for the stability of the above magnetic order and also predicts a polarization arising from a coherent displacement of the oxygen atoms as shown in Fig. 1.4. The calculations predict large polarization values $0.5 \mu\text{Ccm}^{-2} < P < 12 \mu\text{Ccm}^{-2}$, two order of magnitude larger than those observed in spin-spiral magnets. Unfortunately, a much smaller value of $0.08 \mu\text{C cm}^{-2}$ was reported experimentally [37]. One explanation of this discrepancy is that the *R*-Mn exchange interaction competes with the Mn-Mn exchange, thus leading to a more complex ferroelectric phase than that theoretically predicted [38].

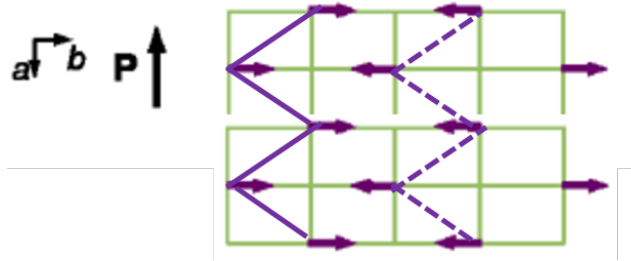


Figure 1.3: Schematic representation of the E-type magnetic structure after Ref. [36]. Note the ferromagnetic zig-zag chain formed by the Mn ions. Solid and broken lines indicate the nearest-neighbor antiferromagnetically coupled zig-zag chains.

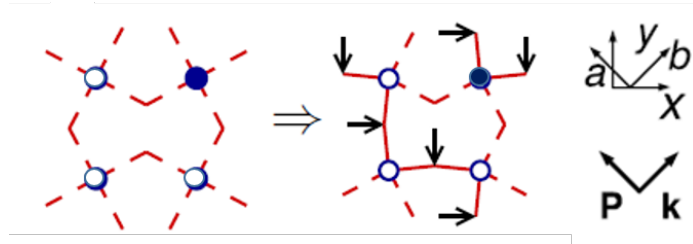


Figure 1.4: Left: not distorted E-type magnetic structure. Right: distorted E-type magnetic phase leading to spontaneous polarization along the diagonal connecting the next-nearest-neighbor Mn atoms. Arrows indicate oxygen displacements. Opposite Mn spins are represented by open and filled circles.

While it is accepted that the DMI interaction inherently leads to modest polarizations for it arises from a relativistic correction, the large *P*-values predicted theoretically

in the case of dominant exchange-striction remain to be observed experimentally [39]. The challenge is to understand to which extent this discrepancy arises from the lack of a suitable theoretical description or from the non favorable structural and electronic characteristics of the magnetic ferroelectrics hitherto studied. The motivation of the present Thesis is provided by the very promising multiferroic performances of quadruple perovskites, as illustrated below.

1.3 $(AMn_3)Mn_4O_{12}$ quadruple perovskites

A breakthrough came with the observation in the quadruple perovskites $(CaMn_3)Mn_4O_{12}$ of much larger polarizations, $P = 0.2870 \mu C \text{ cm}^{-2}$, induced by magnetism than those previously reported in other magnetic ferroelectrics [40, 41]. This observation may suggest that the peculiar structural features of quadruple perovskites provide favorable conditions for hosting ferroelectricity.

The quadruple perovskite structure $(AA'_3)B_4O_{12}$ was first reported by Marezio *et al.* for $(NaMn_3)Mn_4O_{12}$ [42], following the synthesis of the prototype compound $CaCu_3Ti_4O_{12}$ by Deschanvres *et al.* [43]. This report prompted the synthesis of similar compounds with different atomic substitutions at the A site ($A = Na, Ca, Cd, Sr, La, Nd$) [44]. The pseudo-cubic structure of these compounds is made of eight simple perovskite (ABO_3) units (see left panel of fig. 1.5). A peculiar feature is the unusually large ($\sim 45^\circ$) tilt of the BO_6 octahedra around the (110) axis, which is typically stabilized by high-pressure. This distortion leads to a doubling of the unit-cell parameter of the pristine ABO_3 cell. It follows that the $(AMn_3)Mn_4O_{12}$ unit cell contains two inequivalent crystallographic sites A and A' . The Wyckoff positions of the different crystallographic sites of the structure are reported in table 1.3. The coordination number of the former sites is twelve as in the simple perovskite structure, while that of the latter sites is reduced to four because of the above large distortion (see right panel of Fig. 1.5). The driving force of the distortion is the Jahn-Teller effect in the A' -sites. Interestingly the square-coordination of A' -sites with oxygen atoms prevents the stabilization of oxygen vacancies. This constitutes an advantage as compared to simple perovskite compounds where oxygen non-stoichiometry greatly affects the physical properties. As a consequence of the large tilt of BO_6 octahedra, there are two

1.3. $(AMn_3)Mn_4O_{12}$ quadruple perovskites

zig-zag superexchange paths, B - O - B and A' - O - B . The value of the B - O - B bond angle ($\psi \sim 137^\circ$) is intermediate between the collinear ($\psi = 180^\circ$) and perpendicular ($\psi = 90^\circ$) geometries. According to the Goodenough-Kanamori-Anderson rules [45] this intermediate geometry leads to competing ferromagnetic and antiferromagnetic interactions. An indication of this competition is given by the C-type structure of the B -ions found in $(LaMn_3)Mn_4O_{12}$, formed by ferromagnetically-coupled antiferromagnetic planes [46]. Because of the square-planar coordination, the magnetic interaction between neighboring A' -sites is mediated by the B -sites and the corresponding superexchange path is A' - O - B - O - A' . In this Thesis we focus on the quadruple perovskites where $A'=B=Mn$.

Sites	Wyckoff positions
A	$2a$
A'	$2b, 2c, 2d$
B	$4e, 4f$
O	$4i(\times 2), 8j(\times 2)$

Table 1.1: Wyckoff positions of the quadruple perovskite $(AA'_3)B_4O_{12}$ crystallographic structure.

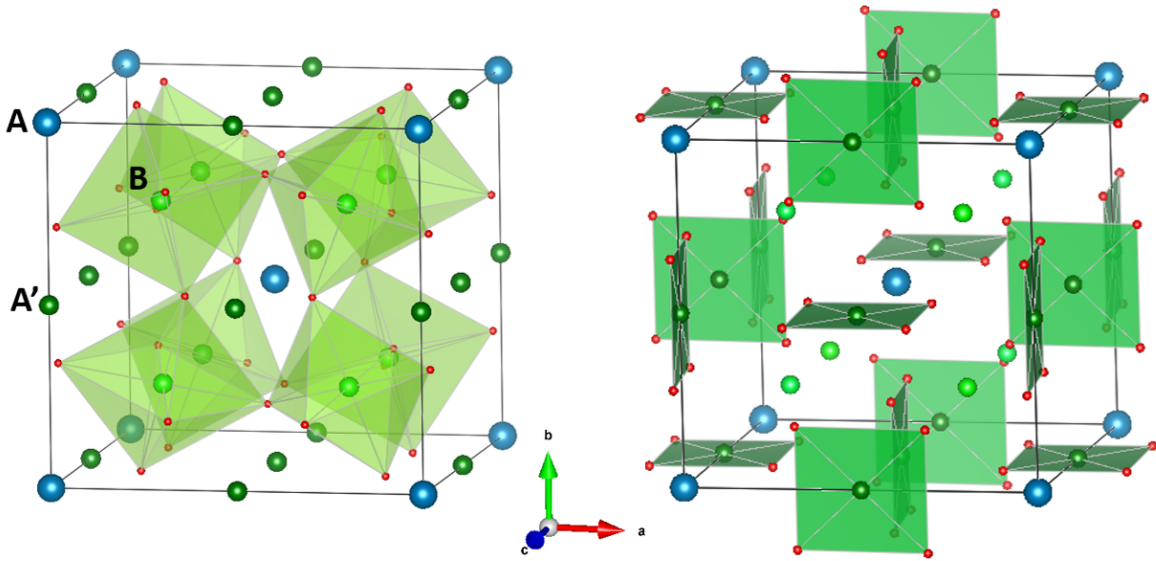


Figure 1.5: Quadruple perovskite crystal structure $(AA'_3)B_4O_{12}$. Left part: octahedral oxygens environment of B -sites. Right part: square-planar oxygens environment of A' -sites.

The above peculiar features of quadruple perovskites may account for the unique

physical properties observed, namely the almost full $\text{Mn}^{3+}/\text{Mn}^{4+}$ charge order in $(\text{NaMn}_3)\text{Mn}_4\text{O}_{12}$ [47] and the aforementioned large magnetic ferroelectricity in $(\text{CaMn}_3)\text{Mn}_4\text{O}_{12}$. Following the latter finding, it would be very interesting to unveil the microscopic mechanism of such an enhanced polarization. This issue remains controversial because of the complexity of the magnetic order consisting of an incommensurate spin-spiral wave [41]. It has been argued that this complex magnetic structure is affected by the charge and orbital orderings stabilized by the mixed valency properties of $(\text{CaMn}_3)\text{Mn}_4\text{O}_{12}$ [48]. The authors ruled out the conventional DMI mechanism of magnetic ferroelectricity presented in the previous section by considering that the orientation of the electric polarization is perpendicular to the spin rotation plane of the helix. They therefore proposed a modified DMI model where the magnetoelectric invariant in the thermodynamic potential couples the polarization with the ferroaxial component of the crystal structure. In any case, the symmetry properties of the magnetic structure and of the polarization observed are also consistent with the exchange-striction mechanism [49]. In conclusion, it appears to be difficult to single out the contribution of each of the two mechanisms to the enhancement of magnetic ferroelectricity in $(\text{CaMn}_3)\text{Mn}_4\text{O}_{12}$. In view of this, it would be desirable to study a related compound displaying similar multiferroic properties but a simpler magnetic structure, which would help elucidating the relevant structural and electronic parameters that govern the above enhancement. This motivation has guided the present Thesis, as illustrated in the section below.

1.3.1 Open questions and strategy for the Thesis

Specific questions addressed in the Thesis are as follows:

- Are the above large polarizations a characteristic feature of the $(\text{AMn}_3)\text{Mn}_4\text{O}_{12}$ family?
- What are the structural parameters of these compounds relevant to the enhancement of the multiferroic performances (high transition temperature, high value of P , strong magnetoelectric coupling)?

- Is charge ordering relevant to the enhancement of the polarization in $(AMn_3)Mn_4O_{12}$ compounds?
- Based on the answer to the previous questions, can we find new $(AMn_3)Mn_4O_{12}$ compounds where the exchange-striction mechanism alone drives large magnetic ferroelectricity?

We have focused our work on two quadruple perovskite compounds, $(LaMn_3)Mn_4O_{12}$ and $(YMn_3)Mn_4O_{12}$, where the isovalent La/Y substitution enabled us to investigate the possibility of tuning the magnetic and ferroelectric properties by using chemical pressure as control parameter. We believe that these two compounds offer an ideal playground to address the above questions owing to a similar crystal structure and the simple single-valent Mn^{3+} properties.

The Thesis is organized as follows:

Chapter 2 is devoted to the experimental methods. The first step was the high-pressure synthesis of the samples. After the synthesis, the determination of structural and magnetic structure was carried out by x-ray and neutron diffraction on single-crystals and powder samples, respectively. The characterization of the physical properties at low temperatures was performed using standard physical property characterization tools. Raman and IR spectroscopy techniques have enabled us to study the vibrational properties and to investigate the spin-phonon coupling. Finally, the ferroelectric properties were studied by means of pyrocurrent and dielectric constant measurements on polycrystalline samples.

The first compound, object of the present Thesis is $(LaMn_3)Mn_4O_{12}$, it has been preliminary studied by our research group. As reported in [46], this compound has been successfully synthesized under high-pressure (6 GPa) and crystallizes in the centrosymmetric - monoclinic space group $I2/m$ at room temperature. A great advantage of this system is a simple commensurate magnetic order made of two magnetic sublattices (see Fig. 1.6). The B -site sublattice forms a C -type structure at $T_{N,B} = 78$ K. In this structure the antiferromagnetic ac -planes are coupled ferromagnetically along the b -axis. The moments are oriented along the ac -diagonal and canted along b . The A' -site sublattice form an anti-body antiferromagnetic structure at $T_{N,A'} = 21$ K and the

moments lie along c . Within the experimental resolution, the temperature dependence of the moments of each magnetic sublattice shows no anomaly at $T_{N,A'}$, which indicates that the two orders are independent of each other (fig. 1.7). Very interestingly, $(\text{LaMn}_3)\text{Mn}_4\text{O}_{12}$ is a simple single-valent Mn^{3+} system, so the $\text{Mn}^{3+}/\text{Mn}^{4+}$ charge ordering observed in the related compound $(\text{CaMn}_3)\text{Mn}_4\text{O}_{12}$ does not come into play. In addition, we will show that the above C -type structure enables us to rule out the role of the antisymmetric exchange in the magnetic ferroelectricity. As a consequence, this compound is an ideal playground to elucidate the above questions.

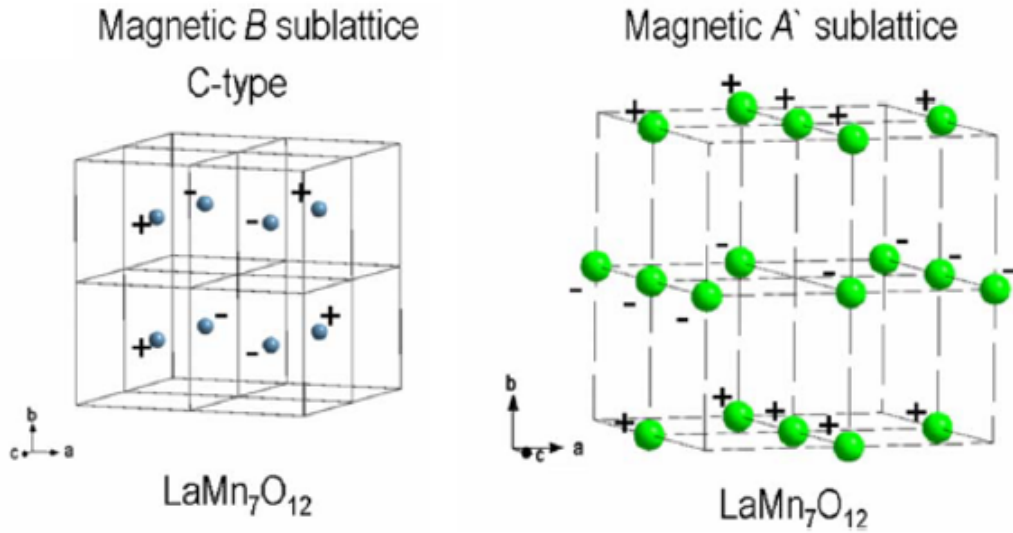


Figure 1.6: The magnetic structure of $(\text{LaMn}_3)\text{Mn}_4\text{O}_{12}$ as reported by Prodi *et al.*, in [46]. Left: magnetic structure of B -sites occurring at $T_{N1} = 78$ K. Right: magnetic structure of A' -sites below $T_{N2} = 21$ K.

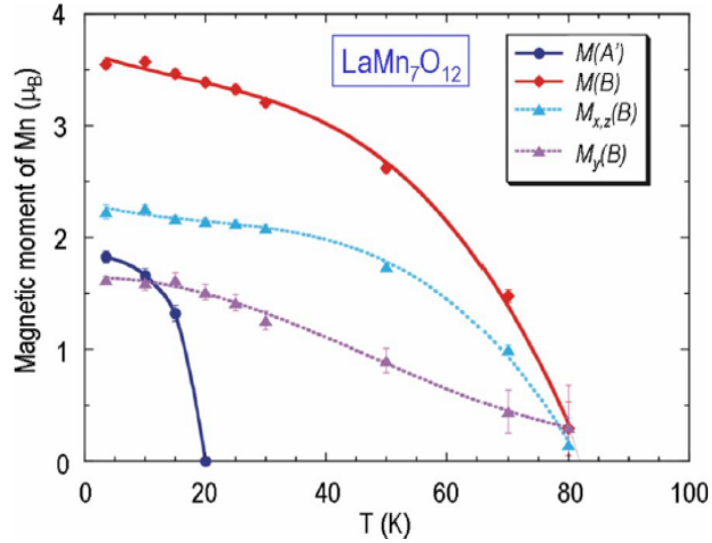


Figure 1.7: After A. Prodi et al.,: Temperature dependence of the cartesian components and of the moduli of the moments for the two magnetic structures of the A' and B sublattices.

In **Chapter 3**, I present the multiferroic properties of $(LaMn_3)Mn_4O_{12}$ (LMO).

In **Chapter 4**, we report on a systematic study of the magnetoelastic coupling in LMO by means of infrared (IR) and Raman spectroscopy and by specific heat measurements and interpretate the results within the framework of the theory of improper ferroelectrics developed by Levanyuk and Sannikov [13].

The last two Chapters 5 and 6 are devoted to the second compound, $(YMn_3)Mn_4O_{12}$ (YMO), a new phase that I synthesized during the course of the Thesis. The main motivation was to investigate the effect of chemical pressure on the magnetic and ferroelectric properties. This was achieved by substituting the La^{3+} ion with the smaller Y^{3+} on the A -sites. Our expectation was an enhancement of the exchange interaction and thus higher ordering temperatures and possibly even stronger magnetic ferroelectricity.

Chapter 5 is devoted to a full study of the crystal and magnetic structures and of the magnetic properties of (YMO).

Finally, in **Chapter 6**, we report on the multiferroic properties of YMO, and on its exact low-temperature crystal structure.

Chapter 2

Experimental methods

Dans ce chapitre, j'ai fait le choix de ne pas développer la théorie relative à chaque technique expérimentale, puisqu'il s'agit de techniques largement connues et référencées, mais d'en donner seulement les grandes lignes qui m'ont été nécessaires de connaître lors des manipulations et de l'analyse des données. L'ensemble des travaux expérimentaux a été possible grâce à de nombreuses collaborations (IMEM-CNR, ESPCI, IMPMC, UF-SCar) et dans le cadre de temps de faisceaux obtenus à l'ILL et à SOLEIL. Durant ma thèse, j'ai donc pu découvrir de nombreuses techniques et obtenir une caractérisation complète de mes échantillons. J'ai choisi de développer légèrement la partie technique relative aux synthèses sous haute pression car ce travail a constitué une large part de mon activité lors de mon année à l'IMEM-CNR à Parme. Ce chapitre ne comporte aucun rappel sur la théorie de la diffraction mais présente seulement le protocole suivi pour la caractérisation structurale des échantillons. Il comporte tout de même une discussion sur la différence entre la spectroscopie Raman et infrarouge, nécessaire à l'interprétation des résultats qui seront présentés au chapitre 4. J'ai personnellement participé à toutes les expériences sauf aux mesures de caractérisations électriques effectuées à l'IMEM par R. Cabassi et F. Bolzoni ou à l'université de São Carlos, aux mesures d'aimantation avec le SQUID effectuées par D. Delmonte au département de physique de l'université de Parme, et certaines mesures de diffraction sur poudres et monocristaux directement effectuées par F. Mezzadri au département de chimie de l'université de Parme.

2.1 High-pressure/high-temperature syntheses

As explained in the previous chapter, in nature, electric and magnetic orders tend to avoid each other for several fundamental reasons. One effective solution to stabilize new crystal structures that allow simultaneously electric and magnetic order is to use high-pressure. Indeed, high-pressure enables a large increase in density, changes in orbital hybridization and coordination number, with deep modification of the electronic structure and transport properties. Exemple include insulator-metal transitions [50] and induction of superconductive properties [51]. In the case of quadruple perovskite structure [42], subject of the present thesis, high-pressure helps to stabilize the Mn^{3+} ions on the A' -sites in the square planar coordination by driving the very large tilt of the corner-sharing BO_6 octaedra which results in a structure 20% densier than the simple perovskite. The technical difficulty is to apply a very high isotropic pressure during the synthesis and obtain homogeneous phase products. In order to reach this objective we have used a 1000 tons multianvil Walker-type press available at the IMEM-CNR in Parma represented in Fig 2.1.



Figure 2.1: The multianvil 1000 tons Walker-type press at IMEM-CNR (Parma, Italy)

This apparatus is suitable for the synthesis of bulk materials under variable isotropic temperature and pressure conditions in the range $2.5 \text{ GPa} < P < 25 \text{ GPa}$ and $0^\circ \text{ C} < T < 2200^\circ \text{ C}$. The maximum (P, T) value is equivalent to the conditions found in the boundary zone between the lower region of the Earth crust and the higher region of the upper mantle, at a depth of 750/800 Km ! The experimental issues occurring in the artificial realization of intense pressures is non trivial. Indeed, high uniaxial pressure (up to 300 GPa) can be applied in a Diamond Anvil Cell and hydrostatic forces could easily be applied through a fluid compression for relatively low pressure (until $\sim 20 \text{ kbar}$ GPa). The difficulty comes when one needs to applied high pressure (several GPa) in isotropic condition. Indeed, at these pressures, liquids do not exist anymore since any material would become solid. The solution that offers the multianvil press is to transform an unidirectional compression force into a quasi isotropic one by means of three different solid components with increasing hardness. The device was invented by David Walker which described his new module designed for producing new synthetic minerals in 1990 [52]. This system converts an axial load over a circular surface, due to the controlled push of a cylindrical piston managed by oil-dynamic circuit, into a three-components force through a set of six wedges, made of tempered steel. As represented in Fig. 2.2, the combination of the six edges generates a cubic cavity filled by eight truncated tungsten carbide cubes which in turn are gathered to create an inner octahedral cavity with a four components resultant force, respectively perpendicular to the four triangular faces of the octahedron. Inside this cavity, we put a porous magnesium oxide octahedron pierced in its center from one side to the other by a cylindrical cavity in which we place a closed cylindrical graphite oven (see Fig. 2.3) which contain the chemically inert noble metal (usually gold or Platinum) capsule containing reagents. The size of the truncation of cubes and of the octahedra is variable, according to the maximum pressure desired. For instance, the quadruple perovskite $(\text{LaMn}_3)\text{Mn}_4\text{O}_{12}$ is obtained at 6 GPa with the largest truncation (17 mm) and the largest octahedra (edges of 25 mm) whereas $(\text{YMn}_3)\text{Mn}_4\text{O}_{12}$ is obtained at 9 GPa which requires smaller truncation of cubes (11 mm) and smaller octahedron (edges of 18 mm).

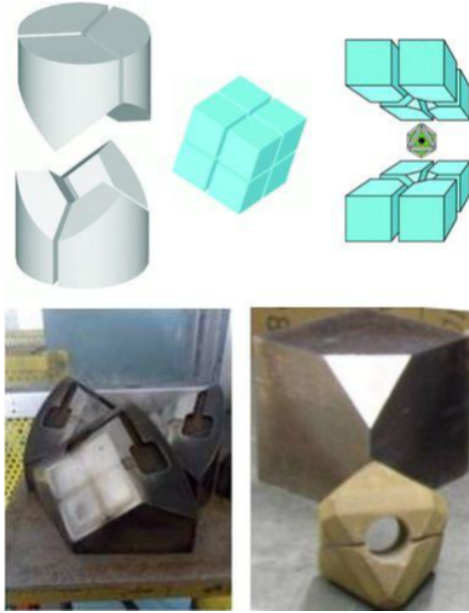


Figure 2.2: up: Scheme of components constituting the Walker type module and the way they are assembled. In the lower part of the figure: from left to right some tempered wedges, a tungsten carbide cube and a correspondent MgO octahedron.

In the middle region of the graphite cylinder, where the capsule is placed (see Fig 2.3), the pressure is quasi-isotropic with a maximum gradient of pressure along the cylinder of about 0.1 GPa/cm at 6 GPa. The heating of the capsule is realized with Joule effect by applying tension between the two tops of the graphite-cylinder inside which has been beforehand introduced a thermocouple. This electrical control allows to manage the temperature exactly around the core of the reaction cell.

The typical synthesis procedure is composed of three successive operations:

1. The pressure is gradually increased from room pressure (100 kPa) to the chosen set point (*e.g.* 6 GPa) with a typical ramp rate in the range 500-700 Pa/min.
2. Then, the system is heated from room temperature to the temperature set-point and is kept stable for the chosen reaction time (typically 2 hours).
3. At the end of the reaction, the system is either quenched down to room temperature by switching off the power unit or the temperature is slowly decreased with a controlled thermal ramp. Once the external temperature on the surface of the

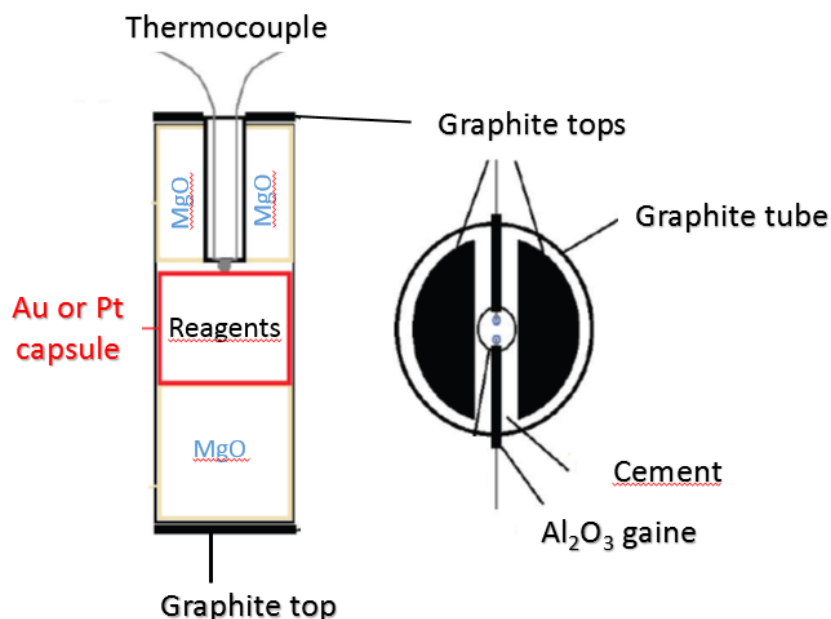


Figure 2.3: Scheme of the capsule holder and thermocouple disposition inside the cylindrical graphite oven.

Walker-type module is equal to the internal temperature, the pressure is slowly released with a rate of 300 Pa/min.

The role of quenching is to "freeze" the obtained high-pressure phase since often the structure would have been different at room conditions. In other words, the obtained high-pressure phases are metastables at atmospheric T and P .

All syntheses were performed from powder reagents grounded manually in a stoichiometric mixture and we obtained homogeneous powder that we could characterize by X-ray diffraction and from which we could, in some cases, extract small single-crystals. However, such single-crystals are often very small ($50 \mu\text{m}$) and usually twinned, which reduces drastically the type of experiments that can be performed. One of the objective of my work in Parma, was to obtain large and non-twinned $(\text{LaMn}_3)\text{Mn}_4\text{O}_{12}$ single-crystals. To do so, we followed the idea, established by a previous systematic study of the phase diagram of $(\text{NaMn}_3)\text{Mn}_4\text{O}_{12}$ [53, 54], that largest crystals growth around the border which separates the instability from the stability field in the P/T phase diagram.

My second objective was to find the good conditions for the obtention of the new quadruple provskite $(\text{YMn}_3)\text{Mn}_4\text{O}_{12}$. After having found the P/T conditions and in order to obtain a large amount of $(\text{YMn}_3)\text{Mn}_4\text{O}_{12}$ powder (~ 1 g) for neutron diffraction experiment I performed several syntheses with a bigger multi-anvil press of 5000 tons available at the Bayerisches Geoinstitut of Bayreuth for visitors in the framework of the DFG Core facility for High-Pressure Research. Indeed, this big press permit to obtain ~ 130 mg of powder for each synthesis at 9 GPa while we obtain only 30 mg of powder at the same pressure with the press of 1000 tons.

2.2 Diffraction techniques

1. After each synthesis, we systematically performed powder X-ray diffraction (PXRD) at room temperature in order to determine the purity of the sample and the percentage of the other phases. These measurements were performed in the Bragg-Brentano geometry using a laboratory diffractometer equipped with a Cu K_α source. This step permits to optimize the P - T conditions for new phases research and to get big single-crystals. In the research for the new $(\text{YMn}_3)\text{Mn}_4\text{O}_{12}$ phase, this step was very important to see if the quadruple perovskite structure was obtained or not and in which proportions, according to the conditions of the synthesis. We made this analysis with the help of the *powder-cell* software by qualitative comparison to the $(\text{LaMn}_3)\text{Mn}_4\text{O}_{12}$ spectrum.
2. We performed room temperature single-crystal X-ray diffraction using two diffractometers: at Parma, a *Bruker APEX II* and at IMPMC: an *Oxford diffraction Xcalibur-S* diffractometer both equipped with a CCD area-detector and graphite monochromatized Mo K_α radiation. Refinements were performed by F. Mezzadri and B. Baptiste. This step was useful for identifying the space-group of $(\text{YMn}_3)\text{Mn}_4\text{O}_{12}$, but also for selecting the better single-crystals for further experiments (spectroscopy, synchrotron ...).
3. We performed a neutron powder diffraction experiment at the *high-intensity two-axis D20 diffractometer* of the Institut Laue Langevin using $\lambda_1 = 1.54 \text{ \AA}$ and $\lambda_2 = 2.41 \text{ \AA}$ wavelengths and a 90° takeoff set-up. The data were taken as a function

of temperature by warming-up the sample from 4 K up to room temperature at a rate of 0.25 K/min. The first wavelength is optimized for the determination of the nuclear structure and the second wavelength for the determination of the magnetic structure. At this step, I went to the 9th fullprof school in Grenoble and learnt the use of the *fullprof package* [55] and how to perform a *Rietveld refinement* [56] and determine a magnetic structure using the theory of irreducible representations [57].

4. Low temperature single-crystal synchrotron diffraction experiment was performed at the beamline CRISTAL of the french synchrotron SOLEIL in Saint-Aubin. It allows to determine the low temperature space-group and the occurrence of a loss of spatial inversion center. These two points were not possible to reach in laboratory because of the lack of diffractometers with low temperature environment and the low flux of laboratory sources with respect to synchrotron.

2.3 Thermodynamics measurements

2.3.1 Transport properties

In the framework of the search for multifunctional materials suitable for applications, it is essential to determine the transport properties of the new samples by measuring the resistivity. This characterization has been performed at IMEM-CNR (Parma) by measuring the resistance as a function of temperature in a *Magnetic Properties Measurement system (MPMS)* used as a cryostat. The system simply measures the current going through the sample when applying a voltage. Such a measure was realized on polycrystalline pellets polished into disk shape (0.1-0.6 mm \times 2-4 mm²) and contacted with silver paste.

There are two possible configurations for contacts :

1. Two contacts: both faces are entirely contacted and the resistance (R) is directly measured between them. This technique does not permit to avoid the contribution of contacts to the value of R but gives a rapid and good preliminar characterization of transport properties, especially for insulating samples for which the resistance

due to contacts is expected to be negligible with respect to the resistance of the sample.

2. Van Der Pauw configuration (Four contacts) [58]. The sample is contacted on four different points (A, B, C and D) of one surface and eight measurements are performed in rapid succession: all possible permutations of choosing two adjacent contacts for the voltage and the other two for measuring the current. Each measure is performed two times with $+V$ and $-V$. We can deduce the in-plane resistivity (ρ) of the sample, without the contribution of contacts, with the following formula:

$$\rho_{in-plane} = \frac{\pi d}{\ln 2} \frac{\sum_{i=1}^8 R_i}{8} f$$

where d is the thickness of the disk and f a shape factor which is equal to 1 in the case of a circular disk.

Measurements obtained with the two different methods for $(\text{YMn}_3)\text{Mn}_4\text{O}_{12}$ polycrystalline sample are reported on Fig. 2.4 and we can see that the curve obtained from the two contacts measurements is weakly higher than the one obtained with the van der Pauw technique, which confirms that the contribution of contacts to the resistivity is negligible.

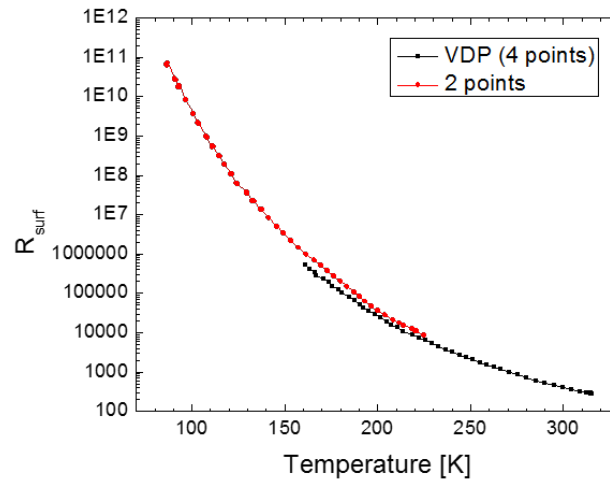


Figure 2.4: Resistivity of $(\text{YMn}_3)\text{Mn}_4\text{O}_{12}$ pellets obtained using the two- and four- (VDP) contact configurations. VDP stands for van der Pauw.

2.3.2 Magnetization

In the framework of this thesis, two commercial dispositives from *Quantum Design*TM have been used to perform magnetic measurements.

- **Magnetic Properties Measurement System (MPMS) of the Superconducting QUantum Interference Device (SQUID) (*Parma*):** This magnetometer is able to detect a magnetic signal from 10^{-8} to 5 emu and to apply a magnetic field between -5 and 5 T in a temperature range going from 2 to 400 K. The principle of the measurement is to detect the magnetic flux created by the sample through some current loops as a function of the position of the sample on the axis of these loops. The variation of the flux is proportional to the magnetic field and the speed of the sample. The sample is fixed on a plastic-straw which moves through a constant and homogeneous magnetic field created by a superconducting magnet.
- **Vibrating Sample Magnetometer (VSM) option of the Physical Properties Measurement System (PPMS) (*IMPMC, Paris*):** the option is similar to the SQUID but the sample vibrates around a fixed position inside non-superconducting copper coil. The maximal speed that can be reached by the sample is high (100 cm/s). This increases the intensity of the signal with respect to the SQUID but reduces the sensitivity to 2.5×10^{-5} emu.

2.3.3 Heat capacity

The specific heat is the first order derivative with respect to temperature of the Hentalpy at constante pressure. There are two contributions to this quantity: the contribution of the conduction electrons and the contribution of lattice. Thus, for insulating materials, it is a natural probe for lattice effects and all kind of phase transitions. Besides, it can be easilly measured as it does not require any contact and can be performed on polycrystalline samples. Usually, it requires ~ 2 mg of material for the signal to be intense enough. We performed specific heat measurements with the PPMS by using the *constant pressure relaxation method*. The temperature range is 1.9 - 300 K. The method consists in weakly increasing the temperature of the sample by a calibrated

heat quantity Q (typically 1%) during a time t and then measuring, as a function of temperature, the time τ it takes to come back to its initial temperature. The characteristic time of the relaxation is directly related to the specific heat of the sample. The sample holder is shown in Fig. 2.5. A heating resistor and a thermometer are located below the sample holder and Cu wires connect electrically and thermally the sample to the resistor, the thermometer and the PPMS. To ensure a good thermalisation, the sample is fixed on the sample holder with a thin layer of grease and in order to avoid thermal effects due to impurities, the measure is performed in a high vacuum of 10^{-5} mBar. The measurement requires two steps: first it is necessary to calibrate the signal of the grease alone as a function of temperature. Then a second measurement is made after having put the sample on the previous quantity of grease. By subtracting the first measurement to the second, we obtain the contribution of the sample only.

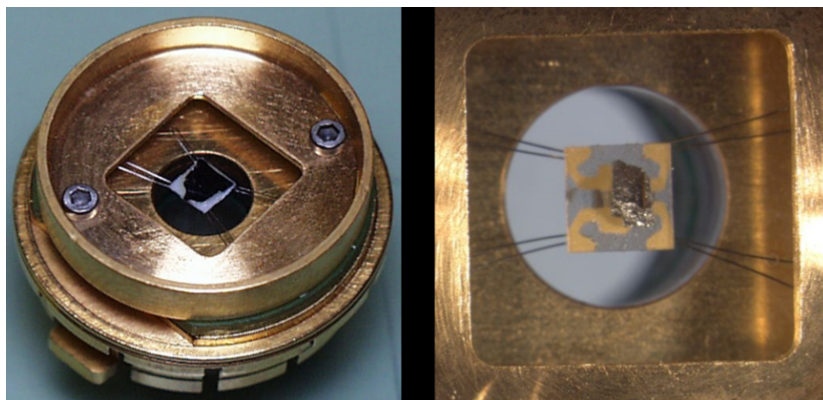


Figure 2.5: Sample holder for the specific heat option of the PPMS.

2.4 Spectroscopy techniques

2.4.1 Difference between Infrared and Raman spectroscopy

A plan-wave is composed of electric and magnetic field, in phase and perpendicular to each other and to the direction of propagation. When an electromagnetic wave goes through a solid, it undergoes 2 types of scattering:

- **Elastic scattering:** No energy transfer, only the direction of the incident photon of energy $h\nu$ is modified. After the sample, the light is diffused and this diffusion can be coherent (*Diffraction*) or incoherent (*Diffusion Rayleigh*)
- **Inelastic scattering:** The incident photon of energy $h\nu$ exchanges a quantity of energy with the sample. This quantity is characteristic of one specific excitation of the crystal. If the energy transfer is total, the incident photon is totally annihilated (or emitted) and it is the case of *infrared* absorption phenomenon (1 photon processus, see Fig 2.6 a). If the energy transfer is partial, the incident photon loses or gains a quantity of energy and this is the *Raman diffusion effect* (two photons processus which combines absorption and emission, see Fig 2.6 b).

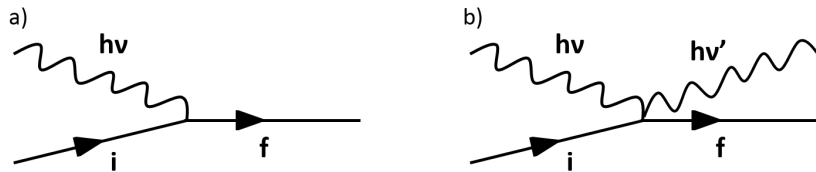


Figure 2.6: Feynmann diagrams of a) infrared absorption and b) Raman diffusion processus. i and f name the initial and final states of the sample, respectively.

In condensed matter, the characteristic energy of the collective excitations of atoms (phonons) is 10-100 meV and can be investigated by Raman and IR spectroscopies which deal with optical frequencies (THz). We record that:

$$8 \text{ cm}^{-1} = 1 \text{ meV}; \quad 33 \text{ cm}^{-1} = 1 \text{ THz}; \quad 100 \text{ cm}^{-1} = 100 \mu\text{m}$$

Spectroscopy measurements can be performed as a function of temperature and thus permit to identify the coupling effect between the lattice and any kind of order (magnetic, ferroelectric, charge...) occurring with temperature.

The principle of IR and Raman spectroscopies is the interaction between the electric field of light and the electric dipolar moment of the material. The dipolar moment is given by :

$$\vec{\mu} = \vec{\mu}_0 + \chi \vec{E} \quad (2.1)$$

$\vec{\mu}_0$ is the permanent dipolar moment which is non-zero if the barycentres of positive and negative charges are different and χ is the polarizability tensor of the material which quantifies the deformation of electron clouds induced by the presence of an electromagnetic wave. Thus, the induced dipolar moment is $\vec{p} = \chi \vec{E}$.

Classical selection rules: In a classical point of view, a crystal can absorb or produce a photon at the same frequency than the periodical vibration of its dipolar moment. If the phonon induces an oscillation of $\vec{\mu}_0$ there is an IR emission. On the contrary, if an incident IR radiation is able to induce a periodical oscillation of $\vec{\mu}_0$, there is absorption of this IR radiation. On the other hand, the electric field of a monochromatic incident radiation of frequency ν_0 can induce in the crystal a dipolar moment $\vec{p} = \chi \vec{E}$ oscillating at the same frequency, this is the Raman effect. Therefore, the classical selection rules are:

- IR-active mode if $\left[\frac{\partial \vec{\mu}}{\partial Q_k} \right]_{eq} \neq 0$ where Q_k is the normal coordinates of mode k: the phonon induces an oscillation of the permanent dipolar moment.
- Raman-active mode if $\left[\frac{\partial \chi}{\partial Q_k} \right]_{eq} \neq 0$: the phonon induces an oscillation of the polarizability.

Quantum selection rules:

- IR-active mode if $\langle f | \mu | i \rangle \neq 0$
- Raman-active mode if $\langle f | \chi | i \rangle \neq 0$

These two matrix elements results from the term $-\vec{\mu} \cdot \vec{E}$ in the Hamiltonian, due to the presence of an electric field.

In the framework of the Ginzburg-Landau theory of second-order phase transition, μ plays the role of the order parameter (η) and E is the external field h . We recall that

the general functional in the vicinity of the critical temperature (T_c) is written:

$$\phi = \alpha_0 \left(\frac{T - T_c}{T_c} \right) \eta^2 + \frac{\beta}{2} \eta^4 - \eta h \quad (2.2)$$

with α and β two positive coefficients.

Mutual exclusion rule: For a centrosymmetric crystal, that is, the case of a space group including the inversion symmetry, we can make the following symmetry considerations:

- Since $\vec{\mu}$ is a polar vector, parities of states $|i\rangle$ and $|f\rangle$ in $\langle f|\mu|i\rangle$ have to be different.
- On the other hand, χ is even with respect to the inversion, therefore $|i\rangle$ and $|f\rangle$ must have the same parity in $\langle f|\chi|i\rangle$.

These symmetry constraints lead to the following exclusion rule: "*In centrosymmetric crystal, IR-active modes are inactive in Raman and vice-versa*". As a consequence, the combination of IR and Raman spectroscopies is very useful to identify the break of the inversion center in crystals when diffraction techniques fail in practice, as we will see is the case in most of the magnetic ferroelectrics.

2.4.2 Sample preparation for spectroscopy

The preparation of samples is a critical phase for spectroscopy measurements. For example, Raman spectroscopy is a surface sensitive technique as the penetration depth of the incident radiation is of few hundred of nanometers. In order to obtain a smooth surface, we tried to polish the sample with a mechanical polisher using a very thin grain-paper of 0.1 μm but this was not successful as we obtained poor Raman signal and thus we conclude that the polishing probably degradates the first layers probed during the Raman spectroscopy experiment. We obtain the best Raman signal by cliving the samples just before putting it under high-vacuum in the cryostat. With this preparation, we were able to recover a good signal at each temperature even if we notice a change in the intensity of modes depending on the position of the few micrometers spot on the surface.

On the other hand, IR spectroscopy is a bulk probe as the penetration depth in the reflectivity mode is of few micrometers, but the reflected intensity is very dependent on the quality of the crystal surface. The diameter of the incident light spot is of the same order of magnitude than the sample size ($\sim 700 \mu\text{m}$). In this case, we obtained a good reflective surface by polishing the sample with a mechanical *Leica* polisher using diamond grain-paper of $0.1 \mu\text{m}$.

2.4.3 Fourier Transform InfraRed (FTIR) Spectrometer

The FTIR is based on a Michelson interferometer (see Fig. 2.7) after which the recombined beam (interferogram) proceeds through the sample and then the detector. The advantage of an FTIR spectrometer is that it exposes the sample to all available infrared light frequencies simultaneously. Therefore, each portion of the interferogram contains encoded information of the sample that was derived from every infrared frequency it was exposed to. In parallel of the infrared interferogram, the spectrometer also acquires a laser interferogram for every scan, used to sample the infrared interferogram. The detector sends the signal toward a computer and with the help of a Fourier transformation, we obtain the plot of the intensity as a function of frequency.

The FTIR spectrometer used at ESPCI is a *Bruker IFS66/s*, composed of several chambers. The source is in the same chamber than the Michelson interferometer. Because our sample absorbs all frequencies in the IR range, we performed the measurement in the reflectivity configuration. The sample is mounted out of the spectrometer in a cryostat sitting just in front of the sample chamber. The detector is also moved out of the detector chamber and mounted beside the sample cryostat. We performed two series of measurements as a function of temperature.

- In the far-infrared range [$20\text{-}700 \text{ cm}^{-1}$], using a *Globar SiC* source, a *Mylar-Germanium* beamsplitter and a *Bolometer* as detector and a resolution of 2 cm^{-1} .
- In the mid-infrared region, we used the *Globar SiC* source combined with a *KBr:Germanium* beamsplitter, a *4.2 K Photoconductor* and a resolution of 4 cm^{-1} (for a reasonable time of acquisition $\sim 10 \text{ min}$).

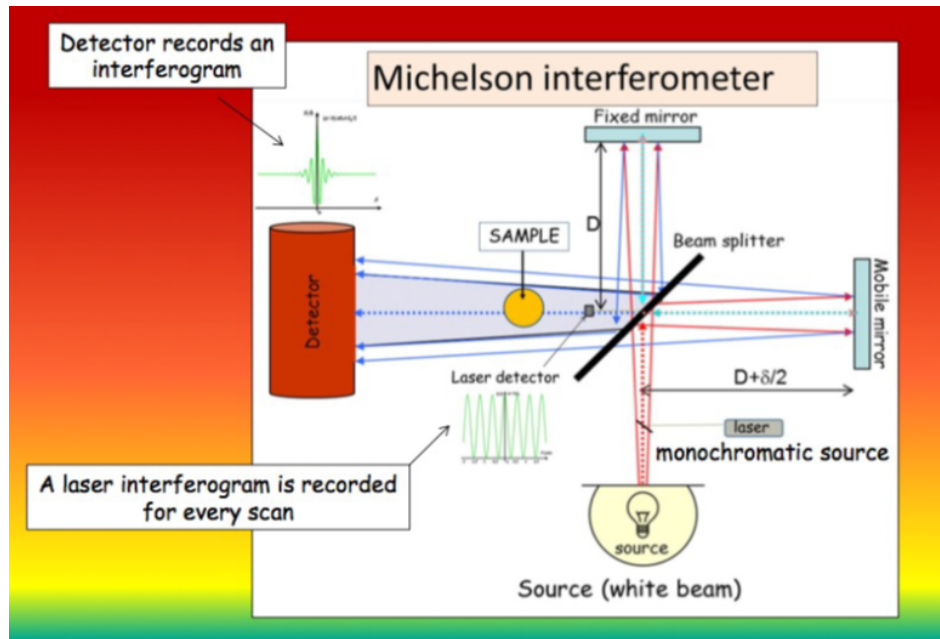


Figure 2.7: Scheme of the Michelson interferometer and path of the light in the FTIR spectrometer at ESPCI.

In order to avoid defects due to the small and irregular shape of our single-crystal we used the *in-situ gold overfilling technique* [59] which consists of coating the sample surface with a good metal (gold) and using the coated sample as its own reference in reflectivity measurements. This is realised by applying a DC voltage of about 2 V on a gold filament placed in proximity of the sample inside the cryostat. When applying the voltage, the filament glows and the gold is evaporated, this produces a layer of gold on the surface of the sample. The thickness of the gold layer is about several times the classical skin depth, even in the far-infrared range ($\sim 100 \text{ cm}^{-1}$) which ensures that multiple reflections do not occur. The procedure of the reflectivity measurement with this technique is as follows:

1. Measure the single channel power spectrum of the steel mirror I_{mirror} .
2. Rotate the cryostat and measure the single channel power spectrum of the sample I_{sample} .
3. Repeat at each temperature.
4. Evaporate gold on the surface of the sample.

5. Measure the single channel of the steel mirror again.
6. Rotate the cryostat and measure the single channel power spectrum of the coated sample and get $I_{coatedSample}/I_{mirror}$.
7. Do it at low and few intermediate temperatures.
8. Obtain the reflectivity of the sample:

$$R_{sample}(\omega) = \frac{I_{sample}(\omega)/I_{mirror}(\omega)}{I_{coatedSample}(\omega)/I_{mirror}(\omega)} \times R_{gold} \quad (2.3)$$

The use of a steel reference mirror between each measurement on the sample is to reduce the influence of the system drift. With the in-situ gold overfling technique, the measured reflectivity has absolute accuracy of 0.5% and relative accuracy of 0.1%.

2.4.4 Triple-stage Raman spectrometer

The triple-stage Raman spectrometer available at the IMPMC is represented in Fig. 2.8. It is a *T64000* designed by *Jobin-Yvon/Horiba* equipped with a CCD camera. We used an Argon Laser ($\lambda = 514.5$ nm) as source of monochromatic radiation, a set of optics to focus the laser onto the sample and the spectrometer in the backscattering geometry to analyse the scattered light. The spectrometer is made of 3 gratings: the first grating disperses the light at different angles as a function of the wavelength. This dispersed light goes through a slit which selects the desired spectral domain and cuts the strong undesired elastic *Rayleigh scattering*. The second grating recomposes the light spectrum without the Rayleigh scattering. The third grating disperses the light again on a bidimensional CCD detector branched to a PC software which translates the scattered light (in counts) as a function of the wavenumber ($1/\lambda$). The CCD camera is cooled down by liquid Nitrogen in order to reduce thermal noise. The triple-stage set-up permits to reach a high resolution of ~ 0.2 cm⁻¹ but reduces the intensity of signal which forces us to performed long acquisitions (~ 1 hour for 1 spectrum).

To ensure a good thermalization of the sample, we used silver paste to mount the samples on the cold head of a liquid-helium flow cryostat, kept under a high vacuum of 10⁻⁶ mBar. By monitoring the signal as a function of the beam power measured before

2.4. Spectroscopy techniques

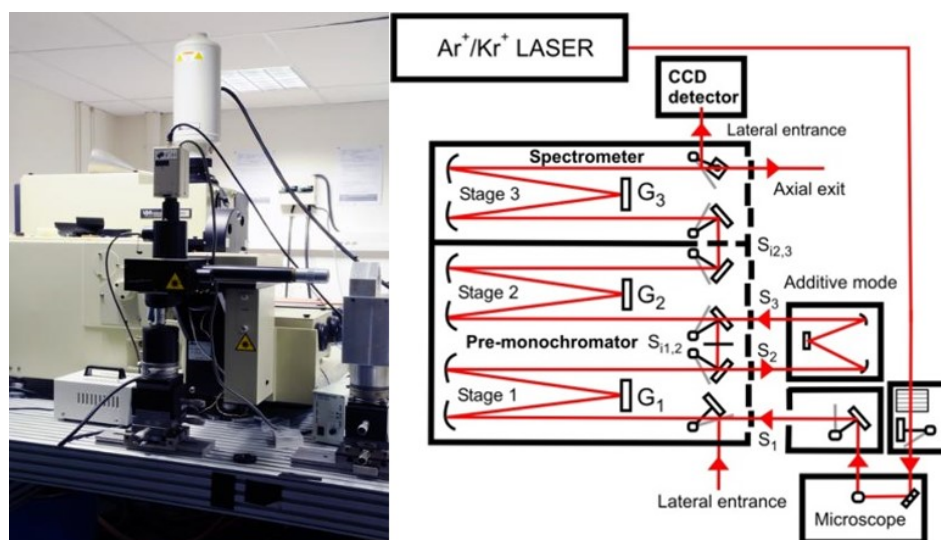


Figure 2.8: Left: The T64000 Raman spectrometer installed at the IMPMC. Right: Scheme of the path of light inside the spectrometer.

the optical window of the cryostat, we verified that sample heating is prevented using power up to 8 mW, so we decided to use a 5 mW beam. We performed several tests on different positions of the spot ($\sim 5\mu m$) on the surface of several samples and chose the position which gives the better signal. Because of thermal contraction, it is necessary to move the sample between each temperature set-point in order to keep the laser spot onto the same point of surface.

2.5 Ferroelectric characterizations

Ferroelectric characterizations have been performed at IMEM-CNR for the $(\text{YMn}_3)\text{Mn}_4\text{O}_{12}$, and at the University of Sao Carlos for $(\text{LaMn}_3)\text{Mn}_4\text{O}_{12}$, on polycrystalline samples previously polished onto disk shape with surface of $\sim 2/4 \text{ mm}^2$ and of different thickness between 630 and 58 μm . These disks are contacted on both faces with silver paste in order to make the electrodes. Temperature control was obtained either by placing the sample in a commercial SQUID or by using a homemade cryostat connected with a *Sumimoto CSW-71* cryocooler.

2.5.1 Pyroelectric currents

Pyroelectricity is the ability of a material of holding an intrinsic electric polarization when temperature is lowered. If this polarization can be changed or reversed by an applied electric field and follows an hysteresis cycle, the material is said to be ferroelectric. The temperature at which appears the spontaneous polarization is called the Curie Temperature (T_c). After having poled the sample and when going through the ferroelectric transition, from low to high temperature, the polarization is released and a pyroelectric current is measured between the two electrodes of the sample. By measuring this pyroelectric current I_p as a function of the temperature T with a constant warming rate τ , we obtain the value of the polarization P by a simple integration.

$$P = \frac{1}{S\tau} \int I_p dT \quad (2.4)$$

with S the surface of the disk. The procedure for pyroelectric measurements is:

1. Cooled down the sample from high temperature T_p to low temperature in the presence of a poling voltage V_p applied with the help of a source meter *Keithley 2400*.
2. Release the poling voltage.
3. Measure the current between the two electrodes as a function of increasing temperature with a constant warming rate with the help of a *keithley 6517B*.

This technique measures the relaxation of charges as a function of temperature and does not avoid the contribution of extrinsic charges to the total measured current. As detailed in chapters 3 and 6, specific measurements are needed to identify the intrinsic nature of the polarization measured by the pyrocurrent technique.

2.5.2 Dielectric constant

A dielectric material can be modeled by an equivalent electric circuit with one capacitor and one resistor in parallel. The resistor, and the value of its conductance $G = 1/R$, expresses the ability of the material of conducting the current and the capacitor, and the value of its capacitance, the ability of storing an electric charge. By using a bridge *LCR HP4824A* covering the frequency (ω) range from 20 to 10^6 Hz, we are able to measure the complex impedance:

$$Z = \frac{1}{G + i\omega C} \quad (2.5)$$

and thus deduce the capacitance C of the system. From this quantity we can obtain the low-frequency relative permittivity also called dielectric constant ϵ_r defined as the proportionality factor between an applied electric field \vec{E} and the induced electric displacement \vec{D} in the material:

$$\epsilon_r = \frac{1}{\epsilon_0} C \frac{d}{S} \quad (2.6)$$

with d the thickness and S the surface area of the sample.

Chapter 3

Multiferroic properties of (LaMn₃)Mn₄O₁₂

3.1 Introduction

Comme reporté par Prodi *et al.* [46], (LaMn₃)Mn₄O₁₂ présente une structure antiferromagnétique simple et commensurable. De plus, tous les ions manganèse de la structure sont dans le même état de valence Mn³⁺. Cela constitue une simplification majeure par rapport au (CaMn₃)Mn₄O₁₂ et font de ce composé un système modèle pour l'étude de la ferroélectricité magnétiquement induite dans les pérovskites quadruples de manganèse. Lorsque j'ai commencé ma thèse, des mesures préliminaires de courant pyroélectrique avaient été réalisées dans le cadre d'une collaboration avec l'université de São Carlos au Brésil et indiquaient l'apparition d'une polarisation à la transition magnétique des sites *B*. De nouvelles mesures étaient nécessaires pour confirmer ce résultat, notamment des mesures en fonction du taux de réchauffement pour vérifier le caractère intrinsèque de la polarisation et à plus fort champs de polarisation pour atteindre la saturation dans l'échantillon. Pour cela, il fallait réaliser des échantillons les plus fins possible et avec deux faces parallèles. J'ai donc réalisé la synthèse et le polissage de nouveaux échantillons de (LaMn₃)Mn₄O₁₂ polycristallins permettant de réaliser les mesures électriques et magnétiques. Idéalement, nous aurions voulu faire ces mesures sur des monocristaux mais leur petite taille ne le permettait pas. En effet, seuls des monocristaux de très petite taille ($\sim 10 \mu\text{m}$) ont pu être extraits des synthèses, mono-cristaux avec lesquels nous avons réalisé des mesures de diffraction à température ambiante en laboratoire

(IMPMC) et à basse température au synchrotron SOLEIL dans le cadre du projet BAG de B. Baptiste. Les données de diffraction de rayons X sur poudre en fonction de la température présentées dans ce chapitre avaient déjà été obtenues avant le début de ma thèse. L'ensemble des résultats reportés dans ce chapitre montre l'existence de propriétés multiferroïques remarquables dans $(\text{LaMn}_3)\text{Mn}_4\text{O}_{12}$, caractérisées par une grande valeur de la polarisation $P_{sat} = 0.54 \mu\text{m cm}^{-2}$ apparaissant à la transition magnétique et un large effet magnétoélectrique révélés par des mesures de pyrocourants et de magnétisation sous champ électrique, respectivement. En revanche, les données de diffraction ne permettent pas de conclure à une perte du centre d'inversion attendue pour expliquer l'apparition de la ferroélectricité.

3.2 Article I: Large ferroelectricity induced by collinear magnetism in the quadruple perovskite $(\text{LaMn}_3)\text{Mn}_4\text{O}_{12}$

STATUS: In preparation

Large ferroelectricity induced by collinear magnetism in the quadruple perovskite $(\text{LaMn}_3)\text{Mn}_4\text{O}_{12}$

A. Gauzzi,^{1,*} F. Milton,² V. Pascotto Gastaldo,² A. Gualdi,² M. Verseils,¹ B. Baptiste,¹ P. Bordet,³ D. Garcia,² A.J.A. De Oliveira,², E. Gilioli,⁴

¹*IMPMC, Sorbonne Universités-Université P. et M. Curie, CNRS, IRD, MNHN, 4, place Jussieu, 75005 Paris, France*

²*Grupo de Supercondutividade e Magnetismo, Departamento de Física, Universidade Federal de São Carlos, Rodovia Washington Luís, km 235, São Carlos - São Paulo, Brazil*

³*Institut Néel, CNRS and Université Grenoble Alpes, BP 166, 38042 Grenoble, France*

⁴*Istituto dei Materiali per Elettronica e Magnetismo-CNR, Area delle Scienze, 43100 Parma, Italy*

Abstract

Pyroelectric current and magnetoelectric coupling measurements on polycrystalline samples of the quadruple perovskite $(\text{LaMn}_3)\text{Mn}_4\text{O}_{12}$ give evidence of ferroelectricity driven by the antiferromagnetic ordering of the B -site Mn^{3+} ions at $T_{N,B}=78$ K with record values of remnant electric polarization up to $P=0.54 \mu\text{C cm}^{-2}$ at saturation. X-ray diffraction measurements indicate an anomalous behavior of the monoclinic β angle at $T_{N,B}$, which suggests that P lies in the ac -plane, where the moments are collinear, and the magnetic structure of the system already reported in a previous work [46] allows us to conclude that exchange striction in the ac -plane is the mechanism of spin-driven ferroelectricity. Polarization values $\sim 3 \mu\text{C cm}^{-2}$ are expected in single crystals, which would open the avenue towards practical multiferroic applications.

I. INTRODUCTION

In the search for suitable multiferroic materials for applications, recently there has been an increasing interest in magnetic ferroelectrics (MFs), where the ferroelectric order is induced by the magnetic order, for this mechanism leads to inherently strong magnetoelectric coupling [60]. On the other hand, the remnant polarizations, P , hitherto reported in these ferroelectrics typically fall in the $\sim 0.1 \mu\text{C cm}^{-2}$ range or below, with the exception of the distorted perovskite compound TbMnO_3 , where values $\sim 1 \mu\text{C cm}^{-2}$ have been reached under high pressures [61]. On the other hand, values in the $10 \mu\text{C cm}^{-2}$ range are required for applications. It is believed that such small P values reflect the weakness of the spin-orbit interaction in non-collinear chiral spin structures [14], where the polarization arises from the antisymmetric exchange striction (Dzyaloshinskii-Moriya interaction) between neighbouring i and j spins, *i.e.* $P \propto |\mathbf{s}_i \times \mathbf{s}_j|$. The attention has then been drawn to collinear spin structures, where large $P \propto |\mathbf{s}_i \cdot \mathbf{s}_j| \gtrsim 1 \mu\text{C cm}^{-2}$ induced by the stronger symmetric exchange striction has been predicted [36]. This possibility is supported by the aforementioned observation of stronger ferroelectricity induced by a collinear E -structure in the above $R\text{MnO}_3$ system (R rare earth). Recently manganese oxides with the quadruple perovskite $(A\text{Mn}_3)\text{Mn}_4\text{O}_{12}$ structure, which contains two distinct A' and B Mn sites [42], have attracted the attention of the multiferroic community thanks to the observation of an enhancement of $P \sim 0.3 \mu\text{C cm}^{-2}$ in single crystalline samples of $(\text{CaMn}_3)\text{Mn}_4\text{O}_{12}$ [40, 41]. This discovery has triggered a number of studies aiming at understanding the origin of this large polarization [49, 62] which may foster the design of multiferroics with even larger P values. On the other hand, in this compound, the polarization is concomitant to a complex interplay of an incommensurate helicoidal spin structure and of a charge and orbital ordering of the Mn^{3+} and Mn^{4+} ions [48]. This hampers a comparison between experiment and theory and to identify the distinct contributions of the symmetric and antisymmetric exchange terms to the polarization. In conclusion, in spite of the increasingly large P values reported recently, the mechanism of P enhancement in magnetic multiferroics remains controversial.

Further progress in the field requires model systems where the principal contributions can be clearly identified and controlled. In order to respond to this need, in the

present work, we focus our attention on the multiferroic properties of $(\text{LaMn}_3)\text{Mn}_4\text{O}_{12}$ [46], where similar multiferroic properties are expected since this compound shares with $(\text{CaMn}_3)\text{Mn}_4\text{O}_{12}$ a similar quadruple perovskite structure and similar electronic properties. Our choice is motivated by the fact that, in spite of these similarities, $(\text{LaMn}_3)\text{Mn}_4\text{O}_{12}$ exhibits comparatively simple structural and electronic properties, namely single-valent Mn^{3+} characteristics and a simple C -type antiferromagnetic (AFM) order of the B -site Mn^{3+} ions at $T_{N,B}=78$ K consisting of collinear antiferromagnetic spins within the ac -plane canted along the b -axis, as reported in [46]. Consequently, unlike $(\text{CaMn}_3)\text{Mn}_4\text{O}_{12}$, in $(\text{LaMn}_3)\text{Mn}_4\text{O}_{12}$ there is no charge-ordering phenomena, nor incommensurate structural modulations are found. Besides, the magnetic structure of B -sites imposes that the average contribution to the polarization of the antisymmetric exchange term (Dzyaloshinskii-Moriya interaction) is zero. The crystal structure undergoes a cubic $Im\bar{3}$ to monoclinic $I2/m$ distortion at 653 K [63] and, within the experimental resolution of powder neutron reported in [46], no further structural phase transitions are observed at low temperatures down to 3.5 K.

II. EXPERIMENTAL

Poly- and single-crystalline samples of $(\text{LaMn}_3)\text{Mn}_4\text{O}_{12}$ were synthesized under high-pressure as described elsewhere [46]. Different poly- or single-crystalline morphologies are obtained by varying the temperature during synthesis. Previous powder neutron diffraction structural studies revealed that the samples are 95 % pure or better and that the samples contain minor impurities of LaMnO_3 and Mn_3O_4 . The as-prepared samples are compact cylinders of 4 mm size in diameter and height that were sliced in order to obtain thin disks of 0.2 - 0.3 mm thickness. In order to investigate the multiferroic properties by means of pyrocurrent and magnetoelectric coupling measurements, a thin Au layer was deposited on both sides by magnetron sputtering.

For the pyroelectric measurements, such metallized disks were subsequently mounted on a closed-cycle cryostat. Pyrocurrents are measured between the two contacted faces, upon warming up the disk using a *Keithley* electrometer and after having poled the sample at high temperature by applying some appropriated voltage.

In order to unveil the interplay between multiferroic and structural properties, the powders were investigated by means of x-ray diffraction as a function of temperature using a *Nonius Kappa-CCD* laboratory diffractometer equipped with a liquid helium bath cryostat and a Mo- $K\alpha$ source.

Finally, the possibility of fine structural changes or structural modulations occurring at the AFM ordering transition, $T_{N,B}$, was investigated by means of single-crystal x-ray diffraction, carried out at room temperature in a commercial *Excalibur* diffractometer equipped with a Mo K_α source ($\lambda = 0.71073 \text{ \AA}$) and at low temperature at the CRISTAL beamline ($\lambda = 0.6717 \text{ \AA}$) of the french synchrotron SOLEIL.

III. RESULTS

In Fig. 3.1, we show the refined unit cell parameters obtained from x-ray powder diffraction data as a function of temperature in the 9-300 K range. Within the experimental resolution, no anomalous behavior is found for any of these parameters, except for the monoclinic angle, β , which displays an abrupt increase of slope at $T_{N,B}$, which confirms previous powder neutron diffraction data [46]. This indicates a sizable magnetoelastic coupling which tends to stretch the *ac*-plane along the diagonal without appreciable change of unit-cell volume.

Pyroelectric current and magnetoelectric coupling measurements show that this structural distortion is concomitant to the appearance of ferroelectricity. A summary of the results of the former measurements is given in Figs. 3.2, 3.3. Fig. 3.2 shows the temperature dependence of the pyrocurrent measured at different heating rates for a poling voltage of 900 V, corresponding to a field of 36 kV cm^{-1} . The data consistently show a pronounced peak in the vicinity of $T_{N,B}$, which is the evidence of ferroelectricity induced by the AFM ordering of the *B*-site Mn^{3+} ions. The measurement gave reproducible results for two different samples and was extended to high temperatures in order to rule out the possible contribution of leakage currents or space charges. For instance, from Fig. 3.2, one notes that, for sufficiently low heating rates, the pyroelectric current vanishes above 100 K; a possible contribution of thermally activated space charges to the pyroelectric current occurs only above 120 K. One also notes a small pyrocurrent peak at $T_{N,A'}$, which indicates a minor contribution of the AFM ordering of the *A'*-sites.

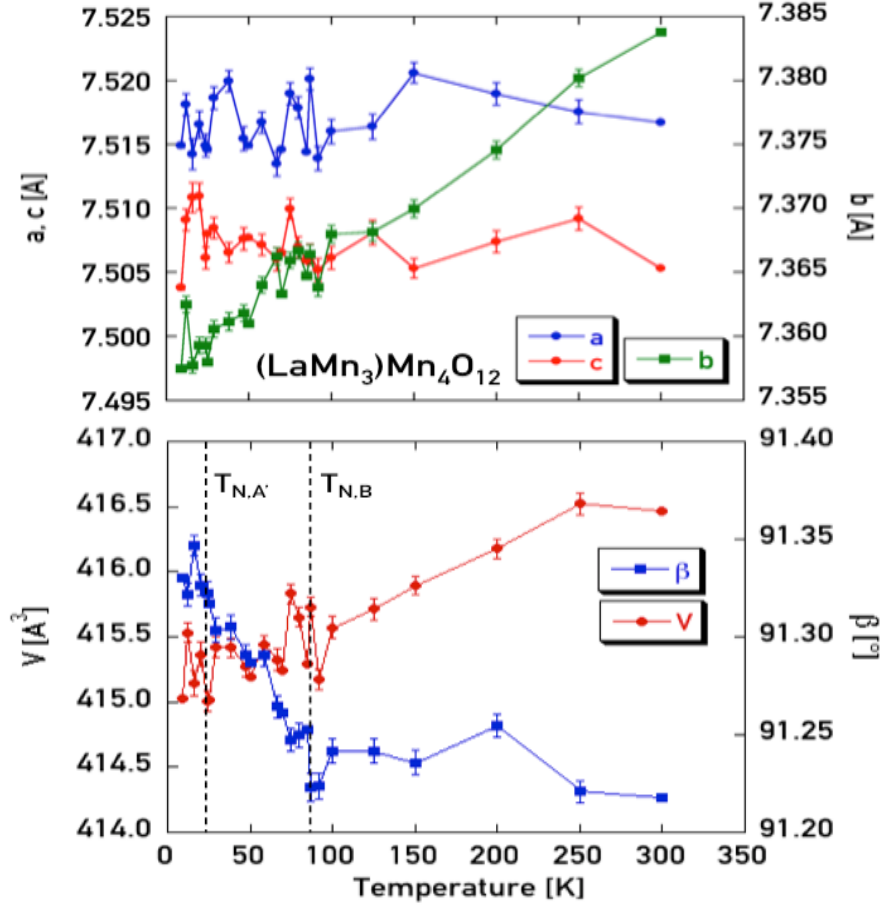


Figure 3.1: Temperature dependence of the unit cell parameters and of the unit cell volume, V , of the monoclinic crystal structure of $(\text{LaMn}_3)\text{Mn}_4\text{O}_{12}$ powders. Note the sudden increase of the monoclinic angle, β , at the antiferromagnetic ordering temperature of the B -site Mn^{3+} ions, $T_{N,B}=78$ K, which indicates a large magnetoelastic coupling.

In Fig. 3.3, we show the temperature dependence of the remnant polarization $P(T)$ obtained by integrating the pyroelectric current curves measured at a heating rate of 1 K/min for three different poling fields of 12, 24 and 36 kV cm^{-1} . As expected, the value of remnant polarization increases with poling field and a value as high as $P = 0.45 \mu\text{C cm}^{-2}$ is reached at the lowest temperature measured of 15 K. The dependence of P on poling field plotted in the inset shows that the saturation of the polarization was not reached. A simple fit of this dependence, using a classic Langevin function, suggests a saturation polarization as high as $P_{sat} = 0.54 \mu\text{C cm}^{-2}$. To the best of our knowledge,

these are record value for magnetic ferroelectrics, twice as large as the value previously reported on $(\text{CaMn}_3)\text{Mn}_4\text{O}_{12}$ [40, 41]. Furthermore, as said before, about 6-10 times larger polarizations are expected in high-quality single crystalline films or bulk samples [64]. Hence, in such samples of $(\text{LaMn}_3)\text{Mn}_4\text{O}_{12}$, polarizations in the $1\text{-}10 \mu\text{C cm}^{-2}$ range are expected.

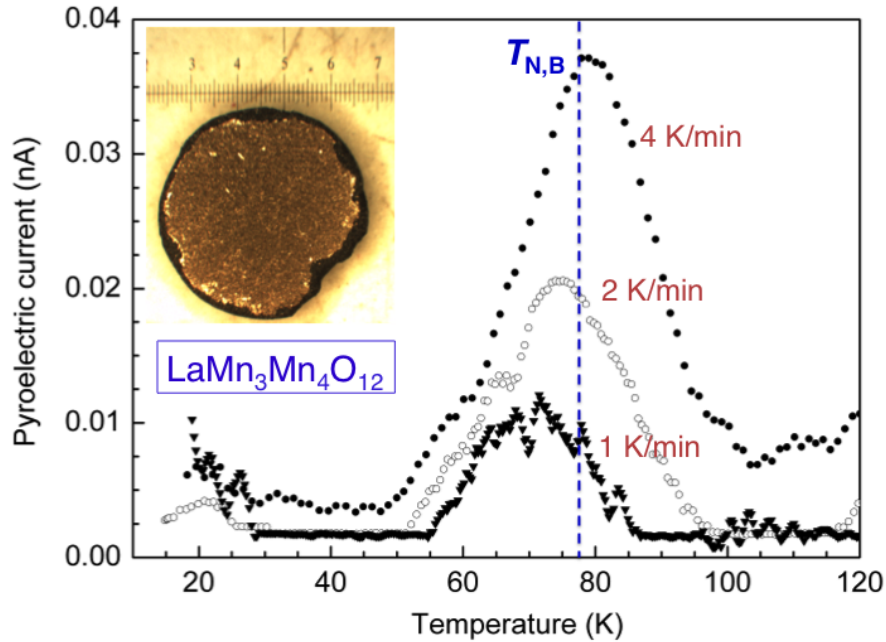


Figure 3.2: Pyrocurrent curves measured at different heating rates for a poling voltage of 900 V on a 0.25 mm thin disk made of $(\text{LaMn}_3)\text{Mn}_4\text{O}_{12}$ sintered powders. Note the peak of pyrocurrent located near the antiferromagnetic ordering temperature, $T_{N,B}=78$ K. The inset shows the disk covered by a Au layer for metallization, as described in the experimental section.

In order to confirm the picture of magnetic ferroelectricity in $(\text{LaMn}_3)\text{Mn}_4\text{O}_{12}$, we have carried out magnetoelectric measurements on a similar metallized disk by measuring the dc magnetization as a function of temperature, $M(T)$, before and after poling the sample with a 30 V voltage, corresponding to an electric field of 400 V cm^{-1} . The curves shown in Fig. 3.4 exhibit a large difference in the magnetization, caused by the poling field, at the AFM ordering temperatures of both A' - and B -site Mn^{3+} ions, $T_{N,A'}=21$ K and $T_{N,B}=78$ K. This gives evidence of a magnetoelectric coupling involving the magnetic moments at both sites. The largest effect is observed at $T_{N,B}$, in agree-

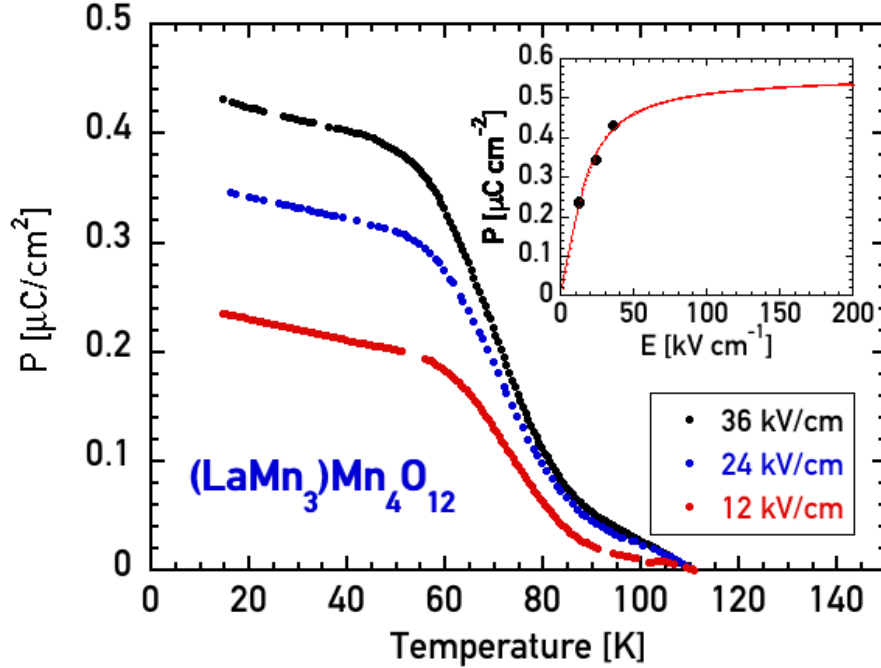


Figure 3.3: Remnant polarization, P , of the polycrystalline $(\text{LaMn}_3)\text{Mn}_4\text{O}_{12}$ sample of Fig. 2 obtained by integrating the pyrocurrent curves measured at different poling voltages. Inset: dependence of P upon poling field. A fit of the experimental points by using a Langevin function indicates a saturation value $P=0.54 \mu\text{C}/\text{cm}^2$.

ment with our previous observation that the dominant contribution to the pyrocurrent occurs at this temperature.

IV. DISCUSSION

The above results raise a number of questions:

(i) The observation of a spontaneous ferroelectric polarization driven by the AFM ordering of the B -site Mn^{3+} ions and concomitant to a large magnetoelastic response of the monoclinic β angle, strongly indicates that the polarization lies along the ac -diagonal. Within the ac -plane the magnetic structure displays AFM coupled collinear moments. Since the magnetic structure of B -sites is responsible for a zero average contribution to P of the antisymmetric exchange striction, we conclude that the macroscopic mechanism of spin-driven ferroelectricity is the symmetric exchange coupling within the ac -plane, consistent with the large polarizations observed. Indeed, in the alternative scenario of antisymmetric exchange (or inverse Dzyaloshinskii-Moriya)

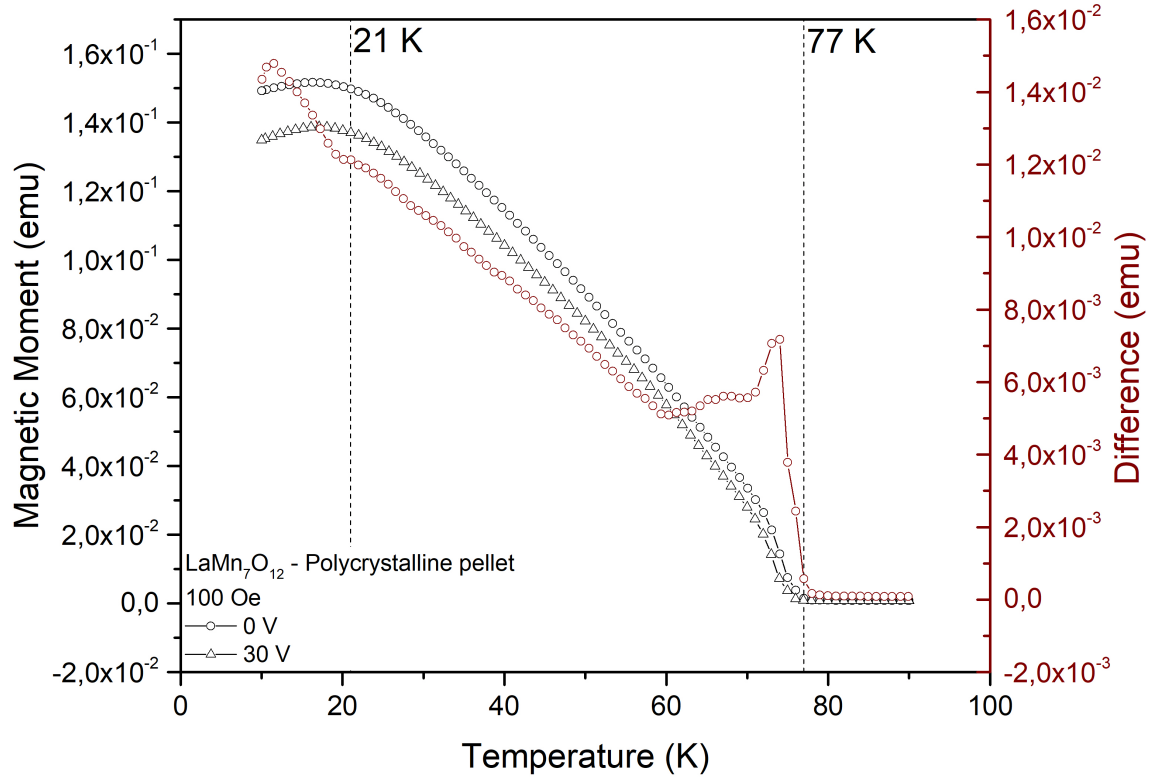


Figure 3.4: Left axis: magnetization curve of a polycrystalline $(\text{LaMn}_3)\text{Mn}_4\text{O}_{12}$ sample measured in a field of 100 Oe before and after the application of a poling field of 30 V. Right axis: difference between the two magnetization curves showing the magneto-electric coupling at the two AFM ordering temperatures $T_{N,B}=78$ K and $T_{N,A'}=21$ K of the of the B -site and A' -site Mn^{3+} ions, respectively.

contribution, smaller polarizations would be expected.

(ii) We experimentally found that the magnetic ferroelectricity is dominated by the magnetic structure of the B -sites, while the magnetic structure of the A' -sites gives a much smaller contribution. We recall that the latter structure is made of ferromagnetic (FM) planes in the ac -plane AFM coupled along the b -axis and that the moments are oriented along this latter axis [46]. Both structures are commensurate and rather simple, so it might be possible to explain theoretically why the former structure is more favorable for ferroelectricity.

(iii) The existence of a large polarization below $T_{N,B}$ would imply sizable noncentrosymmetric structural distortion below this temperature. It is well known that it is experimentally difficult to detect these distortions by means of ordinary diffraction experiments when they are small and second-harmonic generation (SHG) experiments are a more direct probe. In the present case, the SHG technique is not suitable either for $(\text{LaMn}_3)\text{Mn}_4\text{O}_{12}$ as it is a narrow-gap semiconductor with $\Delta=60$ meV, as indicated by resistivity [46] and optical conductivity measurements. Therefore, in the present case, we limit ourselves to compare the crystal structures measured at 300 and 50 K on high quality single crystals by means of x-ray diffraction. The two refined structures are reported in Table I. The aim of this comparison is to detect any anomalous value of thermal parameter or the appearance of satellite peaks that may reveal a noncentrosymmetric structural distortion or modulation, following a similar analysis performed previously on the proper ferroelectric $(\text{BiMn}_3)\text{Mn}_4\text{O}_{12}$, where the polar Bi^{3+} was found to induce a spontaneous polarization in the $I2/m$ quadruple perovskite structure [65]. No additional satellite peaks were observed at low temperature. The high quality of the structural refinement enables us to conclude that, in the present case, the $I2/m$ symmetry describes well the crystal structure in both, para- and ferro-electric phases above and below $T_{N,B}$. This conclusion is consistent with previous reports on the lack of noncentrosymmetric distortions in other magnetic ferroelectrics [66, 11, 31]. By means of resonant magnetic x-ray scattering, Walker *et al.* [67] succeeded in detecting minute fm-size modulations of atomic displacements in the simple perovskite TbMnO_3 . This compound exhibits remnant polarizations one order of magnitude smaller than that reported here, thus we expect that much larger structural modulations should be observed in $(\text{LaMn}_3)\text{Mn}_4\text{O}_{12}$ single crystals or thin films, but resulting in a long-range centrosymmetric structure.

(iv) The very large polarizations found in $(\text{CaMn}_3)\text{Mn}_4\text{O}_{12}$ and $(\text{LaMn}_3)\text{Mn}_4\text{O}_{12}$ suggest that manganese oxides with quadruple perovskite structure, described by the general formula $(\text{AMn}_3)\text{Mn}_4\text{O}_{12}$, where A is a di- or three-valent cation, are particularly favorable for hosting large magnetic ferroelectricity. Further theoretical and experimental studies are needed to elucidate this point, which goes beyond the scope of this work. To stimulate further work, we limit ourselves to recall the peculiar features of

quadruple perovskites not found in simple perovskites that may be associated with the observation of large magnetic ferroelectricity [68]. 1) In all $(\text{AMn}_3)\text{Mn}_4\text{O}_{12}$ compounds hitherto reported, no indication of oxygen defects has been found, which is attributed to the fact that oxygen vacancies would destabilize the bonding of the low-coordination number of the A' sites. 2) In quadruple perovskites, the symmetry of the oxygen sites is comparatively high as compared to that of distorted simple perovskites, which limits strain-induced lattice distortions of the oxygen sublattice. As a result, the ability of the oxygen atoms to screen the electric dipole moment formed by the distortion of the Mn sublattice is also reduced. An extensive low-temperature structural study of the ferroelectric phase of $(\text{LaMn}_3)\text{Mn}_4\text{O}_{12}$ is required to verify this scenario.

V. CONCLUSION

In conclusion, we have reported a ferroelectric phase, with a record value of remnant polarization, $P_{\text{sat}}=0.54 \mu\text{C cm}^{-2}$ in the quadruple perovskite compound $(\text{LaMn}_3)\text{Mn}_4\text{O}_{12}$, concomitant to a C -type AFM ordering of the B -site Mn^{3+} ions at $T_{N,B}=78$ K. This observation is accompanied by the evidence of a sizable magnetostriction of the unit cell and of a very large magnetoelectric coupling at the same temperature. This result is striking in two aspects. (i) Considering that the above polarizations, twice as large as that found in $(\text{CaMn}_3)\text{Mn}_4\text{O}_{12}$ single crystals, have been obtained on polycrystalline samples, 6-10 times larger values are expected in high-quality single crystalline films or bulk samples [64]. This would correspond to extremely large values, $\sim 3 - 6 \mu\text{C cm}^{-2}$, comparable to those obtained in proper ferroelectrics, which would open the avenue towards multiferroic applications. (ii) If the above picture of polarization in the ac -plane will be confirmed, the unique magnetic contribution to polarization would come from the exchange-contraction mechanism within the ac -plane. This result provides clear hints for the optimization of the multiferroic properties of magnetic ferroelectrics and we envisage that even better multiferroic performances may be found among novel quadruple perovskites.

3.2. Article I: Large ferroelectricity induced by collinear magnetism in the quadruple perovskite (LaMn₃)Mn₄O₁₂

Temperature	300 K	50 K
Radiation	MoK $_{\alpha}$ $\lambda=0.71073$ Å	Synchrotron $\lambda=0.6717$ Å
$a,b,c(\text{Å})$	7.5072(5),7.3752(5),7.5164(5)	7.4980(4),7.3660(3),7.5055(4)
$\beta(^{\circ}),V(\text{Å})^3$	91.268(6), 416.06(5)	91.187(6), 414.44(3)
La 2a (0,0,0)		
U_{eq}	0.0089(4)	0.0029(3)
U_{11}, U_{22}, U_{33}	0.0078(5), 0.0091(5), 0.0098(5)	0.0035(4), 0.0027(3), 0.0025(4)
U_{23}, U_{13}, U_{12}	0, -0.0009(3),0	0, -0.0014(3),0
Mn A' 2b (0,1/2,0)		
U_{eq}	0.0096(5)	0.0030(4)
U_{11}, U_{22}, U_{33}	0.0059(10), 0.007(1), 0.0158(11)	0.0020(8), 0.0019(7), 0.0052(8)
U_{23}, U_{13}, U_{12}	0, -0.0013(9),0	0, -0.0001(7),0
Mn A' 2c (1/2,0,0)		
U_{eq}	0.0105(5)	0.0032(4)
U_{11}, U_{22}, U_{33}	0.0065(10), 0.0172(12), 0.0077(10)	0.0015(9), 0.0069(7), 0.0012(8)
U_{23}, U_{13}, U_{12}	0, -0.0011(8),0	0, 0.0005(7),0
Mn A' 2d (1/2,1/2,0)		
U_{eq}	0.0090(5)	0.0035(4)
U_{11}, U_{22}, U_{33}	0.0134(11), 0.0063(10), 0.0072(10)	0.0061(9), 0.0025(7), 0.0018(8)
U_{23}, U_{13}, U_{12}	0, -0.0013(9),0	0, 0.0001(7),0
Mn B 4e (1/4,1/4,1/4)		
U_{eq}	0.0068(4)	0.0025(3)
U_{11}, U_{22}, U_{33}	0.0053(8), 0.0077(8), 0.0074(8)	0.0028(7), 0.0033(6), 0.0014(7)
U_{23}, U_{13}, U_{12}	0.0000(5), -0.0012(7),0.0007(4)	0.0000(3), -0.0006(6),-0.0001(-3)
Mn B 4f (1/4,1/4,3/4)		
U_{eq}	0.0068(4)	0.0025(3)
U_{11}, U_{22}, U_{33}	0.0050(8), 0.0063(8), 0.0090(9)	0.0027(7), 0.0022(6), 0.0026(7)
U_{23}, U_{13}, U_{12}	-0.0001(5), -0.0011(7),-0.0001(4)	0.0001(3), -0.0005(6),-0.0001(3)
O1 4i (x,1/2,z)		
x,z	0.1850(7),0.6813(8)	0.1869(6),0.6783(6)
U_{eq}	0.0098(12)	0.0027(9)
U_{11}, U_{22}, U_{33}	0.008(3), 0.008(3), 0.014(3)	0.001(2), 0.0052(19), 0.002(2)
U_{23}, U_{13}, U_{12}	0, -0.001(2),0	0, -0.0002(18),0
O2 4i (x,1/2,z)		
x,z	-0.1920(7),0.6688(7)	-0.1921(6),0.6685(6)
U_{eq}	0.0086(12)	0.0032(9)
U_{11}, U_{22}, U_{33}	0.006(3), 0.012(3), 0.007(3)	0.005(2), 0.0040(19), 0.001(2)
U_{23}, U_{13}, U_{12}	0, 0.005(2),0	0, 0.0015(19),0
O3 8j (x,y,z)		
x,y,z	0.4864(5),0.3244(5),0.8131(5)	0.4873(4),0.3244(4),0.8124(4)
U_{eq}	0.0091(9)	0.0052(7)
U_{11}, U_{22}, U_{33}	0.008(2), 0.009(2), 0.010(2)	0.0066(18), 0.0057(14), 0.0031(15)
U_{23}, U_{13}, U_{12}	-0.0037(17), -0.0016(17),-0.0006(15)	-0.0011(11), 0.0004(14),-0.0005(11)
O4 8j (x,y,z)		
x,y,z	0.6731(5),0.1895(5),0.5155(5)	0.6729(4),0.1904(4),0.5145(4)
U_{eq}	0.0084(9)	0.0052(7)
U_{11}, U_{22}, U_{33}	0.009(2), 0.0061(19), 0.0011(2)	0.0044(17), 0.0060(15), 0.0050(16)
U_{23}, U_{13}, U_{12}	-0.0007(17), 0.0010(17),-0.0028(15)	-0.0001(11), -0.0018(14),-0.0027(12)
R [all data]	R ₁ =0.0411, wR ₂ = 0.0995	R ₁ =0.0318, wR ₂ = 0.0795

Table 3.1: Crystal structure obtained from refinement in the $I2/m$ space-group of single-crystal x-ray diffraction data.

Chapter 4

Raman and IR spectroscopy study of the spin-lattice coupling in (LaMn₃)Mn₄O₁₂

4.1 Introduction

Comme décrit dans le chapitre précédent, (LaMn₃)Mn₄O₁₂ présente des propriétés multiferroïques remarquables, avec notamment la plus grande valeur de polarisation magnétiquement induite jamais reportée et un fort couplage magnétoélectrique. Cependant, aucune évidence de distorsions ferroélectriques n'a pu être identifiée par diffraction. Or, pour être ferroélectrique, un matériau doit forcément présenter des distorsions qui brisent le centre d'inversion. Ainsi, la question légitime est: Ce composé est-il vraiment ferroélectrique ? Si oui, existe-t-il un moyen d'observer les distorsions attendues, même minuscules (10^{-15} m) ? Une façon indirecte d'identifier les distorsions du réseau est d'observer l'évolution du spectre de phonons en fonction de la température. Pour cela, les techniques de spectroscopie infrarouge et Raman, ainsi que la mesure de la chaleur spécifique sont particulièrement appropriées. De plus, les techniques de spectroscopie permettent d'identifier les phonons qui se couplent aux propriétés multiferroïques. Durant ma thèse j'ai donc réalisé ces mesures en parallèle entre l'IMPMC et le laboratoire de R. Lobo à l'ESPCI et ce chapitre en présente les résultats ainsi qu'une interprétation théorique dans le cadre de la théorie phénoménologique des ferroélectriques impropres développée en 1974 par A. P. Levanyuk et D. G. Sannikov [13].

4.2 Article II: Evidence of strong magnetoelastic coupling driving magnetic ferroelectricity

STATUS: In preparation

Evidence of strong magnetoelastic coupling driving magnetic ferroelectricity in (LaMn₃)Mn₄O₁₂

M. Verseils,^{1,*} R.P.S.M. Lobo,^{2,3} Ch. Bellin,¹ P. Giura,¹ Y. Klein,¹ M.D'astuto,¹ A. Polian,¹ K. Beenut,¹ P.S. Pizani,⁴ A.J.A. De Oliveira,⁴ R. Cabassi,⁵ F. Bolzoni,⁵ E. Gilioli,⁵ and A. Gauzzi¹

¹*IMPMC, Sorbonne Universités-Université P. et M. Curie, CNRS, IRD, MNHN, 4, place Jussieu, 75005 Paris, France*

²*LPEM, ESPCI-ParisTech, CNRS, 10, rue Vauquelin, 75005 Paris, France*

³*Sorbonne Universités, Univ Paris 6, CNRS, LPEM 75005 Paris, France* ⁴*Grupo de Supercondutividade e Magnetismo, Departamento de Física, Universidade Federal de São Carlos, Rodovia Washington Luís, km 235, São Carlos - São Paulo, Brazil*

⁵*Istituto dei Materiali per Elettronica e Magnetismo-CNR, Area delle Scienze, 43100 Parma, Italy*

Abstract

We report on a systematic infrared (IR) optical conductivity and Raman spectroscopy study on single crystals of the magnetic ferroelectric quadruple perovskite (LaMn₃)Mn₄O₁₂ (LMO) as a function of temperature. We identified a large number of mutually exclusive IR and Raman modes consistent with a symmetry analysis applied to the centrosymmetric monoclinic $I2/m$ structure of LMO. We followed the temperature dependence of the strongest modes in the vicinity of the AFM ordering transition, $T_{N,B}$, at which an electric polarization appears. The IR modes display either a conventional hardening in the whole temperature studied or a phonon frequency renormalisation at the temperature of magnetic ordering of B -sites, $T_{N,B}$. The renormalisation corresponds to either a softening or hardening of the mode, similar to previous observations of AFM transitions in ordinary paraelectric materials, which is

explained by including an exchange coupling between neighboring spins to the hamiltonian of an elastic crystal. On the other hand, much more pronounced anomalies are observed at $T_{N,B}$ in the behavior of the Raman modes. These anomalies consist in a pronounced critical enhancement of the mode frequency followed by an abrupt drop. Both behaviors are explained qualitatively by previous phenomenological theories of improper ferroelectrics and suggest the existence of fluctuating ferroelectric domains in a long-range centrosymmetric structure. The magnitude of the anomalies observed in the behavior of the Raman modes points to a strong magnetoelastic coupling at $T_{N,B}$ concomitant to the onset of the fluctuating domains with no-long-range ferroelectric order in the absence of poling. Complementary specific heat measurements as a function of field carried out on polycrystalline samples show a large field-induced depression of the lattice specific heat which reaches $\sim 40\%$ at 2 K in a field of 9 T. This depression gives further evidence of an additional field-induced lattice hardening induced at $T_{N,B}$.

I. INTRODUCTION

Improper ferroelectricity, *i.e.* the appearance of a switchable macroscopic electric polarization induced by another order parameter, has been the object of experimental and theoretical studies since the 60's [69]. First observed in ammonium fluoroberyllate [70] and later in rare-earth molybdates [71, 72], this phenomenon has recently attracted a renewed interest in the case of magnetic ferroelectrics (MFs), where the principal order parameter is magnetic [73, 10, 74, 11, 75, 60, 76]. It is believed that these multiferroic materials are promising for applications, as the magnetoelectric coupling is inherently large it can be used to switch a magnetic domain by an electric field, or viceversa. This may lead to novel concepts of electronics devices, such as fast and low-power consuming non-volatile memories [14, 77, 7, 78] that would revolutionize electronics and information technologies.

While the phenomenological theory of magnetic ferroelectricity has been well established by including appropriate ME terms in the free energy [22, 21], the microscopic mechanisms suitable to explain the experimental behavior observed remain controversial. In spite of the important quantity of experimental data available and of the numerous MFs hitherto discovered, clear experimental signatures of the onset of ferroelectric

order, *e.g.* phonon anomalies at the critical temperature of magnetic ordering or non-centrosymmetric structural distortions, are surprisingly missing. For instance, the observed phonon anomalies in $(\text{CaMn}_3)\text{Mn}_4\text{O}_{12}$ and RMnO_3 multiferroics [79, 80, 81] are not substantially different from the modest mode renormalizations previously reported in ordinary paraelectric antiferromagnets like MnF_2 [82, 83]. These renormalizations, fully explained by second-order perturbation theory, consist in a deviation from the conventional mode-hardening with decreasing temperature predicted by Balkanski [84] and the magnitude of renormalization is proportional to the square of the magnetic order parameter (M) [85]. On the other hand, the structural distortions observed in the magnetic ferroelectrics previously studied are either minute modulations or not observed at all [66]. For example, in recent studies, it was reported that in TbMnO_3 the dipolar distortions associated with magnetically induced ferroelectricity are in the femtoscale [67, 86] and previous spectroscopy studies on this compound failed to detect a center of symmetry breaking [81]. One may argue that the reason of the missing signatures of the ferroelectric phase in MFs is the comparatively small polarization characteristic of these materials, typically smaller than $\sim 0.1 \mu\text{C cm}^{-2}$, which may hinder practical applications. However, no clear signature was reported in $(\text{CaMn}_3)\text{Mn}_4\text{O}_{12}$ either [87], where polarization is found to be as large as $\sim 0.3 \mu\text{C cm}^{-2}$ [40, 49, 41, 62].

Very recently, some of us reported (see chapter 3) record high polarizations $P_{sat} \sim 0.54 \mu\text{C cm}^{-2}$ induced by a C-type antiferromagnetic (AFM) order of the B -site Mn^{3+} ions in $(\text{LaMn}_3)\text{Mn}_4\text{O}_{12}$ (LMO), which shares a similar quadruple perovskite structure [46] with $(\text{CaMn}_3)\text{Mn}_4\text{O}_{12}$. These values, obtained far from saturation in polycrystalline samples, suggest that values in the $\sim 10 \mu\text{C cm}^{-2}$ range are expected in single crystals or epitaxial films, which is very promising not only for a direct spectroscopic observation of the ferroelectric phase but also for applications. With this motivation, in this work we carried out a systematic optical conductivity and Raman spectroscopy study in LMO single crystals across the AFM ordering temperature of the B -sites at $T_{N,B}=78$ K. The results confirm the centrosymmetric $I2/m$ structure of LMO, since no coincidence of the Raman and infrared (IR) modes is found. All IR modes are found to display the conventional mode renormalization expected in ordinary AFM, as said before. Conversely, the main Raman modes give evidence of a deviation from

the normal Balkanski behavior around 150 K and strong magnetoelastic coupling that manifests itself as a critical behavior at $T_{N,B}$. We propose to explain the results using the phenomenological theory of improper ferroelectrics developed by Levanyuk and Sannikov in [13] and hypothesize the existence of strong magnetic fluctuations above $T_{N,B}$, which turn out to affect the Raman modes but not the infrared ones because of symmetry considerations. This theory explains the formation of several ferroelectric domains with opposite orientations which accounts for the observed long-range centrosymmetric structure of LMO in the low-temperature phase, in the absence of a poling field. A complementary specific heat study on a LMO polycrystalline sample displays a very large magnetic field-induced suppression of the phonon contribution at low temperature, which supports a picture of strong magnetoelastic coupling. A straightforward analysis of the field-dependence of this suppression indicates that the dominant magnetoelectric term in the free energy is quadratic in the field. This result confirms the centrosymmetric structure of LMO and sets a constraint as to the microscopic mechanism of magnetic ferroelectricity relevant to the present case.

II. EXPERIMENTAL

Samples. As reported previously [46], $(\text{LaMn}_3)\text{Mn}_4\text{O}_{12}$ is a metastable phase synthesized at high pressure. Depending on the synthesis conditions, both powders or small 0.2-0.5 mm-sized single crystals are reproducibly obtained. The present spectroscopic study was carried out on single crystals, while a polycrystalline sample was used for the specific heat study. x-ray single-crystal diffraction was performed to identify the orientation of the single crystals. Neutron powder diffraction data taken at the 3T diffractometer of the LLB laboratory in Saclay confirm the purity of powder to be above 95%.

Raman spectroscopy. A series of Raman spectra in the 150-750 cm^{-1} range was taken as a function of temperature in the 10-300 K range by using a Jobin-Yvon/Horiba T64000 spectrometer equipped with a CCD camera. The spectra were taken by focusing an Ar laser beam ($\lambda = 514.5 \text{ nm}$) on a $\sim 5 \mu\text{m}$ diameter spot on the surface of a freshly broken $(\text{LaMn}_3)\text{Mn}_4\text{O}_{12}$ single-crystals. To ensure a good thermalization, we used silver paste to mount the sample on the cold head of a liquid-helium flow cryostat kept under a high vacuum of 10^{-6} mbar. By monitoring the mode frequency as a function

of the beam power measured before the optical window of the cryostat, we verified that sample heating is prevented using powers up to 8 mW, so we decided to use a 5 mW beam. For the strongest Raman modes, we achieved a typical energy resolution of 0.2 cm^{-1} .

Infrared spectroscopy. IR spectra were collected as a function of temperature upon warming-up the sample in a Bruker IFS66/s Fourier-Transform spectrometer. We used either a bolometer-Mylar Germanium or a 4.2 K Si:BPhototconductor-KBr:Ge detector-beamsplitter combination for the $80\text{-}700 \text{ cm}^{-1}$ and $300\text{-}2500 \text{ cm}^{-1}$ spectral regions, respectively. The measurements were performed in the reflectivity geometry using a Globar SiC source with a resolution of 2 cm^{-1} . Spectra were taken on a 0.5 mm -size single crystal polished using a Leica mechanical polisher equipped with a $0.1 \mu\text{m}$ diamond grain-paper and mounted on the cold finger of an Advanced Research Systems, Inc. Helitran cryostat. The polished surface does not correspond to a simple crystallographic direction as the normal direction of the surface is $[-2,4,-3]$. In order to investigate all modes, we used linearly polarized light with polarization along two orthogonal directions, indicated as P01 and P02. In order to determine the absolute reflectivity, we used an *in situ* gold overfilling technique, as described elsewhere [88].

Thermodynamic measurements. Temperature- and field-dependent magnetization, M , and specific heat, C_p , measurements were carried out on a $(\text{LaMn}_3)\text{Mn}_4\text{O}_{12}$ pellet using a Vibrating Sample Magnetometer (VSM) and a 2τ relaxation method, respectively, implemented in a commercial Quantum Design TM physical properties measurement system (PPMS) equipped with a 9 T superconducting magnet.

III. RESULTS

Fig. 4.1 summarizes the raw reflectivity data taken at 10 K in the $80\text{-}750 \text{ cm}^{-1}$ range for the two orthogonal polarizations, P01 and P02. Note that the two spectra share several modes, consistent with the fact that, according to the above x-ray diffraction analysis, the sample surface is oriented along the $[-2,4,-3]$ direction, which is not a principal direction. Our data analysis enabled us to identify 28 and 34 modes in the P01 and P02 polarizations, respectively. 23 modes are common to both polarizations, although with different intensities, hence we observe 39 IR modes in total. This observation

is consistent with a straightforward symmetry analysis of the IR- and Raman-active modes predicted in the monoclinic $I2/m$ symmetry of LMO. The 60 phonon modes have the following symmetries: $10 A_g + 18 A_u + 8 B_g + 24 B_u$ of which 39 ($17 A_u + 22 B_u$) are IR-active, 18 ($10 A_g + 8 B_g$) are Raman-active and the remaining 3 ($A_u + 2B_u$) are acoustic. Interestingly, the Raman-active modes involve only the oxygen atoms. Specifically, $2A_g + B_g$ modes correspond to the $4i$ Wyckoff sites, while the remaining $3A_g+3B_g$ modes concern the $8j$ sites. For both polarisations, the number of modes is unchanged with increasing temperature, although their intensities decrease, as expected. This confirms the conclusion of a previous structural study [46] that no structural change occurs in the whole temperature range investigated.

In order to analyze the IR spectra, we used a Lorentz oscillator for each mode, which yields the following contribution to the dielectric function:

$$\epsilon(\omega) = \epsilon_\infty + \sum_k \Delta\epsilon_k \frac{\Omega_k^2}{\Omega_k^2 - \omega^2 - i\gamma_k\omega} \quad (4.1)$$

where ϵ_∞ is the contribution of the electronic transitions and each transverse-optical (TO) k -th mode is described by a resonance frequency Ω_k , an dielectric strength $\Delta\epsilon_k$ and a damping γ_k . As usual, these parameters were fitted under the constraint that the reflectivity calculated at normal incidence, $R = |1 - \sqrt{\epsilon}|^2 / |1 + \sqrt{\epsilon}|^2$, matches the experimental value. Note from Fig. 4.1 the excellent agreement between the experimental reflectivity curve and the fit. Using Eq. 4.1, we obtained the imaginary part of the dielectric function, ϵ'' , whose maxima represent the TO-frequencies. This function is plotted in Fig. 4.2 for both P01 and P02 polarizations and compared with the Raman spectrum taken at the same temperature (≈ 10 K). The Raman spectrum displays 11 modes, which is consistent with the previous prediction of 18 Raman-active modes, considering that some modes, for instance those at 475 and 660 cm^{-1} , may be split in frequency, however the splitting is not clearly resolved because of the cubic pseudosymmetry of LMO. Specifically, the a - and c -axis parameters are very similar. Most IR modes are not present in the Raman spectra, and vice-versa, which confirms the previous conclusion from a neutron diffraction study [46] that the space group of LMO remains centrosymmetric $I2/m$ down to low temperatures. In order to confirm this result, we attempted to carry out *ab initio* calculations of the phonon frequencies

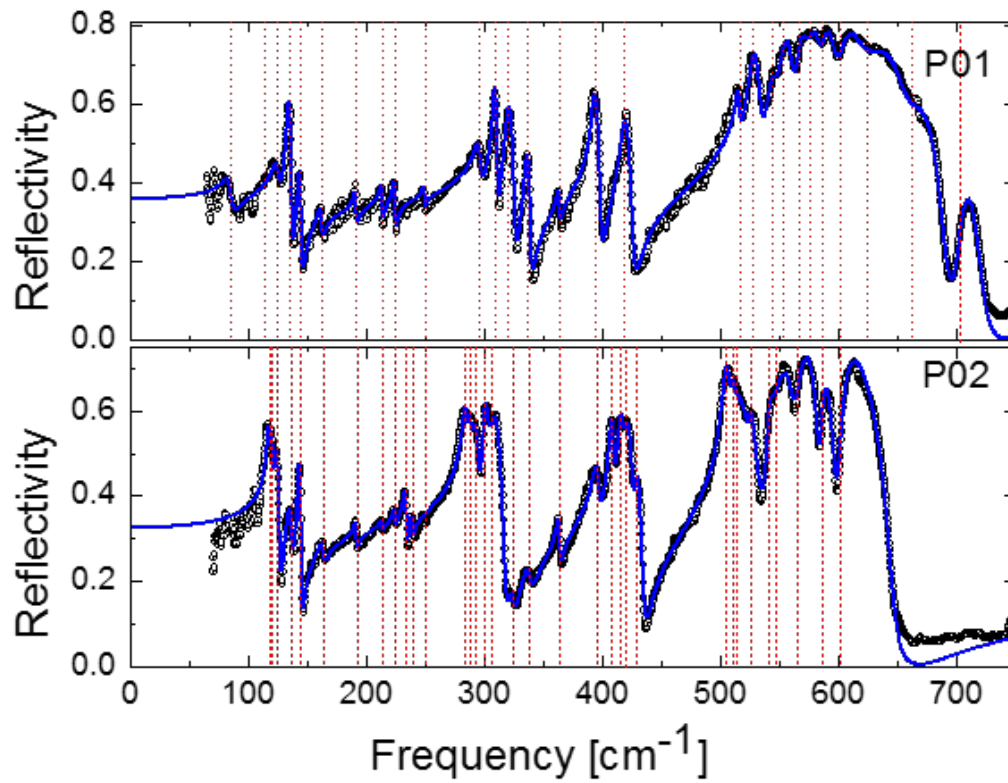


Figure 4.1: Reflectivity of a LMO single crystal measured at 10 K using polarized light with two orthogonal polarizations P01 (top panel) and P02 (bottom panel). Black dots are experimental points; blue lines are fits to the data using transverse-optical (TO) Lorentz oscillators, according to Eq. 4.1. The dashed vertical red lines represent the positions of the fitted TO modes.

in a relaxed $I2/m$ structure within density functional theory (DFT) in the local density approximation. The calculations led to six negative frequency values, which may reflect the limitations of DFT to precisely describe the electronic and dynamical properties of this system.

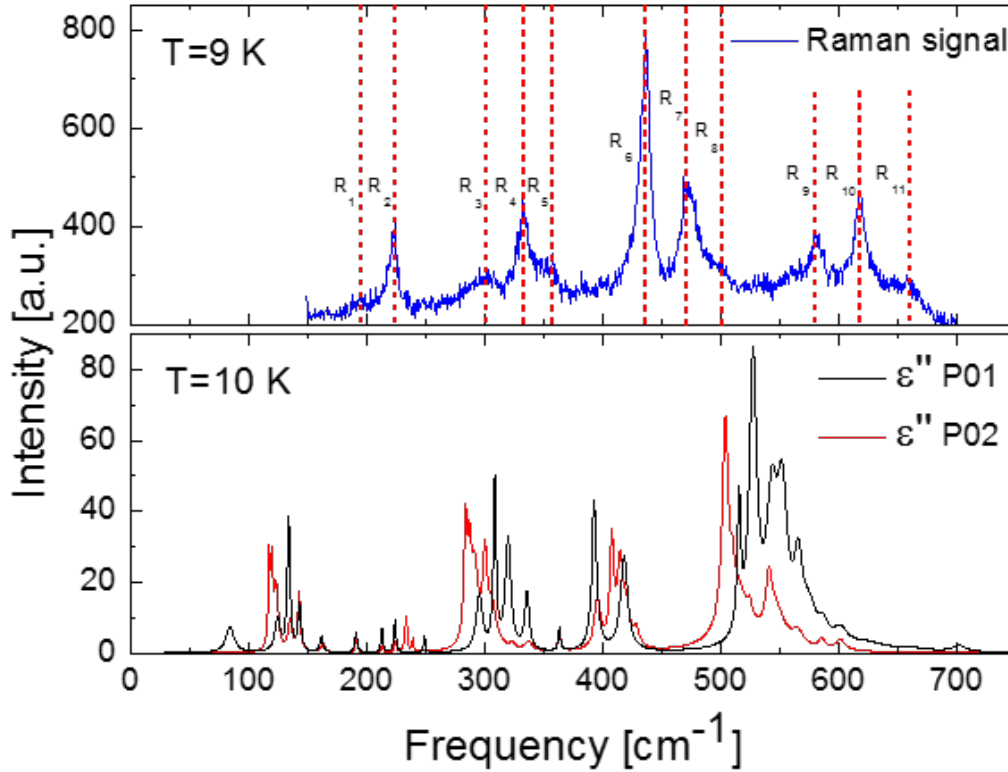


Figure 4.2: Top: Raman spectrum of a representative $(\text{LaMn}_3)\text{Mn}_4\text{O}_{12}$ single crystal measured at 10 K. Bottom: imaginary part of the dielectric function of a $(\text{LaMn}_3)\text{Mn}_4\text{O}_{12}$ single crystal from the same batch obtained from the fit with Lorentz's model of the IR reflectivity curves taken at 10 K for two P01 (red) and P02 (black) orthogonal light polarizations.

In the absence of phonon calculations, we tentatively assign the main Raman modes observed experimentally by comparing them with those previously reported on perovskitelike compounds with similar electronic and structural characteristics. We refer to two studies by Iliev *et al.* on LaMnO_3 [89] and on $(\text{CaMn}_3)\text{Mn}_4\text{O}_{12}$ [90] which exhibit an orthorhombic $Pmna$ and rhombohedral $R\bar{3}$ distortion, respectively, of the pristine

cubic $Pm-3m$ structure of simple perovskites. Similar to LMO, in both compounds, only the oxygen atoms are Raman active. The analysis of the descent in symmetry of the irreducible representations (IRs) indicates that: i) A_g modes of the $R-3$ space group are A_g modes in $I2/m$ as well; ii) E_g modes of $R-3$ correspond to B_g modes in $I2/m$; iii) E_g modes arising from a $A_g + E_g$ decomposition in $R-3$ correspond to A_g modes of $I2/m$. This correspondence leads us to conclude that the R_9 , R_{10} and R_{11} modes observed in LMO correspond to a T_g mode of the pristine cubic $Im-3$ phase. The frequency of the R_{11} mode at 660 cm^{-1} is close to that of the Jahn-Teller (JT) B_g mode of LaMnO_3 observed at 693 cm^{-1} [89]. Similarly, the frequency of the R_{10} mode at 620 cm^{-1} is close to that of the A_g mode of $(\text{CaMn}_3)\text{Mn}_4\text{O}_{12}$ at 612 cm^{-1} . Hence, according to the above correspondence of modes, the R_{10} mode of LMO is an A_g mode. In $(\text{CaMn}_3)\text{Mn}_4\text{O}_{12}$, this later mode has been reported to be one of the two peaks of a doublet arising from a splitting of a T_g mode of the pristine cubic phase, consistent with the hypothesis that R_9 , R_{10} and R_{11} form a T_g triplet in LMO arising from the undistorted cubic phase. Thus, R_9 is likely to be the B_g mode of the triplet split by the monoclinic $I2/m$ distortion. The R_7 , R_6 and R_2 modes at 475 , 438 and 223 cm^{-1} , respectively, are close to the 3 A_g modes at 474 , 428 and 211 cm^{-1} of $(\text{CaMn}_3)\text{Mn}_4\text{O}_{12}$. Thus, the symmetry of these modes should be A_g in LMO as well. We give a physical interpretation of the above Raman modes by noting that the polarization of these modes should not be fundamentally different from that of the modes previously studied in orthorhombic LaMnO_3 . Following Iliev *et al.* [89, 90], the high-, intermediate- and low-frequency regions $582\text{-}693$, $462\text{-}509$ and $218\text{-}347\text{ cm}^{-1}$ correspond to the stretching, bending and rotation modes of the MnO_6 octahedra, respectively.

In the following, we should analyze the temperature dependence of the main IR and Raman modes by focusing on the anomalous behavior expected in the vicinity of the AFM ordering transition temperature, $T_{N,B} = 78\text{ K}$. We limit ourselves to study the changes of mode frequency as determined by fitting the experimental peaks using Lorentz and Fano-Lorentz functions for the IR and Raman modes, respectively. Following previous work the latter function was chosen to take into account the asymmetry of the Raman modes. In Fig. 4.3, the temperature dependence of the frequency is plotted for six representative IR modes. Modes labeled as IR-12 and IR-26 exhibit a

conventional behavior consisting in a progressive hardening with decreasing temperature which levels off at low temperature. This characteristic behavior, caused by mode anharmonicity, is explained by Balkanski's model [91]. The other four modes IR-11, IR-21, IR-31 and IR-36 follow the above conventional behavior until the AFM ordering temperature $T_{N,B}$ at which an anomalous softening or hardening occurs. This anomaly is a consequence of AFM transition [82, 83], previously observed in several compounds including manganese oxides with perovskitelike structure similar to the present compound LMO [79, 85, 89, 92, 80, 93]. In agreement with previous studies [85, 83] we have found that the frequency change $\Delta\omega$ caused by the magnetic order below $T_{N,B}$ in LMO is well explained by Baltensperger and Helman (BH) theoretical expression [84] obtained by including the spin energy to the Hamiltonian of an harmonic lattice. In second-order perturbation theory, it turns out that $\Delta\omega$ is proportional to the spin-spin correlation function and that the proportionality coefficient is an appropriate average of the exchange couplings between all neighboring magnetic ions. Hence, the BH theory predicts that the sign of the frequency change in the magnetic phase reflects the sign of the dominant exchange terms. According to this prediction, the experimental results of Fig. 4.3 indicate that the magnetic structure of the B -sites of LMO is described by exchange terms with opposite sign, in agreement with the previous report of C-type structure [46], formed by ac -planes of AFM-coupled ions coupled ferromagnetically along the b -axis. In agreement with the above BH prediction, Fig. 4.3 further shows that, for all modes, the anomalous frequency change $\Delta\omega$ below $T_{N,B}$ is well described by the square of the ZFC susceptibility (see Fig.4.3). In conclusion, in LMO, the anomalies of the IR modes observed at the magnetic transition are fully explained by the effect of spin energy on mode frequency, as treated in the above BH theory, without invoking the effect of electric polarization.

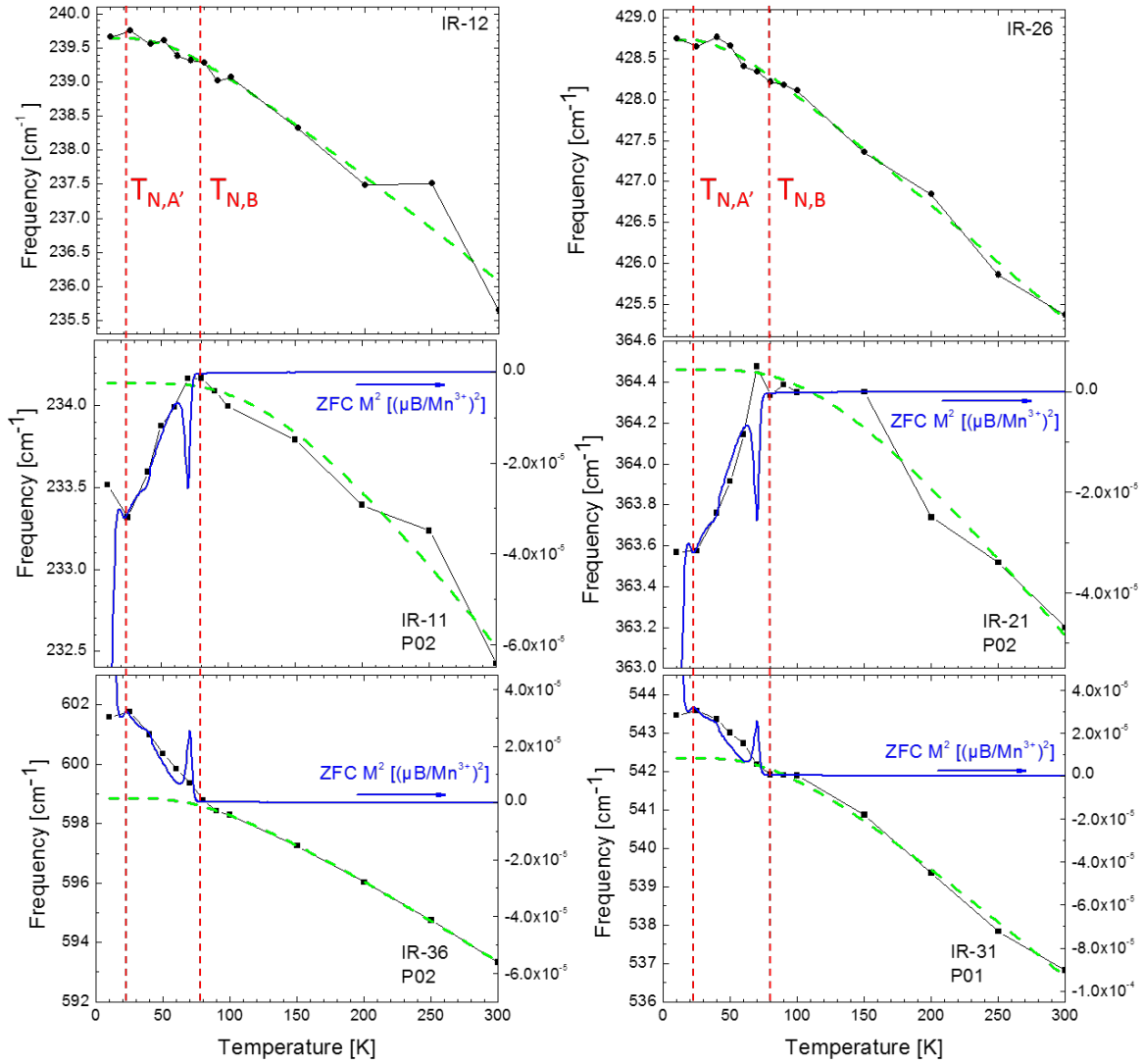


Figure 4.3: Black dots: Temperature dependence of the frequency of representative IR modes in the 10-300 K range. The magnetic phase transitions at $T_{N,B}$ and $T_{N,A'}$ are indicated by red dashed lines. The green dashed lines show the Balkanski's anharmonic phonon hardening obtained from fitting of the high temperature range. The blue solid lines represent the square of the ZFC magnetization measured on a single-crystal of $(\text{LaMn}_3)\text{Mn}_4\text{O}_{12}$.

Interestingly, much more pronounced anomalies near $T_{N,B}$ are found in the behavior of the Raman modes. Fig. 4.4 shows the temperature dependence of the frequency of the three strongest modes in the 10-300 K range. Well above $T_{N,B}$, in the 150-300 K range, all these modes follow the conventional dependence predicted by the aforementioned Balkanski model. However, upon approaching $T_{N,B}$, below 150 K, all modes display a strong hardening, followed by a marked drop of 2-3 cm^{-1} at $T_{N,B}$. At the temperature corresponding to the magnetic orientation of A' -sites, $T_{N,A'}$, there is a second renormalisation of the Raman-modes characterized by a slow softening. To the best of our knowledge, such marked anomalies, characterized by a large frequency drop at the magnetic ordering transition ($T_{N,B}$), were never reported before either in conventional AFM or in magnetic ferroelectrics. For example, the anomalies observed in related manganese oxides such as $(\text{CaMn}_3)\text{Mn}_4\text{O}_{12}$ [93] or RMnO_3 [79, 85, 89, 92, 80, 93] consist in discontinuities of the slope of the temperature-dependent frequency curves similar to the one occurring at $T_{N,A'}$ in our case. The peak behavior observed here is similar to the critical behavior of thermodynamic quantities such as specific heat found at second-order phase transitions. This similarity suggests a critical behavior of the strain field, as the latter directly governs the Raman matrix elements.

In the following, we will try to interpretate the results in the framework of phenomenological theory of improper ferroelectrics developed by Levanyuk and Sannikov [13]. We recall that in improper ferroelectrics, the polarization (electric dipolar moment) is not the order parameter of the ferroelectric transition. In the particular case of magnetic ferroelectrics, the order parameter is the magnetization. The authors show that the generic order parameter entering in the Ginzburg-Landau thermodynamic potential of improper ferroelectrics is formed by at least two scalar components ξ and η , forming two second-order invariants $\xi\eta P$ and $(\xi^2 - \eta^2)P$. As a consequence, $\xi\eta$ and $(\xi^2 - \eta^2)$ are polar, while ξ and η are not. The above order parameter components have the meaning of normal coordinates of modes. It results that the matrix elements giving the contribution in IR and Raman spectrum of the polarization are $\langle f|\xi\eta P|i \rangle$ and $\langle f|\xi\eta\chi E|i \rangle$, respectively, where χ is the tensor of polarizability. In the high-temperature paraelectric phase ($T > T_c = T_{N,B}$), because of symmetry constraints, the IR term is equal to zero, that is, the polar soft mode associated to ferroelectric displace-

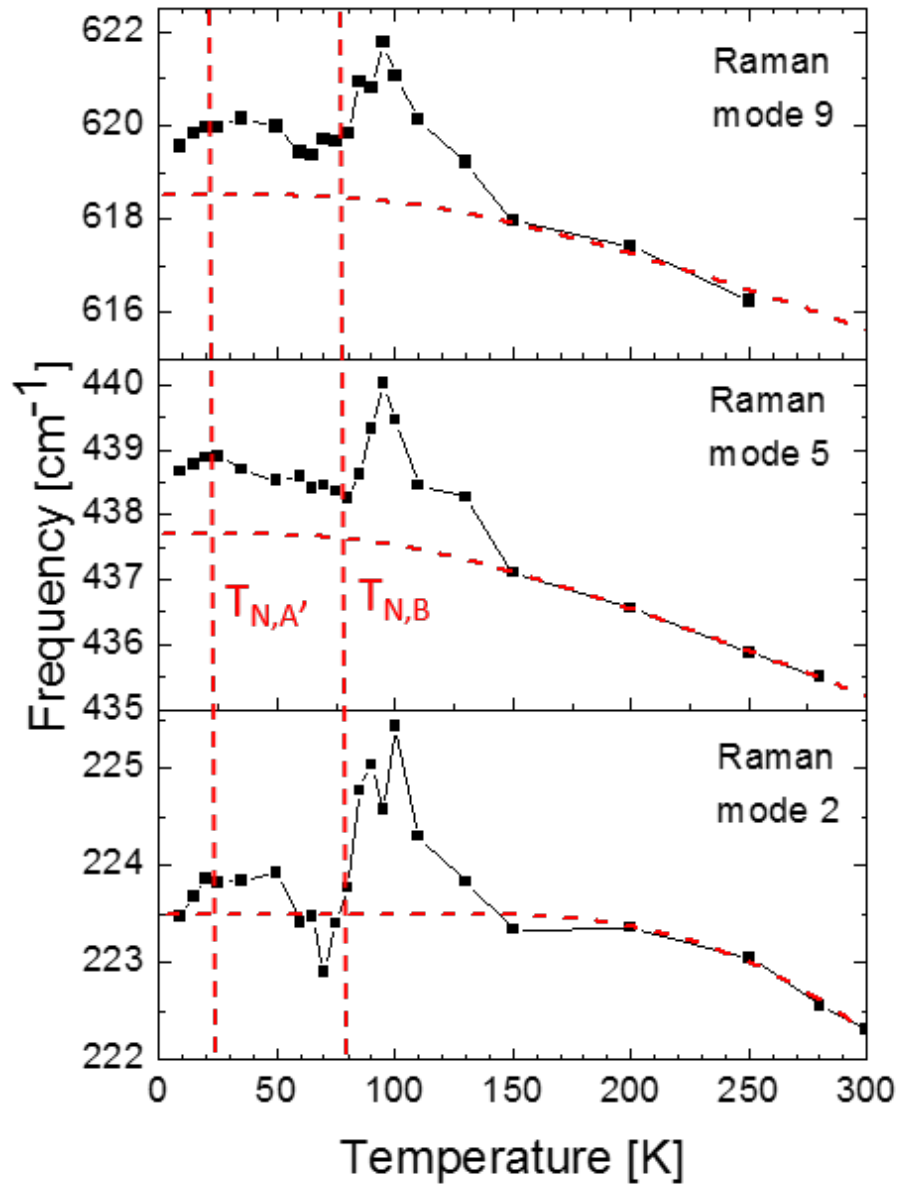


Figure 4.4: Thermal evolution of Raman frequency of the 3 principal modes obtained from asymmetric-Lorentz fit of the data between 250 and 10 K. The magnetic phase transitions T_B and $T_{N,A'}$ are indicated by the red dotted vertical lines.

ments is inactive in the IR spectrum. In the low-temperature ferroelectric phase, $|i\rangle$ is polar, therefore both terms are allowed by symmetry. However, the IR term varies continuously in P giving a very low contribution in intensity near the transition point and might be difficult to detect in IR spectrum. Both theoretical results are coherent the absence of anomaly driven by ferroelectricity in our reported IR spectra. On the other hand the Raman term is allowed by symmetry in the paraelectric phase but its contribution zero because by definition $\langle \xi \rangle = \langle \eta \rangle = 0$ in the symmetric phase. However, we envisage that strong fluctuations of the ξ and η can give a contribution to the raman-active modes. Finally, when going through the transition, the Raman term undergoes a critical behavior due to the improper ferroelectric transition driven by ξ and η which present simultaneously spontaneous non-zero mean values at T_c . The link between the thermodynamic potential, the thermal expansion coefficient and the relation between the relative variation of frequency of mode and the relative variation of volume given by the Gruneisen parameter help us to conclude that a jump of specific heat due to the second-order improper ferroelectric transition is equivalent to a jump in frequency of the corresponding modes. Therefore, we can explain the deviation of Raman frequencies from the normal thermal Balkanski behavior at 150 K by the effect of strong magnetic fluctuations and the drop at $T_{N,B}$ by the coupling of Raman modes with ferroelectric displacements.

The frequency dependence of the low frequency dielectric constant can be tracked from the fitting parameters of IR spectra. In Fig. 4.5, we report the frequency dependence of the low-frequency optical value (from P01 spectra) of the dielectric constant (ϵ' real part of the dielectric function) at several temperatures with the very-low frequency value, ϵ_0 , obtained from capacitance measurements. The figure shows a significant discrepancy between the two values as, the IR data consistently yield $\epsilon_0=15-16$, while the dc value measured directly by means of the capacitance method is significantly higher, ~ 25 . As previously discussed in TbMnO_3 [81], this discrepancy can be explained by electromagnons in the ferroelectric phase, which should be detected in the low frequency $10-80 \text{ cm}^{-1}$ region of the Raman spectra, not accessible to the present experiment. However in this case, the contribution of the electromagnons should disappear at $T_{N,B}$ which is not the case. We should rather attribute the difference of the

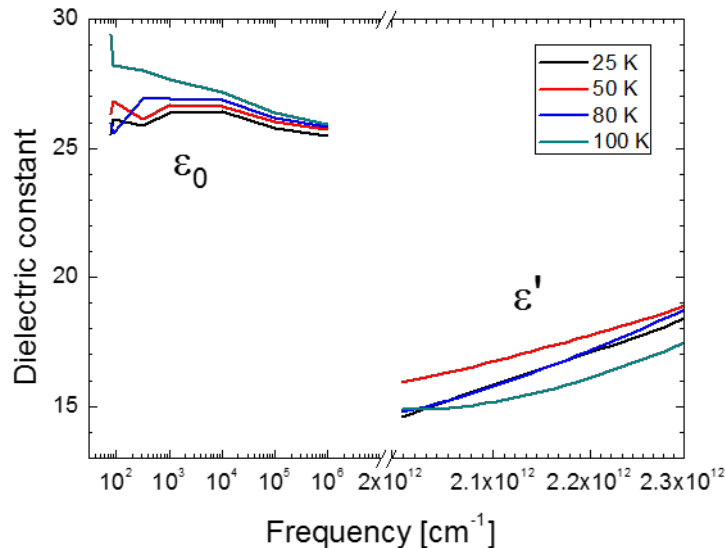


Figure 4.5: Comparison of the low-frequency dielectric constant of $(\text{LaMn}_3)\text{Mn}_4\text{O}_{12}$ calculated from the Lorentz fit of IR spectra (P01) as a function of frequency and the very-low DC value, ϵ_0 , obtained from capacitance measurements on polycrystalline sample.

infrared and DC values to relaxor-like phenomena, since ϵ_0 curves undergo a negative slope as a function of frequency.

The above scenario of magnetoelastic coupling is confirmed by a systematic study of the specific heat, $C_p(T, H)$, measured as a function of magnetic field, H , and temperature, T , at constant pressure in the AFM phase, $T < T_{N,B}$. Since the electronic contribution to the specific heat is vanishing in insulating LMO, our expectation is that the field-induced changes of C_p directly reflects the changes in lattice dynamics. According to this expectation, we found the very large field-induced changes shown in Fig. 4.6 where it is noted that, at all temperatures below $T_{N,B}$, C_p is reduced by the field; at the maximum applied field of 9 T, the relative reduction $C_p(H)/C_p(0)$ reaches 40 % at 2 K and progressively decreases with increasing temperature. This finding provides further evidence of a large magnetoelastic coupling and indicates that the magnetic field induces a lattice hardening, consistent with the previous Raman data.

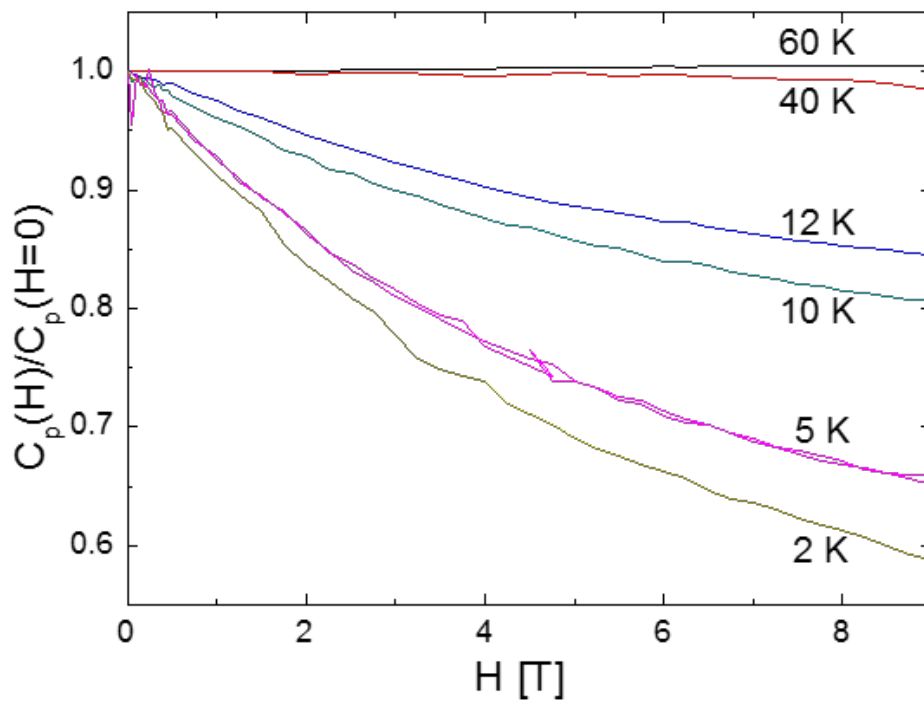


Figure 4.6: Temperature-dependent heat capacity of polycrystalline $(\text{LaMn}_3)\text{Mn}_4\text{O}_{12}$ as a function of applied magnetic field H in the 2-60 K range.

IV. CONCLUSIONS

In conclusion, the present systematic infrared (IR) optical conductivity and Raman spectroscopy study unveils an opposite behavior of the IR and Raman modes at the AFM ordering transition in the magnetic ferroelectric LMO. First, the absence of simultaneously IR- and Raman-active modes confirms the picture of centrosymmetric structure a priori not compatible with a long-range lattice induced electric polarization. Second, the absence of pronounced anomalies in the IR modes is consistent with previous theories on the symmetry invariants characterizing the onset of ferroelectricity in improper ferroelectrics. On the other hand, the pronounced mode hardening followed by an abrupt frequency drop found in the Raman modes point to a strong magnetoelastic coupling at $T_{N,B}$ consistent with the onset of fluctuating ferroelectric domains that could explain the average non polar structure. The large depression of the lattice specific heat in large fields gives further evidence of an additional field-induced lattice hardening induced by the magnetic order at $T_{N,B}$.

Chapter 5

Effect of the chemical pressure ($\text{La}^{3+}/\text{Y}^{3+}$ substitution)

5.1 Introduction

En parallèle de l'étude de la phase déjà existante LMO, nous avons cherché à obtenir une nouvelle phase de perovskite quadruple dans le but d'améliorer les propriétés multiferroïques. La particularité de la structure pérovskite quadruple par rapport à la pérovskite simple réside dans l'inclinaison particulièrement prononcée des octaèdres d'oxygène, à l'origine de l'angle de super-échange $Mn-O-Mn$, $\psi \sim 137^\circ$. Cette propriété structurale est responsable de la compétition entre les interactions d'échange antiferromagnétique et ferromagnétique en fonction de la direction et selon les deux trajectoires $B-O-B$ et $A'-O-B$ disponibles entre ions magnétiques premiers voisins. Notre idée a donc été d'introduire sur le site A un atome de petite taille afin d'augmenter l'interaction d'échange, mais sans changer la valence du site A afin de garder la monovalence $3+$ de tous les manganèses dans la structure. Nous avons donc choisi l'atome d'Yttrium qui est $\sim 30\%$ plus petit que le Lanthane et qui, comme ce dernier, possède le même état d'oxydation $3+$. Comme attendu, pour stabiliser une telle phase, où la pression chimique est plus importante dû à la petite taille de l'ion Y^{3+} , il faut augmenter la pression de synthèse. Nous avons donc commencé l'étude du diagramme de phase au dessus de 6.5 GPa. A l'aide de plusieurs synthèses nous avons pu déterminer la zone de stabilité de la phase et obtenir des échantillons de poudre de grande pureté (98%).

5.2 Article III: Effect of chemical pressure induced by the $\text{La}^{3+}/\text{Y}^{3+}$ substitution on the magnetic ordering of $(\text{AMn}_3)\text{Mn}_4\text{O}_{12}$ quadruple perovskites

STATUS: To be published in Physical Review Materials in December 2017.

Effect of chemical pressure induced by the $\text{La}^{3+}/\text{Y}^{3+}$ substitution on the magnetic ordering of $(\text{AMn}_3)\text{Mn}_4\text{O}_{12}$ quadruple perovskites

M. Verseils,¹ F. Mezzadri,² D. Delmonte,² B. Baptiste,¹ Y. Klein,¹ S. Shcheka,³ L.C. Chapon,^{4,*} T. Hansen,⁴ E. Gilioli,² and A. Gauzzi¹

¹ *Institut de Minéralogie, de Physique des Matériaux et de Cosmochimie - Sorbonne Université, UPMC, CNRS, IRD, MNHN - 4, place Jussieu, 75005 Paris, France*

² *Istituto dei Materiali per Elettronica e Magnetismo, CNR, Area delle Scienze, 43100 Parma, Italy*

³ *Bayerisches Geoinstitut, University of Bayreuth, 95440 Bayreuth, Germany*

⁴ *Institut Laue-Langevin, 71 avenue des Martyrs, 38000 Grenoble, France*

Abstract

We report on the successful high-pressure synthesis of single-phase powders of the quadruple perovskite $(\text{YMn}_3)\text{Mn}_4\text{O}_{12}$, where the chemical pressure exerted by the small Y^{3+} ion is expected to enhance the exchange interaction between Mn^{3+} ions. According to this expectation, powder neutron diffraction, specific heat and magnetization measurements give evidence of a C-type antiferromagnetic ordering of the Mn^{3+} ions in the octahedrally coordinated B -sites at $T_{N,B}=108$ K, 30 K higher than in the isostructural and isovalent compound, $(\text{LaMn}_3)\text{Mn}_4\text{O}_{12}$. Surprisingly, we found no evidence of long-range magnetic order of the square-coordinated A' -sites, although an indication of latent magnetic order is given by a broad peak of the DC magnetization between 70 and 40 K and by a sharp peak in the AC susceptibility at $T^*=70$ K. A further unexpected feature of $(\text{YMn}_3)\text{Mn}_4\text{O}_{12}$, not found in previously reported $(\text{AMn}_3)\text{Mn}_4\text{O}_{12}$ compounds, is a

second-order structural phase transition at $T_s=200$ K, attributed to a partial redistribution of charge involving both the B and A' -site Mn^{3+} ions. The present results suggest the existence of competing magnetic orderings, which may be linked to the occurrence of magnetic ferroelectricity in the $(\text{AMn}_3)\text{Mn}_4\text{O}_{12}$ system.

I. INTRODUCTION

Quadruple perovskites, described by the general formula $(\text{AA}'_3)\text{B}_4\text{O}_{12}$, have recently attracted a great deal of interest for they display unique charge, spin and orbital orderings not found in simple perovskites, ABO_3 . These properties arise from a unique pseudocubic structure shown in Fig. 1, first reported by Marezio *et al.* [42], which hosts two distinct A and A' sites. The structure is stabilized by the Jahn-Teller distortion of the latter sites, typically occupied by Cu^{2+} , as in the prototype compound $\text{CaCu}_3\text{Ti}_4\text{O}_{12}$ reported by Deschanvres *et al.* [43], or by Mn^{3+} , as in the present case. The distortion turns the pristine dodecahedral coordination of the A' sites into square-planar and drives a very large tilt of the corner-sharing BO_6 octahedra, the tilt angle $\psi \sim 137^\circ$ being much larger than that found in simple perovskites. The resulting structure is characterized by two distinct B -O- B and A' -O- B zig-zag superexchange paths with competing antiferromagnetic (AFM) or ferromagnetic (FM) interactions, which accounts for the variety of ground states observed. The square coordination of the A' sites also accounts for the absence of oxygen defects in quadruple perovskites, as these defects would destabilize the bond structure. This feature constitutes a further important difference as compared to simple perovskites where oxygen nonstoichiometry greatly affects the physical properties. In the present paper, we consider the quadruple perovskite $(\text{AMn}_3)\text{Mn}_4\text{O}_{12}$ family where both A' and B sites are occupied by Mn. Among the remarkable properties observed in these compounds, notable are the full charge order in the mixed-valence compound $(\text{NaMn}_3)\text{Mn}_4\text{O}_{12}$ [47] and the large values of electric polarization induced by magnetism in $(\text{CaMn}_3)\text{Mn}_4\text{O}_{12}$ [40], attributed to a peculiar helicoidal orbital and magnetic order [41, 49].

The above orderings remain poorly understood because of a complex interplay between charge, spin and orbital degrees of freedom, which makes the development of realistic theoretical models challenging. In the absence of reliable models, in the present

work we investigate the effect of chemical pressure on the stability of the magnetic structure, as the exchange interaction is sensitive to bond angles and bond distances of the superexchange paths. We consider the comparatively simple case of single valent Mn^{3+} systems where only the spin and orbital degrees of freedom come into play. Specifically, we report on the successful high pressure synthesis of high-purity $(\text{YMn}_3)\text{Mn}_4\text{O}_{12}$ powders, where the Y^{3+} ion ($R_{\text{Y}^{3+}} = 1.1 \text{ \AA}$ [94]) is significantly smaller than all the A -ions (La^{3+} , Bi^{3+} , Ca^{2+} , Na^+ , Pr^{3+} , Pb^{2+}) previously reported for the $(\text{AMn}_3)\text{Mn}_4\text{O}_{12}$ system [44, 65, 95]. According to our expectation, we achieved a significant increase of the ordering temperature of the B -sites as compared to its isovalent counterpart with $A=\text{La}$ [46]. On the other hand, we surprisingly find no long-range magnetic order of the A' -sites, which has always been observed in all $(\text{AMn}_3)\text{Mn}_4\text{O}_{12}$ compounds previously reported. Instead, at high temperature, we observe a second-order structural phase transition never observed in any of these compounds. These unexpected features suggest the existence of latent structural and magnetic instabilities in the $(\text{AMn}_3)\text{Mn}_4\text{O}_{12}$ system.

The paper is organized as follows: in Section II, we report on the experimental techniques employed for the synthesis and characterization of both single crystals and powder samples of $(\text{YMn}_3)\text{Mn}_4\text{O}_{12}$. In Section III, we present and discuss the properties of the nuclear and magnetic structure and the result of the magnetic, and thermodynamic measurements. In particular, we discuss the results with emphasis on the unexpected absence of long-range order in the A' -sites. In Sec. IV, we draw the conclusions.

II. EXPERIMENTAL

High-pressure synthesis. $(\text{YMn}_3)\text{Mn}_4\text{O}_{12}$ single crystals and powder samples were obtained from the solid state reaction of stoichiometric mixtures of Y_2O_3 and Mn_2O_3 powders filling a Pt capsule at 9 GPa and 1300°C for 2 hours using a multi-anvil press, as described in detail elsewhere [53]. A 1000 tons multi-anvil press installed in the IMEM-CNR laboratory was used to optimize the synthesis conditions. A larger 6000 tons press installed at the Bayerisches Geoinstitut in Bayreuth was used to prepare a larger ($\sim 1\text{g}$) amount of powders required for the powder neutron diffraction study. After the heat treatment, the samples were quenched to room temperature and the

pressure was slowly released. Attempts to obtain the desired phase at lower pressure or at lower temperatures were not successful. A room temperature powder x-ray diffraction (xrd) analysis in the Bragg-Brentano geometry by means of a laboratory diffractometer equipped with a $\text{Cu K}\alpha$ source was performed to check the purity of the as-prepared powders after each run.

Single-crystal x-ray diffraction. Single-crystal X-ray diffraction data were collected on an Oxford diffraction Xcalibur-S diffractometer equipped with a Sapphire CCD-detector with $\text{Mo-K}\alpha$ radiation ($\lambda = 0.71073 \text{ \AA}$, graphite monochromator) at 293 K. Data reduction, cell refinement, space-group determination, scaling and multiscan absorption correction [96] were performed using *CrysaAlisPro* software [97]. The structure was solved through Olex2 program [98] by direct methods using *SHELXT* [99]. The refinement was then carried out with *SHELXL-2013* [99] by full-matrix least squares minimization and difference Fourier methods. All atoms were refined with anisotropic displacement parameters.

Neutrons powder diffraction In order to systematically study the nuclear and magnetic structures as a function of temperature, a neutron powder diffraction experiment was subsequently performed on a 920 mg powder sample at the high-intensity two-axis D20 diffractometer of the Institut Laue Langevin in Grenoble (France) using $\lambda_1 = 1.54 \text{ \AA}$ and 2.41 \AA wavelengths and a 90° takeoff set-up. The data were taken as a function of temperature by warming-up the sample from 4 K up to room temperature at a rate of 0.25 K /min. The two wavelengths are optimized for an accurate determination of the nuclear and magnetic structures, respectively. We employed the Fullprof package [55] in the sequential and multi-pattern mode to perform, for each temperature, a Rietveld refinement of the nuclear and magnetic structures using the two λ_1 - and λ_2 -patterns with the same weight. Thermal displacement parameters were refined with anisotropic model for A'-sites because of their anisotropic environment and with isotropic model for all the other atoms.

Thermodynamic and magnetic properties. Constant-pressure specific heat (C_p) measurements as a function of temperature in the 2-400 K range were carried out on the same powders as above using a 2τ -relaxation method in a commercial Quantum DesignTM Physical Property Measurement System (PPMS). DC magnetization (M_{DC})

measurements were carried out in a commercial Quantum DesignTM Superconducting Quantum Interference Device magnetometer (SQUID) as a function of temperature and field. A first zero-field-cooling (0-ZFC) measurement was performed after having completely removed the residual field by warming the superconducting magnet above its critical temperature. A further series of ZFC and field-cooling (FC) magnetization curves in the 10-100 Oe range were taken by minimizing the residual field before each ZFC measurement. This was accomplished by discharging the magnet in the oscillating mode. We verified that this procedure typically reduces the residual field below 0.02 Oe, as measured by means of a gaussmeter.

III. RESULTS

A. Structural properties

Crystal structure. The single-crystal X-ray diffraction study indicates that, at room temperature, the system crystallizes in the monoclinic $I2/m$ space-group, see Supplemental Material (section 5.3) for tables refinement. This indicates that the isovalent La/Y substitution does not alter significantly the structure of the pristine (LaMn₃)Mn₄O₁₂ compound, as expected, which is confirmed by a subsequent powder neutron diffraction study (see Fig. 5.1). This study also shows that the purity of the powder sample is 95 % or better. The diffractogram shows minor diffraction peaks attributed to an unknown impurity phase formed at 9 GPa. In the following, we shall limit ourselves to analyze the neutron data as a function of temperature. In the whole 4 - 285 K range investigated, no indication of symmetry change was detected within the experimental resolution and all patterns were successfully refined in the $I2/m$ symmetry. In the refinement, all B thermal parameters were supposed to be isotropic except those of the Mn A' -sites for which the square-coordination is expected to be anisotropic. For all temperatures, we obtained good refinements, such as those shown in Fig. 5.1, where the experimental and calculated patterns are compared for two representative temperatures, 285 K and 4 K. The quality of the refinement did not change appreciably in the whole temperature range studied. However, we noticed an anomalous increase of the B parameter of Y below $T_s=200$ K. This indicates that the structural transition at T_s may be associated with a shift of Y ions from the centrosymmetric (0,0,0) posi-

5.2. Article III: Effect of chemical pressure induced by the $\text{La}^{3+}/\text{Y}^{3+}$ substitution on the magnetic ordering of $(\text{AMn}_3)\text{Mn}_4\text{O}_{12}$ quadruple perovskites

tion. The inherent limitation of the present refinement of powder diffraction data does not permit to unambiguously identify any symmetry change. A further high-resolution single-crystal study, e.g. by synchrotron x-ray diffraction, may elucidate this point.

In Table I, we report the results of the refinements of the 285, 190 and 4 K structures. As expected, the smaller Y^{3+} ion leads to a 2 % smaller unit cell, $V = 407.42(2) \text{ \AA}^3$, as compared to the isostructural compound $(\text{LaMn}_3)\text{Mn}_4\text{O}_{12}$. The room-temperature unit-cell parameters are $a = 7.4500(2) \text{ \AA}$, $b = 7.3418(2) \text{ \AA}$, $c = 7.4500(2) \text{ \AA}$ and $\beta = 91.121(1)^\circ$. The evolution of the structure with temperature is shown in Fig. 5.2. At high temperature, above T_S , the c -axis and the monoclinic angle β display an unusual increase upon decreasing T . Below T_S , the a -axis parameter also increases, hence the unit-cell volume suddenly increases. This feature gives evidence for a second-order phase transition at T_s with no apparent change of space group. The neutron diffraction patterns display neither extra Bragg peaks nor changes of intensity in any peak, which indicates that the transition at T_s is non magnetic. A similar V -shaped behavior of the unit-cell volume was recently reported in $(\text{CaMn}_3)\text{Mn}_4\text{O}_{12}$ [100] where the anomaly is concomitant to a cubic-to-rhombohedral structural transition. At lower temperature, *i.e.* below $T_{N,B}=108 \text{ K}$, V turns back into a conventional regime with positive thermal expansion. As discussed below, this temperature corresponds to the magnetic ordering of B-sites. In this temperature, no anomaly is observed in the behavior of the unit-cell parameters; all of them display a smooth temperature dependence and the cusp-like behavior of V at $T_{N,B}$ is less pronounced than that at T_s . This behavior is due to a levelling-off of the a -axis dependence and to a smaller expansion rate of the c -axis parameter, while b continues to decrease rapidly.

In order to gain an insight into the origin of the transitions at T_s and at $T_{N,B}$, we analyze the temperature dependence of the relevant Mn-O bond-length distances for the A' ($2b$, $2c$, $2d$) and B -sites ($4e$, $4f$), as shown in Figs. 5.4 and 5.3, respectively. Representative values of these distances and of the corresponding Jahn-Teller (JT) distortion parameters, Δ_{JT} , for the B -sites are reported in Table 6.1. The Δ_{JT} values for the two octahedra are slightly different and somehow larger than in $(\text{CaMn}_3)\text{Mn}_4\text{O}_{12}$ [101] but smaller than in $(\text{LaMn}_3)\text{Mn}_4\text{O}_{12}$ [46]. At both transition temperatures, T_s and $T_{N,B}$, almost all distances exhibit more or less pronounced discontinuities in the slope.

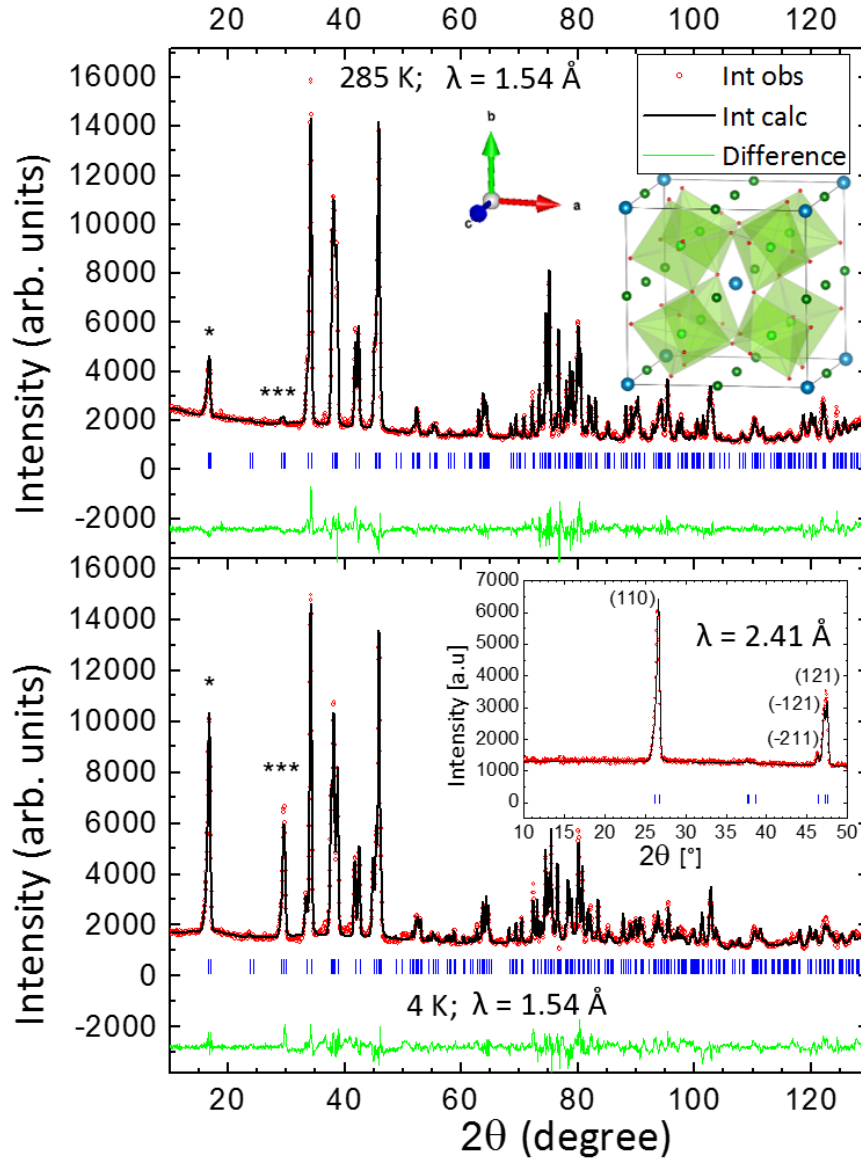


Figure 5.1: Red circles: Experimental neutron diffraction patterns taken at 285 K (top panel) and 4K (bottom panel) on the $(\text{YMn}_3)\text{Mn}_4\text{O}_{12}$ powder sample using a wavelength $\lambda_1 = 1.54 \text{ \AA}$. Black line: calculated intensity obtained by refining the λ_1 and λ_2 patterns, as described in the text. Green line: difference between observed and calculated patterns. Inset: main magnetic peaks at 4 K measured using a neutron wavelength of $\lambda_2 = 2.41 \text{ \AA}$.

5.2. Article III: Effect of chemical pressure induced by the $\text{La}^{3+}/\text{Y}^{3+}$ substitution on the magnetic ordering of $(\text{AMn}_3)\text{Mn}_4\text{O}_{12}$ quadruple perovskites

Temperature	285 K	190 K	4 K
$a, b, c(\text{\AA})$	7.45005(16), 7.34182(14), 7.45002(16)	7.44950(17), 7.32773(15), 7.45549(17)	7.47151(20), 7.30317(18), 7.46605(21)
$\beta(\circ), V(\text{\AA}^3)$	91.1214(13), 407.415(15)	91.1546(14), 406.897(16)	91.4225(16), 407.265(19)
B_{iso}	2.12(13)	Y 2a (0,0,0) 1.89(13)	4.63(30)
$\beta_{11}, \beta_{22}, \beta_{33}$	0.0056(18), 0.0064(11), 0.0035(17)	Mn A' 2b (0,1/2,0) 2c (1/2,0,0) 2d (1/2,1/2,0)	0.0086(24), 0.0051(14), 0.0068(22)
$\beta_{12}, \beta_{13}, \beta_{23}$	0.0, -0.00312(78), 0.0)	0.0, -0.00339(80), 0.0	0.0, -0.0112(14), 0.0
B_{iso}	0.418(75)	Mn B 4e (1/4,1/4,1/4) 4f (1/4,1/4,3/4) 0.368(79)	0.715(98)
T, z	0.16367(85), 0.29432(79)	O1 4i(x,0,z) 0.16354(80), 0.29504(82)	0.16314(83), 0.29389(89)
B_{iso} O1	0.942(77)	0.808(79)	0.053(67)
T, z	0.17962(88), 0.68360(87)	O2 4k(x,0,z) 0.17841(92), 0.68490(91)	0.17582(94), 0.69043(99)
B_{iso} O2	0.942(77)	0.808(79)	0.053(67)
T, y, z	0.01260(78), 0.30824(68), 0.17224(64)	O3 8j(x,y,z) 0.01311(71), 0.30816(72), 0.17168(67)	0.01341(93), 0.31512(108), 0.16776(95)
B_{iso} O3	1.368(50)	1.363(54)	2.421(87)
T, y, z	0.30977(65), 0.17796(69), -0.00977(64)	O4 8i(x,y,z) 0.30977(69), 0.17867(72), -0.00928(68)	0.31427(95), 0.18654(111), -0.00665(97)
B_{iso} O4	1.289(57)	1.363(54)	2.421(87)
R-Bragg(λ_1, λ_2), Global χ^2	6.66, 6.24, 5.65	6.99, 6.60, 6.12	8.77, 5.99, 7.99
Magnetic R-factor			4.97

Table 5.1: Crystal structure of $(\text{YMn}_3)\text{Mn}_4\text{O}_{12}$ as obtained from the Rietveld refinement of powder neutron diffraction data in the $I2/m$ space-group, as described in the text. The structure is given for the representative temperatures of 285 K (above T_S), 190 K (above $T_{N,B}$) and 4 K (below $T_{N,B}$). Numbers in parentheses indicate statistical uncertainty.

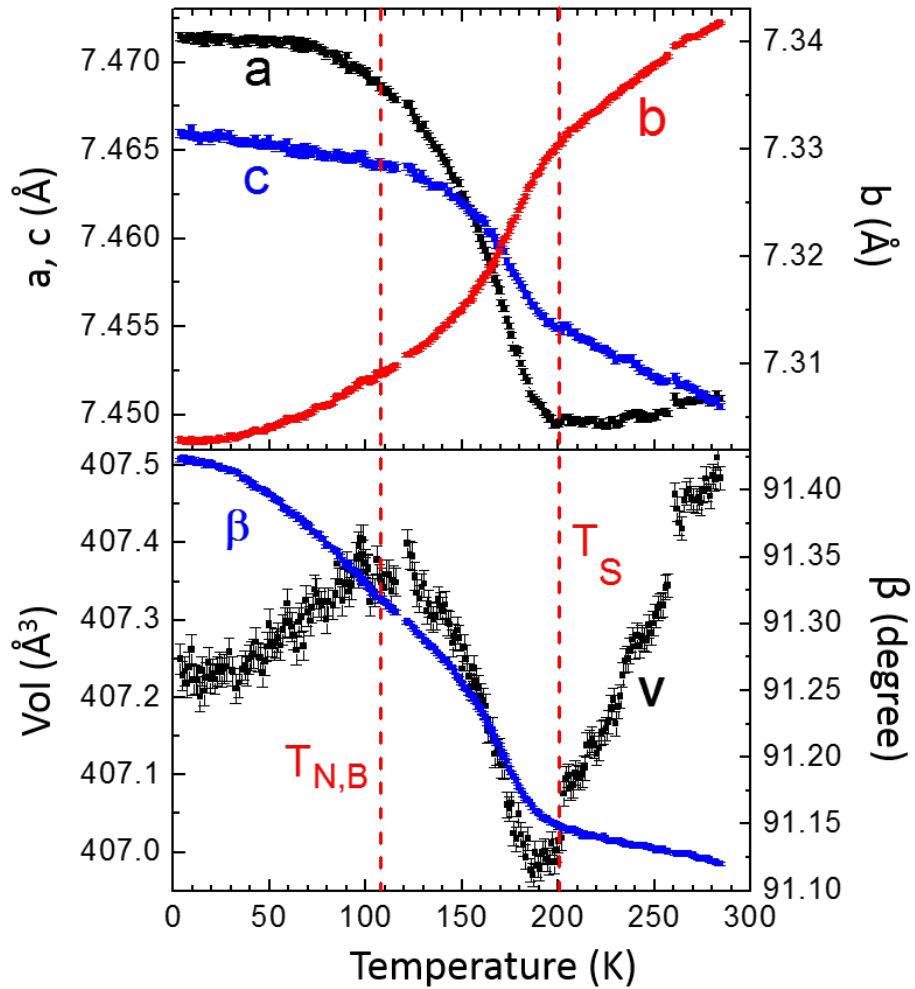


Figure 5.2: Unit cell parameters and unit cell volume of $(\text{YMn}_3)\text{Mn}_4\text{O}_{12}$ as a function of temperature obtained from the refinement of the powder neutron diffraction data. Broken lines indicate the temperatures of the second order structural phase transition at T_s and of the antiferromagnetic ordering of the B-sites at $T_{N,B}$.

5.2. Article III: Effect of chemical pressure induced by the $\text{La}^{3+}/\text{Y}^{3+}$ substitution on the magnetic ordering of $(\text{AMn}_3)\text{Mn}_4\text{O}_{12}$ quadruple perovskites

Namely, the bond lengths having a dominant component along the b -axis, *e.g.* Mn(2c)-O4, Mn(2b)-O3, Mn(2d)-O4, Mn(4e)-O1 and Mn(4f)-O2 (see Table 6.1), display a conventional behavior in the $T_s - T_{N,B}$ range. On the other hand, the bond lengths mainly contained in the ac -plane, *e.g.* Mn(4e)-O3, Mn(4f)-O4, Mn(2d)-O2, Mn(2d)-O1, Mn(2b)-O1 and Mn(2b)-O2, exhibit an anomalous increase with decreasing temperature. This difference is consistent with the change in the unit cell parameters discussed above and suggests a magnetostriction below $T_{N,B}$ which mainly involves the two shortest A' -O bonds, Mn(2b)-O3 and Mn(2c)-O4. In order to further analyze the structural changes occurring at T_s and at $T_{N,B}$, we calculated the bond valence sum (BVS) for all B and A' -sites. For the latter sites, we included the four next-nearest oxygen neighbors to obtain a realistic estimate of the valence. The result of the analysis is reported in Fig. 5.5. At first sight, the changes observed at T_s and $T_{N,B}$ are explained by a small charge redistribution, as observed in other quadruple perovskites [102], or by a change in the orbital occupancy. However, since the changes are much more pronounced at $T_{N,B}$, the changes may simply reflect a variation of internal strain, consistent with a scenario of magnetostriction, as discussed by Goodenough in the case of doped manganites with simple perovskite structure [45].

Magnetic structure. In Fig. 5.1, the temperature dependence of the diffraction patterns reveals an increase of the intensity of the (110), (-211), (-121) and (121) peaks at $T_{N,B}$, which indicates a long-range magnetic ordering with $\mathbf{k} = (0, 0, 0)$ propagation vector. A straightforward symmetry analysis indicates two distinct irreducible representations (irrep) corresponding to the $I2'/m'$ and $I2/m$ magnetic groups describing the magnetic structure. For each one of these two irreps, we have considered the three possibilities of ordering of the A' -sites alone, of the B -sites alone and of both sites. We obtained a successful refinement of the data only for the $I2'/m'$ structural model where the B sites are ordered while the A' sites are not. No refinement including the ordering of the A' -sites converged. The absence of magnetic order of the A' -sites in $(\text{YMn}_3)\text{Mn}_4\text{O}_{12}$ is surprising as the opposite result was reported for all previous $(\text{AMn}_3)\text{Mn}_4\text{O}_{12}$ compounds [46, 65, 47].

By taking into account the cubic pseudosymmetry of the $I2/m$ crystal symmetry, we shall finally propose the magnetic structure reported in Table 5.3 where the magnitude

Temperature	Bond orientation	285 K	190 K	4 K
<i>A'</i> sites				
Mn(2 <i>b</i>)-O1 ($\times 2$)	<i>ac</i> -plane	2.915(7)	2.908(7)	2.910(7)
Mn(2 <i>b</i>)-O2 ($\times 2$)	<i>ac</i> -plane	2.776(8)	2.786(8)	2.839(8)
Mn(2 <i>b</i>)-O3 ($\times 4$)	<i>bc</i> -plane	1.902(8)	1.898(8)	1.847(8)
Mn(2 <i>c</i>)-O3 ($\times 4$)	<i>bc</i> -plane	2.826(8)	2.829(8)	2.835(8)
Mn(2 <i>c</i>)-O4 ($\times 4$)	<i>ab</i> -plane	1.934(8)	1.935(8)	1.941(8)
Mn(2 <i>d</i>)-O1 ($\times 2$)	<i>ac</i> -plane	1.983(7)	1.974(7)	1.990(7)
Mn(2 <i>d</i>)-O2 ($\times 2$)	<i>ac</i> -plane	1.896(8)	1.897(8)	1.905(8)
Mn(2 <i>d</i>)-O4 ($\times 4$)	<i>bc</i> -plane	2.752(8)	2.746(8)	2.679(8)
<i>B</i> sites				
Mn(4 <i>e</i>)-O1 ($\times 2$)	$\sim b$ -axis	1.973(3)	1.973(3)	1.966(3)
Mn(4 <i>e</i>)-O3 ($\times 2$)	$\sim a$ -axis	1.898(7)	1.895(7)	1.916(7)
Mn(4 <i>e</i>)-O4 ($\times 2$)	$\sim c$ -axis	2.061(7)	2.060(7)	2.040(7)
Δ_{JT}		0.00114	0.00117	0.00066
Mn(4 <i>f</i>)-O2 ($\times 2$)	$\sim b$ -axis	1.969(3)	1.966(3)	1.958(3)
Mn(4 <i>f</i>)-O3 ($\times 2$)	$\sim a$ -axis	2.101(7)	2.106(7)	2.129(7)
Mn(4 <i>f</i>)-O4 ($\times 2$)	$\sim c$ -axis	1.909(7)	1.909(7)	1.927(7)
Δ_{JT}		0.00162	0.00171	0.00195

Table 5.2: Mn-O bond lengths (in Å) for the Mn *A'* and *B*-sites at the representative temperatures of 284, 190 and 4 K obtained from the data of Table 6.2. Numbers in parentheses indicate statistical uncertainty. $\Delta_{JT} = \frac{1}{3} \sum_{i=1}^3 \left[\frac{(d_i - \bar{d})}{\bar{d}} \right]^2$ indicates the Jahn-Teller parameter, where *i* labels the 3 inequivalent bonds of the MnO_6 octahedron.

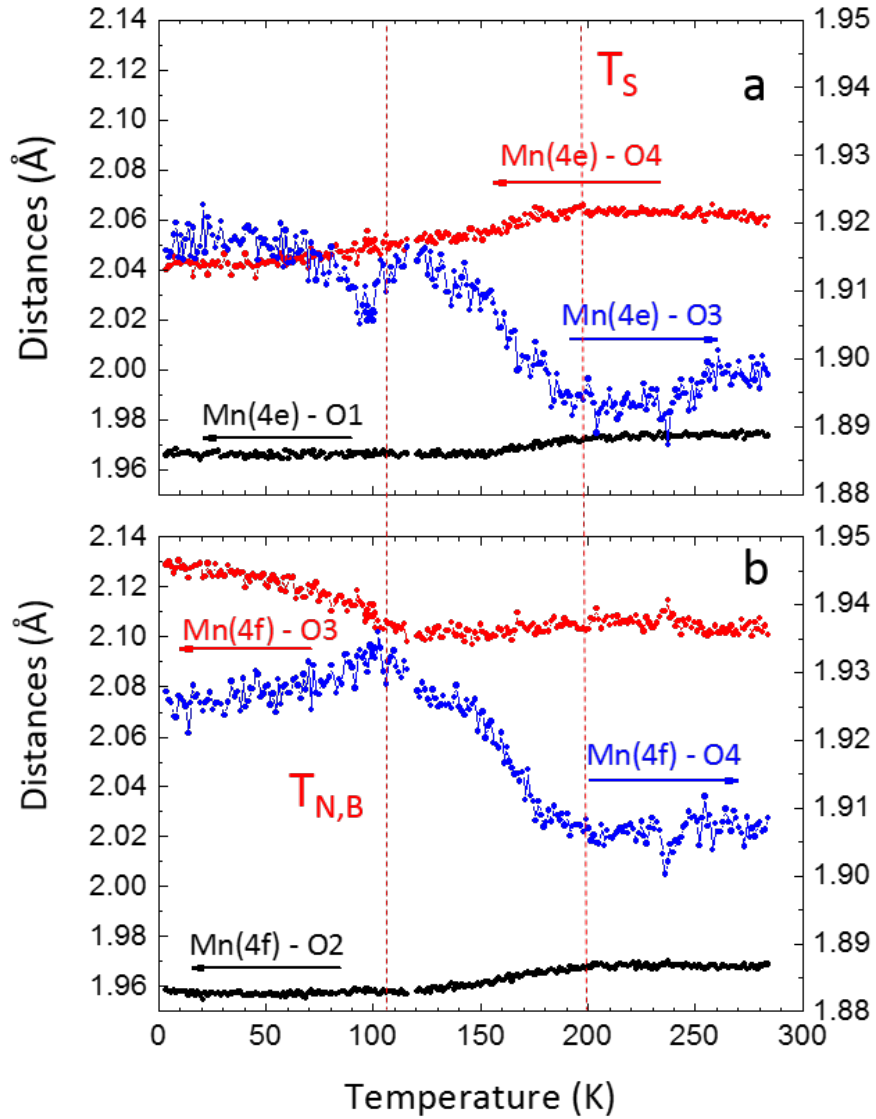


Figure 5.3: (color online) Temperature dependence of the Mn-O bond lengths of the B -sites obtained from the structural refinement of the powder neutron diffraction data. a: Mn (4e) sites. b: Mn (4f) sites. Red broken lines indicate the transitions at T_s and at $T_{N,B}$.

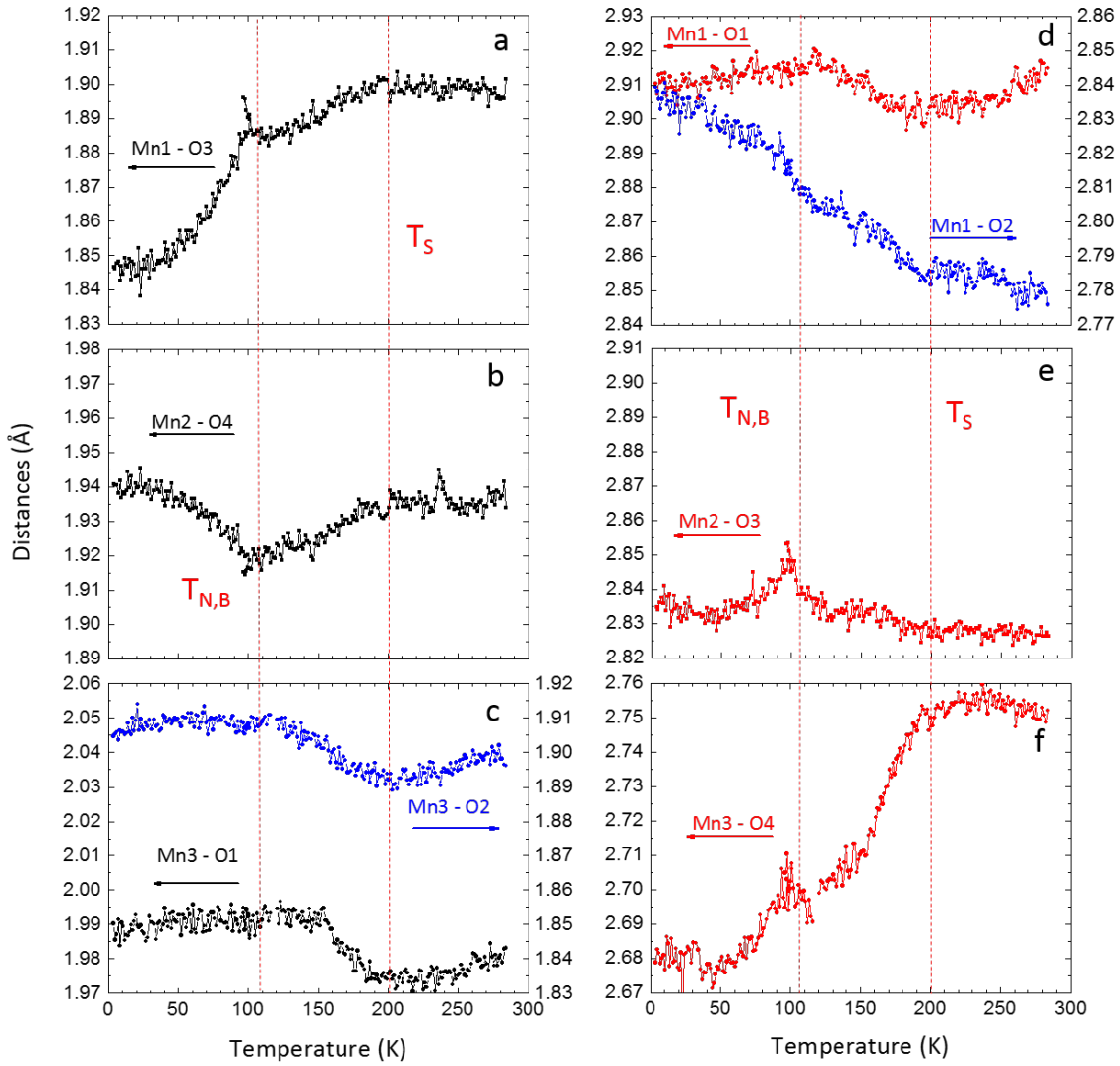


Figure 5.4: (color online) Mn-O bond lengths of the A' -sites as a function of temperature. Left panels: Mn-O bond lengths of the square-planar coordinated Mn(2b), Mn(2c) and Mn(2d) A' -sites. Right panels: the same as before for the Mn(2b), Mn(2c) and Mn(2d) A' -sites. Red broken lines are as above.

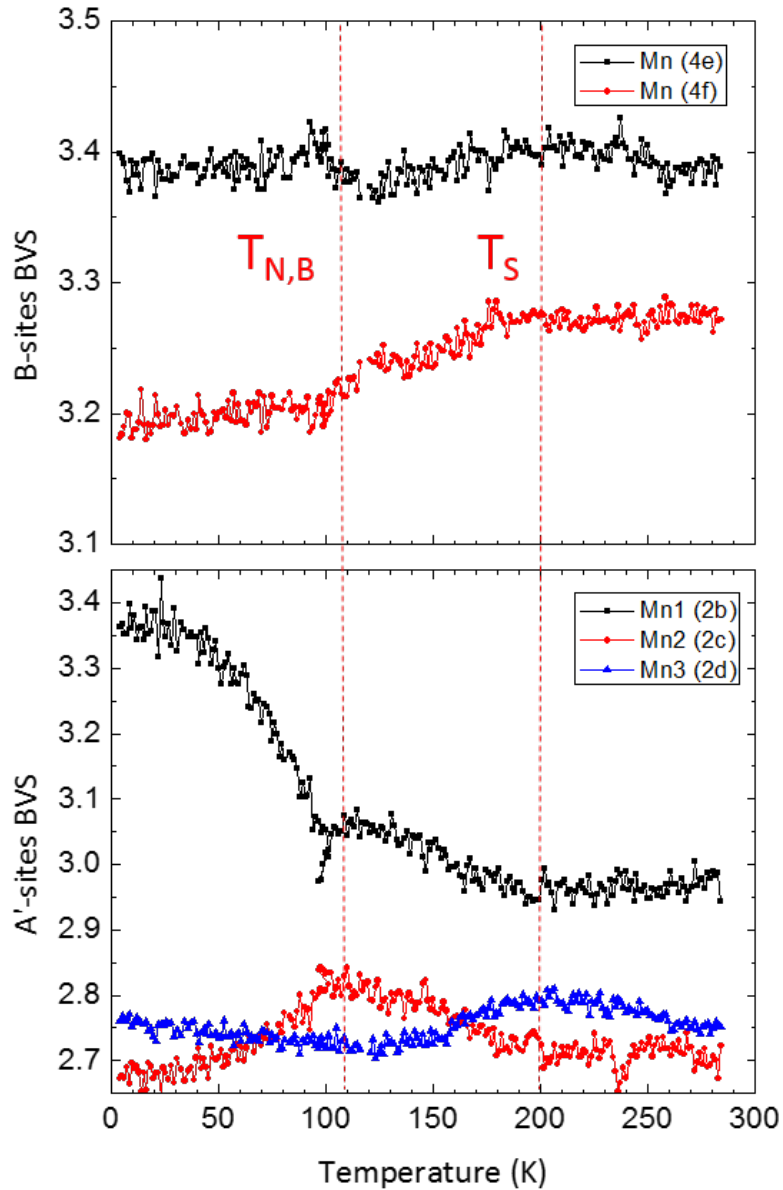


Figure 5.5: (color online) Temperature-dependence of the bond valence sum (BVS) of the Mn sites of $(\text{Y Mn}_3)\text{Mn}_4\text{O}_{12}$. Upper-panel: B -sites (4e and 4f). Lower-panel: A' -sites (2b, 2c and 2d). Red broken lines are as above.

of the magnetic moment is the same for the two $4e$ and $4f$ B -sites. This is a C -type structure similar to that previously reported for (LaMn₃)Mn₄O₁₂, where the coupling is AFM within the ac -plane and FM along the b -axis. The good quality of the refinement is apparent from the inset of Fig. 5.1 and from Table 5.3, where we report the refined structure for the lowest temperature measured, 3.7 K. At this temperature the refined value of the magnetic moment is $\mu = 3.5(7) \mu_B/\text{Mn}$, somehow lower than the value of $4.0 \mu_B$ expected for the Mn³⁺ ion in the high spin state ($S = 2$). It is well known that this reduction reflects the semicovalent character of the Mn-O bond in manganites. Notable is the pronounced canting of the moments along the b -axis explained by a Dzyaloshinskii-Moriya (DM) interaction [25] expected in tilted perovskitelike structures. In the present case, the canting angle of the moment with respect to the ac -plane is as large as $\sim 20^\circ$, much larger than previously reported in the counterpart simple-perovskite compound YMnO₃ [103]. This difference is ascribed to the much larger tilt of the MnO₆ octahedra characteristic of quadruple perovskites.

All diffraction patterns in the whole 4-285 K range measured were refined in sequential mode in order to obtain the temperature dependence of the nuclear and magnetic structure. The temperature dependence of the moment (see Fig. 5.7) exhibits a typical mean-field behavior with no anomalies, which confirms the absence of additional long-range magnetic orderings of the A' -sites. The refinement of the canted (M_y) component of the moment was carried out only below 80 K; at higher temperatures, this component becomes too small to be reliably refined.

	M_x	M_y	M_z	M	R_{Bragg}	R_{Mag}
Mn (B-sites)	-2.2(1)	1.21(1)	2.4(1)	3.52(15)	8.86/6.13	3.52/5.10

Table 5.3: B -site magnetic moment of (YMn₃)Mn₄O₁₂ in the $I2'/m'$ magnetic space group obtained from the structural refinement of the powder neutron diffraction data taken at 3.7 K.

B. Physical properties

Specific heat. Fig. 5.8 shows the temperature behavior of the specific heat, C_p , measured at constant pressure. As expected from the previous structural analysis, the data show two pronounced jumps, $\Delta C_p^{TS} \sim 65 \text{ J mol}^{-1} \text{ K}^{-1}$ and $\Delta C_p^{TN,B} \sim 22 \text{ J mol}^{-1} \text{ K}^{-1}$, at the structural and magnetic phase transitions, respectively. The jumps indicate

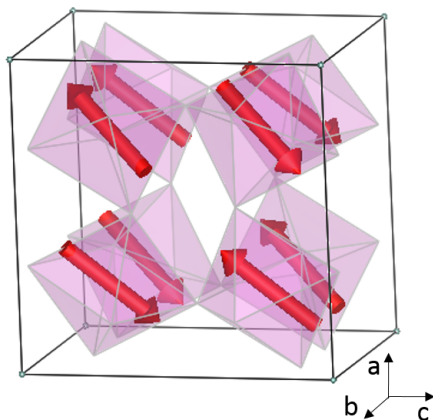


Figure 5.6: (Color online) C-type magnetic structure of $(\text{YMn}_3)\text{Mn}_4\text{O}_{12}$ as determined from the refinement of the neutron data (see Table III). Note the pronounced canting of the moments along the b -axis, as described in the text.

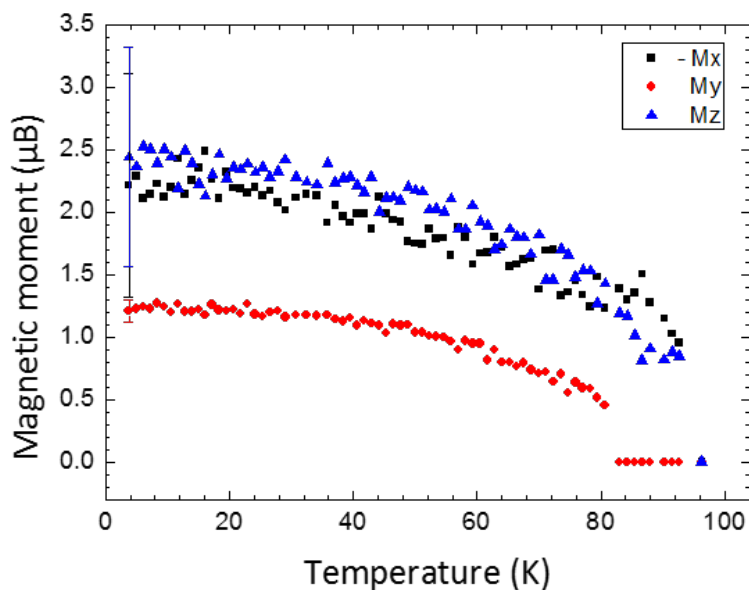


Figure 5.7: (Color online) Temperature dependence of the 3 components of the B -site moments obtained from the structural refinement of the powder neutron diffraction data. For clarity, error bars are indicated only at low temperature.

that the two transitions are of second order, consistent with the behavior of the cell volume. The size of the jump at $T_S \sim 2 \times T_{N,B}$ is more than two times larger than the jump at $T_{N,B}$, which is attributed to the fact that the transition at T_S involves the lattice energy, whilst the transition at $T_{N,B}$ mainly involves the electronic energy. The absence of any further transition at low temperatures confirms the surprising finding of no long-range ordering of the A' -ions. The C_p value at 300 K is $384 \text{ J mol}^{-1} \text{ K}^{-1}$ is to be compared to the Dulong-Petit value of $498 \text{ J mol}^{-1} \text{ K}^{-1}$, which suggests a Debye temperature larger than 300 K.

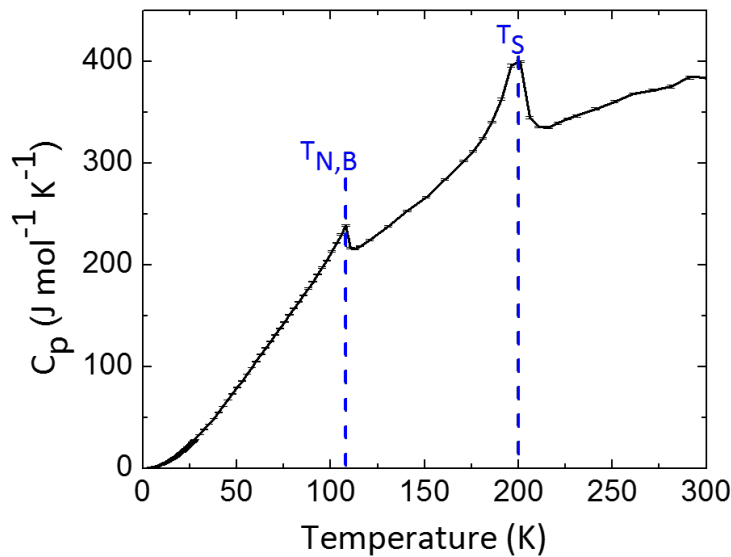


Figure 5.8: (Color online) Temperature dependence of the specific heat of $(\text{YMn}_3)\text{Mn}_4\text{O}_{12}$. Note the anomalies at the magnetic ordering of the B sites at $T_{N,B}=108 \text{ K}$ and at the structural transition, $T_s=200 \text{ K}$, as discussed in Sec. III. A.

DC and AC Magnetization. In Fig. 5.9, we plot the ZFC and FC DC magnetization curves, $M(T)$, measured at different fields of 0, 10, 50 and 100 Oe. The analysis of the paramagnetic region above $T_{N,B}$ highlights an anomaly of the $1/\chi$ curve at T_s , which indicates that the structural transition discussed above alters the superexchange interaction between Mn ions. Above this temperature, the $1/\chi$ curve displays a conventional Curie-Weiss behavior characterized by a Weiss constant $\Theta_W = -105 \pm 5 \text{ K}$, which confirms the predominant AFM nature of Mn-O-Mn superexchange interaction.

In the ZFC curves, a sharp field-dependent Hopkinson peak [104] at $T_{N,B}$ reflects a marked magnetic anisotropy, consistent with the C -type magnetic structure proposed. A fit of the Curie constant yields an effective moment of $5.02 \mu_B$, close to the value $4.9 \mu_B$ expected for the high-spin state ($S = 2$) of Mn^{3+} ions by assuming a quenched orbital momentum. Below $T_{N,B}$, the ZFC and FC curves exhibit the characteristic behavior of a weak ferromagnet. This behavior, observed also in the ZFC curve measured at zero-field (see black curve of Fig. 5.9), is quantitatively explained by a small difference of $\approx 0.004 \mu_B$ in the magnetic moments of the two $4e$ and $4f$ B sites, which is allowed by symmetry. This analysis justifies the above assumption of a tetragonal pseudosymmetry.

In the magnetic phase below $T_{N,B}$, the magnetization of the DC ZFC curves displays a broad peak in the at $T^*=50\text{-}70$ K range. The intensity of this peak scales with the field and no peak is observed in the first magnetization curve taken after having completely suppressed the residual field of the magnet, as described in the experimental section. Under these conditions, the field is not larger than the earth magnetic field. The absence of any feature in the first magnetization curve below $T_{N,B}$ is coherent with the absence of additional magnetic peaks in the neutron diffraction data, which are also taken at zero field. The appearance of a broad peak in the ZFC data not observed in the first magnetization curve suggests a latent magnetic ordering at T^* .

In order to investigate the origin of this broad peak, we performed AC susceptibility measurements as a function of frequency, f , up to 10 kHz for field amplitudes in the 0.01-10 oersted range. Interestingly, a sharp peak is observed at the same temperature T_s where the dc data exhibit a broad peak for all amplitudes and for all frequencies. Neither the intensity, nor the shape of the peak changes significantly either with field or with frequency up to 10 kHz. Fig. 5.10 shows representative curves of the real part χ' for different fields taken at $f=57$ Hz. Further work is needed to elucidate the origin of this magnetic response, which supports the picture of latent magnetic ordering.

Fig. 5.11 shows the dependence of the magnetization as a function of field up to 8 T measured at 5 and 65 K. At both temperatures, the linear behavior observed at high field and the existence of a sizable hysteresis support the picture of weak FM. Interestingly, the coercive field is significantly larger than in other $(\text{AMn}_3)\text{Mn}_4\text{O}_{12}$ compounds

[46, 105, 40, 106, 107], which is attributed to a stronger magnetic anisotropy.

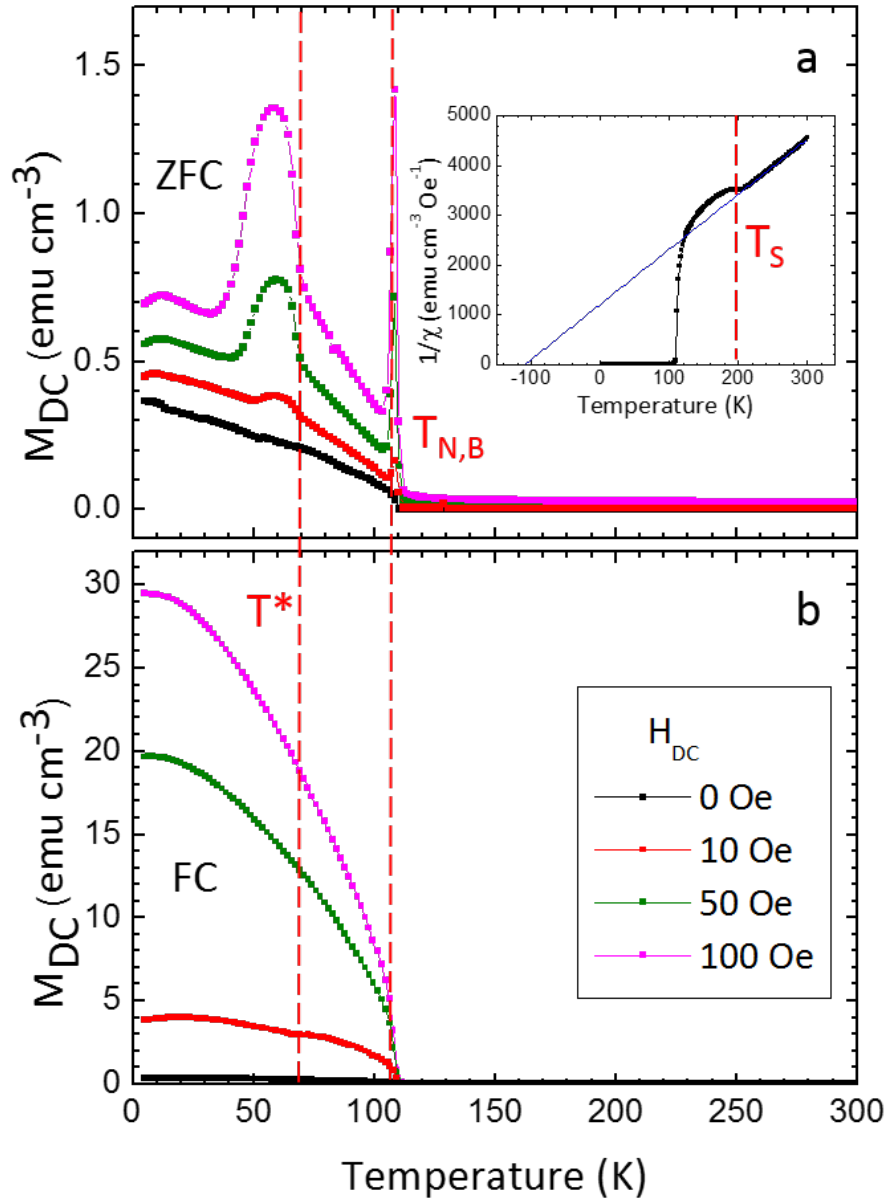


Figure 5.9: (a) ZFC DC magnetization curves measured at 0, 50 and 100 Oe. Inset: Curie-Weiss fit of the inverse susceptibility in the paramagnetic 200 - 300 K region (b) FC DC magnetization curves at 0, 50 and 100 Oe.

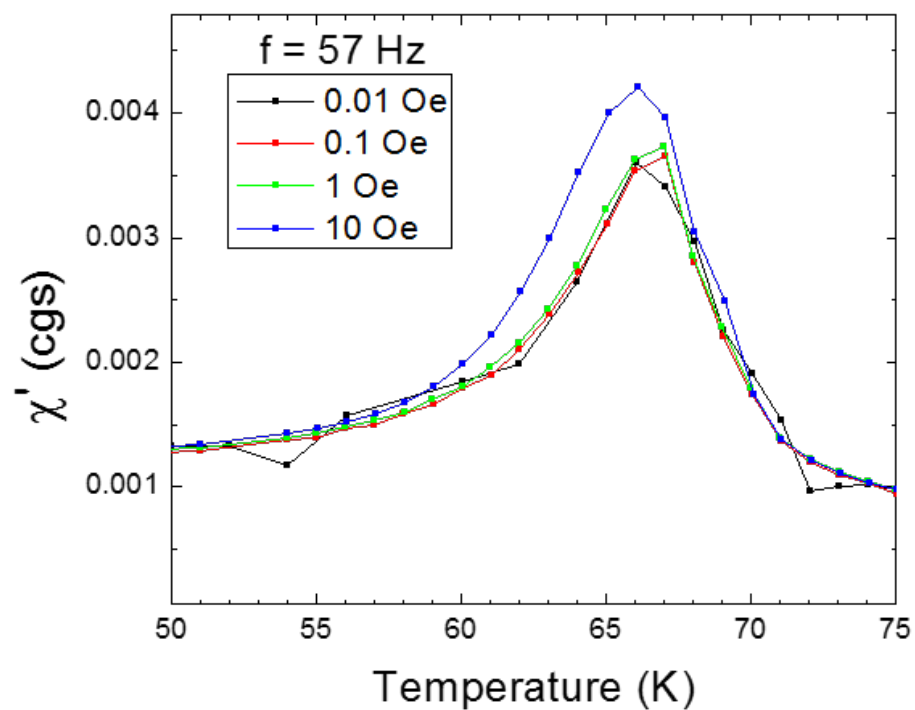


Figure 5.10: Real part of the AC susceptibility measured at a frequency $f=57$ Hz for different AC fields indicated in the legend. No significant changes are observed by changing either the field amplitude or f , as explained in the text.

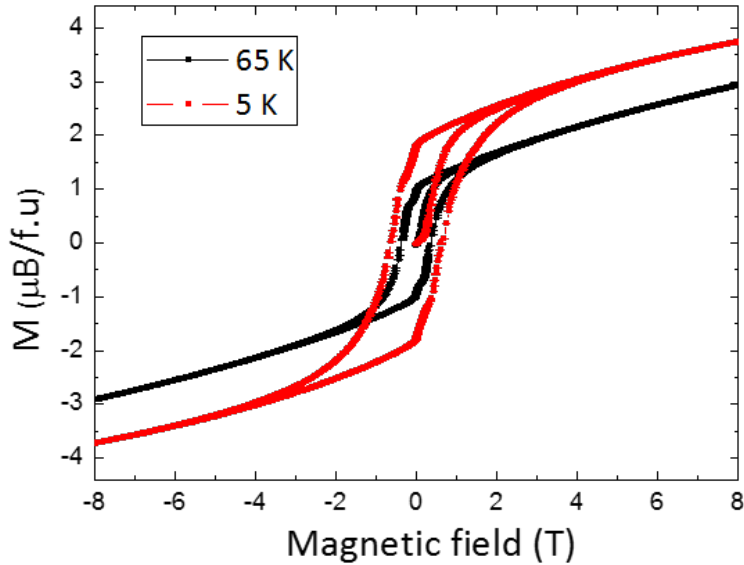


Figure 5.11: Magnetization as a function of field up to 8 T at 5 and 65 K.

IV. CONCLUSION

In conclusion, we have reported on the successful high pressure synthesis of the single valent Mn^{3+} $(\text{YMn}_3)\text{Mn}_4\text{O}_{12}$ quadruple perovskite, where the insertion of the small Y^{3+} ion in the A site exerts a significant chemical pressure, which is expected to enhance the strength of the superexchange interaction between neighboring Mn^{3+} ions. A systematic study of the structural and physical properties confirms this expectation; we have found a significant 30 K enhancement of the AFM ordering temperature of the Mn^{3+} B -sites with respect to the case of the isostructural and isovalent compound $(\text{LaMn}_3)\text{Mn}_4\text{O}_{12}$ reported previously. We argue that this enhancement is promising in view of future developments of quadruple perovskites as magnetic ferroelectrics. On the other hand, we have surprisingly found no long-range ordering of the Mn^{3+} A' -sites; instead, a broad peak of the dc magnetization at $T^*=50\text{-}70$ that disappears in the first magnetization ZFC curve and a sharp peak of the ac susceptibility at the same temperature suggests a latent order of these sites. A further unexpected feature of $(\text{YMn}_3)\text{Mn}_4\text{O}_{12}$ is the occurrence of a structural second-order phase transition at $T_s = 200$ K, which concomitant to an anomalous behavior of the unit cell and of most

Mn-O bonds. A BVS analysis suggests that this transition is associated with a partial charge redistribution involving both A' and B Mn sites, which may alter the AFM interaction between neighboring Mn ions. Further experiments are needed to explain the absence of long-range ordering of the A' sites and to investigate the origin of the structural transition at T_s and the possibility of magnetic ferroelectricity.

ACKNOWLEDGMENTS

The authors are grateful to F. Bolzoni, R. Cabassi, G. Calestani, B. Dabrowski and M-B. Lepetit for stimulating discussions, T. Roisnel, L-M. Chamoreau, D. Frost and H. Keppler for assistance in the structural refinement, in the single-crystal diffraction measurements and in the high-pressure synthesis and gratefully acknowledge the support of the Bayerisches Geoinstitut, the German Science Foundation and the Laue-Langevin Institut. M.V. gratefully acknowledges financial support from the "Leonardo da Vinci" doctoral program of the Franco-Italian university.

5.3 Supplementary information on article III

In this Supplemental Information section, we provide a summary of the single-crystal X-ray diffraction study carried out at room temperature on $(\text{YMn}_3)\text{Mn}_4\text{O}_{12}$ sample, as described in the experimental section of the manuscript.

Empirical formula	YMn₇O₁₂
Formula weight	665.49
Temperature	293 K
Crystal system	monoclinic
Space group	<i>I</i> 2/ <i>m</i>
a	7.4221(8) Å
b	7.3219(7) Å
c	7.4232(7) Å
α	90°
β	91.100(9)°
γ	90°
Volume	403.33(7) Å ³
Z	2
ρ _{calc}	5.480 g/cm ³
μ	17.767 mm ⁻¹
F(000)	620.0
Crystal size	0.045 × 0.037 × 0.033 mm ³
Radiation	MoK _α (λ = 0.71073)
2θ range for data collection	7.69° to 52.736°
Index ranges	-9 ≤ h ≤ 9, -8 ≤ k ≤ 9, -9 ≤ l ≤ 3
Reflections collected	715
Independent reflections	441 [R _{int} = 0.0209, R _{sigma} = 0.0390]
Data/restraints/parameters	441/0/56
Goodness-of-fit on F ²	0.968
Final R indexes [I >= 2σ (I)]	R ₁ = 0.0397, wR ₂ = 0.0897
Final R indexes [all data]	R ₁ = 0.0765, wR ₂ = 0.1102
Largest diff. peak/hole	0.91/-0.75 e Å ⁻³

 Table 5.4: Single-crystal data and structure refinement for (YMn₃)Mn₄O₁₂.

Atom	x	y	z	B(eq)
Y1	0	0	0	1.69(5)
Mn1	0	1/2	0	0.87(5)
Mn2	1/2	0	0	0.98(5)
Mn3	1/2	1/2	0	0.85(5)
Mn4	1/4	1/4	1/4	0.57(4)
Mn5	1/4	1/4	3/4	0.63(4)
O1	0.1659(10)	0	0.3001(9)	1.07(11)
O2	0.1826(10)	0	0.6834(9)	0.63(4)
O3	0.0140(7)	0.3074(7)	0.1715(6)	0.95(10)
O4	0.3113(7)	0.1728(7)	0.0114(6)	1.26(11)

 Table 5.5: Fractional atomic coordinates and equivalent isotropic displacement parameters, B_{eq} , obtained from the refinement of the single-crystal X-ray diffraction data. B_{eq} is defined as 1/3 of the trace of the orthogonalized β_{ij} tensor.

5.3. Supplementary information on article III

Atom	β_{11}	β_{22}	β_{33}	β_{23}	β_{13}	β_{12}
Y1	0.0091(4)	0.0066(4)	0.0075(4)	0	-0.0024(3)	0
Mn1	0.0076(5)	0.0022(5)	0.0022(4)	0	-0.0010(4)	0
Mn2	0.0037(5)	0.0018(5)	0.0078(5)	0	-0.0006(4)	0
Mn3	0.0038(5)	0.0064(5)	0.0015(4)	0	-0.0004(3)	0
Mn4	0.0033(3)	0.0023(3)	0.0022(3)	0.0000(2)	-0.0005(2)	0.0003(3)
Mn5	0.0040(3)	0.0021(3)	0.0026(3)	0.0000(2)	-0.0008(3)	0.0004(3)
O1	0.0068(14)	0.0041(18)	0.0039(14)	0	0.0018(11)	0
O2	0.0040(3)	0.0021(3)	0.0026(3)	0.0000(2)	-0.0008(3)	0.0004(3)
O3	0.0025(11)	0.0055(11)	0.0050(11)	-0.0029(11)	-0.0011(7)	0.0004(1)
O4	0.0100(11)	0.0037(11)	0.0036(11)	0.0000(7)	-0.0007(7)	0.0051(11)

Table 5.6: Anisotropic displacement parameters obtained from the refinement of the single-crystal X-ray diffraction data.

Chapter 6

Multiferroic properties of the new quadruple perovskite $(\text{YMn}_3)\text{Mn}_4\text{O}_{12}$

6.1 Motivations

Dans le chapitre précédent nous avons présenté une étude complète des structures cristalline et magnétique de la nouvelle pérovskite quadruple $(\text{YMn}_3)\text{Mn}_4\text{O}_{12}$ obtenue sous haute pression et qui présente à température ambiante le même groupe d'espace centrosymétrique que le LMO. Cette étude, couplée à des mesures magnétiques a permis de mettre en évidence une transition structurale du deuxième ordre à $T_s = 200$ K; une transition magnétique à $T_{N,B} = 108$ K correspondant à l'orientation des sites B et une anomalie magnétique induite par le champ à $T^* = 70$ K dont l'origine reste inconnue ainsi que l'absence d'orientation magnétique des sites A' . Ces effets démontrent l'existence de plusieurs interactions magnétiques en compétition qui pourraient être à l'origine des propriétés multiferroïques. Dans un deuxième temps nous avons donc cherché à caractériser ces éventuelles propriétés multiferroïques par des mesures de pyrocourants et de la constante diélectrique ainsi qu'en déterminant la structure cristalline exacte à basse température par diffraction de rayonnement synchrotron. Ce chapitre reporte les résultats de cette étude réalisée entre l'IMEM-CNR, l'IMPMC et la ligne CRISTAL du synchrotron SOLEIL dans le cadre du projet BAG de B. Baptiste.

6.2 Article IV: Evidence of centrosymmetry breaking in the magnetic ferroelectric $(\text{YMn}_3)\text{Mn}_4\text{O}_{12}$

STATUS: Manuscript in preparation

Evidence of centrosymmetry breaking in the magnetic ferroelectric $(\text{YMn}_3)\text{Mn}_4\text{O}_{12}$

M. Verseils,¹ R. Cabassi,² B. Baptiste,¹ F. Mezzadri,² D. Delmonte,² F. Bolzoni,² E. Gilioli,² and A. Gauzzi¹

¹ *Institut de Minéralogie, de Physique des Matériaux et de Cosmochimie - Sorbonne Université, UPMC, CNRS, IRD, MNHN - 4, place Jussieu, 75005 Paris, France*

² *Istituto dei Materiali per Elettronica e Magnetismo, CNR, Area delle Scienze, 43100 Parma, Italy*

Abstract

We report on the unusual properties of magnetic ferroelectricity of the quadruple perovskite $(\text{YMn}_3)\text{Mn}_4\text{O}_{12}$, where the comparatively small Y^{3+} ion exerts a large chemical pressure on the crystal structure. Pyrocurrent, dielectric constant and transport measurements performed on polycrystalline samples give evidence of spontaneous electric polarization reaching the remarkable saturation value $P_{sat} = 0.54 \mu\text{C cm}^{-2}$, two times higher than the value previously reported in the related compound $(\text{CaMn}_3)\text{Mn}_4\text{O}_{12}$. Surprisingly, ferroelectricity shows up at a characteristic temperature, $T^* = 70 \text{ K}$, where magnetic susceptibility shows a large anormal peak not compatible with a long range magnetic order, as reported previously [108]. The observation of ferroelectricity is consistent with complementary single-crystal synchrotron x-ray diffraction data showing the appearance of a commensurate non-centrosymmetric structural modulation at the structural phase transition $T_s = 200 \text{ K}$. To the best of our knowledge, this is the first unambiguous observation of non-centrosymmetric distortion in a magnetic ferroelectric. The P -values expected in single-crystals bulk or thin films samples being significantly larger than those reported here suggest that $(\text{YMn}_3)\text{Mn}_4\text{O}_{12}$ may be a suitable material for practical multiferroic applications.

I. INTRODUCTION

During the last years, magnetic ferroelectrics have attracted a great deal of interest for their inherently strong magnetoelectric coupling; this property is promising for novel concepts of electronic devices, such as nonvolatile rapid memories, where magnetization can be switched by an electric field with a modest energy consumption. One fundamental step towards applications is the capability of tuning the multiferroic properties, such as the strength and the orientation of the spontaneous polarization, P , in suitable materials. At present, this long-term objective appears to be challenging considering that the structural signatures of the magnetic ferroelectrics hitherto studied are elusive. Indeed, only weak modulations of ionic positions could be evidenced in TbMnO₃ [67, 86] and (CaMn₃)Mn₄O₁₂ [87] which are the most studied magnetic ferroelectrics and, in a large case of type-II multiferroics, experiments (diffraction, spectroscopy) failed to reveal the expected symmetry lowering [66]. It is therefore important to elucidate this point in order to single-out the control parameters of the spontaneous polarization.

We argue that the lack of strong structural or spectroscopic signatures in magnetic ferroelectrics is due to the fact that, as discussed by Levanyuk and Sannikov [13], the symmetry properties of the second-order phase transition in these materials are fundamentally different from those of ordinary ferroelectric transitions. We recall that, in the latter case, the order parameter is the vector of spontaneous polarization, P , which completely accounts for the reduction of symmetry at T_c . On the other hand, in magnetic ferroelectrics (improper ferroelectrics), the principal order parameter is the magnetic order. Therefore (i) the symmetry of the ferroelectric phase is not described by the maximal polar subgroup of the space group of the initial phase and (ii) the symmetry properties of the magnetic order parameter differ from those of the ferroelectric polarization. This circumstance implies that the order parameter entering in the Landau thermodynamic potential of magnetic ferroelectrics is formed by at least two scalar components, ξ and η , forming second-order invariants either of the type $\xi\eta P$ or $(\xi^2 - \eta^2)P$. It follows that the polarization is proportional to the square of the order parameter, i.e. $P \propto \rho^2 = \xi^2 + \eta^2$, and the bilinear product $\xi\eta$ (or difference $\xi^2 - \eta^2$) transforms as a polar vector, while the individual components, ξ or η , do not.

In practice, the components, ξ and η , correspond to normal coordinates describing the lattice distortion at the transition. Thus, contrary to the case of ordinary ferroelectrics, the soft mode in the paraelectric phase of magnetic ferroelectric is not infrared active, which explains the lack of visible anomalies in the infrared spectrum at the transition. A similar situation occurs for the Raman-active modes, since the components of the Raman tensor, χ_{ij} , are quadratic in the normal coordinates (i.e. in ξ and η). Therefore, in the paraelectric phase, the soft mode does not contribute to the Raman intensity either (see chapter 4). Finally, the lack of evidence of noncentrosymmetric distortion by means of diffraction methods is explained by the existence of four degenerate phases with different values of ξ and η and with opposite orientations of the polarization, as discussed in [13]. This leads to the formation of a domain structure with zero average polarization, in the absence of a poling field.

In a recent work [108], we have reported on the successful synthesis of the new quadruple perovskite [42] phase $(\text{YMn}_3)\text{Mn}_4\text{O}_{12}$, on its crystal and magnetic structure and on its magnetic and thermodynamic properties. This preliminary work has given evidence of three characteristic temperatures, $T_s = 200$ K; $T_{N,B} = 108$ K and $T^* = 70$ K. $T_{N,B}$ was unambiguously attributed to the antiferromagnetic ordering of the B -sublattice, while T_s was found to correspond to a second-order structural transition described by significant structural distortions with no apparent change of symmetry. On the other hand, at T^* we observed a marked field-dependent anomaly of the dc magnetic susceptibility.

The strikingly different magnetic orderings observed in $(\text{LaMn}_3)\text{Mn}_4\text{O}_{12}$ and in $(\text{YMn}_3)\text{Mn}_4\text{O}_{12}$ are surprising considering the very similar crystal structures (space group $12/m$). This difference offers an ideal opportunity to investigate the sensitivity of a potential ferroelectric polarization to the magnetic structure. In order to address this issue, in the present work, we have studied the ferroelectric properties of $(\text{YMn}_3)\text{Mn}_4\text{O}_{12}$ by means of pyrocurrent, dielectric constant and transport measurements on several polycrystalline samples. Considering that any modification of the crystal structure or of the magnetic response is expected to affect the multiferroic properties of magnetic ferroelectric, in the present work, we have also investigated in detail the structural modifications at T_s and the magnetic anomaly at T^* by means of high-

resolution synchrotron diffraction on a single crystals and of magnetic susceptibility, respectively. Our results give evidence of a large spontaneous polarization occurring at T^* and of a structural modulation at T_s which breaks the inversion symmetry.

II. EXPERIMENTAL

Sample preparation Polycrystalline samples and ~ 0.2 mm-size single-crystals were obtained from a solid state reaction of a stoichiometric mixture of Y₂O₃ and Mn₂O₃ powders at 9 GPa and 1300°C for 2 hours using a multi-anvil press, as described in [108]. Electrical measurements were carried out on disk obtained by polishing the as-prepared polycrystalline samples using a *Leica* mechanical polisher. Typical diameter and thickness of the disks were ~ 1 mm and ~ 60 -600 μm , respectively. Suitable low contact-resistance electrodes were made by covering each disk surface with silver paste. The single-crystal used for X-ray synchrotron diffraction was selected from the powders.

Pyroelectric current and dielectric constant measurements Pyroelectric currents (I_p) were measured upon heating up the disk samples using a *Keithley 6517B* electrometer after having poled the sample at a suitable temperature, T_p , using a source meter *Keithley 2400*.

The capacitance of the polycrystalline disks was determined from complex impedance measurement performed with a commercial *HP4824A* LCR meter covering the 20 - 10⁶ Hz frequency range from and using an ac voltage of $V_s=200$ mV. For both measurements, the temperature control was achieved by using the liquid helium cryostat of a commercial Quantum Design magnetic properties measurement system (MPMS).

Transport Resistance measurements in the 60-300 K range were performed using either a commercial Quantum Design Physical Property Measurement System or a commercial Quantum Design SQUID. The resistivity measurements carried out in the van der Pauw configuration showed low contact resistances, negligible as compared to the sample resistance. This allowed us to perform impedance measurements in the simple two-contact geometry suitable for our disk-shaped samples.

Single-crystal X-ray synchrotron diffraction Several single-crystals of (YMn₃)Mn₄O₁₂ were tested in advance with a 4-circles diffractometer of the drx platform of IMPMC

(*Rigaku/Oxford* diffraction *Xcalibur S*). The less twinned crystal, of $\sim 10\mu\text{m}$, was further analyzed under synchrotron radiation by using a 4-circles diffractometer of the beamline CRISTAL at SOLEIL (Saint Aubin, France). The sample was mounted onto a kapton (MiTeGen) microwire with the help of high-vacuum grease. Three acquisitions were collected, at 50, 150 and 300 K using the electron with 18.46 KeV energy corresponding to a wavelength $\lambda = 0.6717 \text{ \AA}$. Data reduction, cell refinement, space-group determination, scaling and multiscan absorption correction [96] were performed using *CrysaAlisPro* software [97]. The structure was solved through *Olex2* program [98] by direct methods using *SHELXT* [99]. The refinement was then carried out with *SHELXL-2013* [99] by full-matrix least squares minimization and difference Fourier methods. All atoms were refined with anisotropic displacement parameters.

III. RESULTS

Dielectric and ferroelectric properties

We first analyzed the influence of the poling temperature, T_p , on the pyrocurrent peak shape. In Fig. 6.1 we report the curve obtained for a poling electric field of $3.2 \times 10^5 \text{ V/m}$ and a warming rate of 1.3 K/min. Note that the size and the width of the peak is reduced and its position shifts towards lower temperature with decreasing T_p . The peaks obtained for $T_p = 104 \text{ K}$ or 75 K are similar; they are larger and higher than the peak obtained for $T_p = 55 \text{ K}$ indicating that the ferroelectric critical temperature lies between 75 and 55 K. The peaks obtained at high T_p present a shoulder around 40 K which seems to be the tail of the pyrocurrent peak obtained for $T_p = 48 \text{ K}$. This suggests that it exists a secondary ferroelectric transition around 45 K. Thus we put forward the hypothesis that the broad peak obtained for $T_p \sim 100 \text{ K}$ is in fact a superposition of two pyrocurrent peaks centered at $T_1 = 65\text{-}70 \text{ K}$ and $T_2 = 45 \text{ K}$.

We also measured the pyrocurrent curve, $I(T)$, under various warming rates on the same sample with constant $T_p = 100 \text{ K}$ and constant poling electric field $E = 3.2 \times 10^5 \text{ V/m}$. As usual, the polarization P was obtained by integration of the I curve. The results plotted in Fig. 6.2 show that the warming rate has practically no influence on the saturation value of P , which consistently fall in the $0.20 - 0.22 \mu\text{C cm}^{-2}$ range. In addition, the I and P curves obtained by inverting the sign poling voltage, E , also

change sign with no changes of magnitude, as expected.

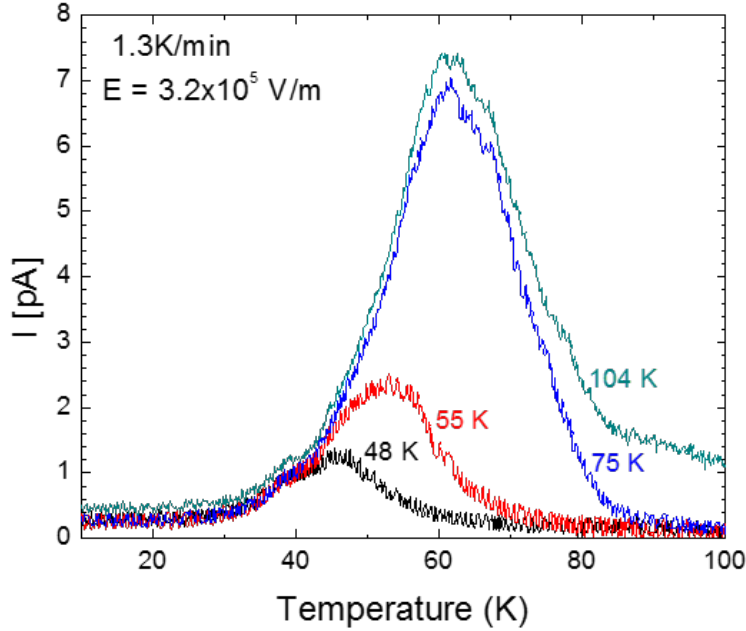


Figure 6.1: Pyroelectric currents obtained for different poling temperatures $T_p = 48, 55, 75$ and 104 K.

A recent study [109], considered the possibility of measuring pyroelectric currents produced by extrinsic effects, such as thermally activated space-trapped charges at grain boundaries. Such extrinsic effects are expected to vary as a function of warming rate, which is not the case of our results. Our data analysis further indicates that the contribution of trapped charges, if any, would be negligible with respect to that of the intrinsic polarization of the sample. The P -values at 8 K are reported on Fig 6.3 for samples with different thicknesses. The experimental points nicely describes the full $P(E)$ curve up to the saturation region where the P values level off at $P_{sat} = 0.54 \mu\text{C cm}^{-2}$ for a poling voltage $E = 3.5 \times 10^6 \text{ V/m}$. This value is twice as large the record value previously reported for the spin-spiral magnet $(\text{CaMn}_3)\text{Mn}_4\text{O}_{12}$ [41, 49], which is very promising by taking into account that much larger values are expected in single-crystals or thin films [110]. Similar to the case of magnetic ferroelectrics reported previously, such as $(\text{CaMn}_3)\text{Mn}_4\text{O}_{12}$ and TbMnO_3 , our attempts to measure the ferroelectric

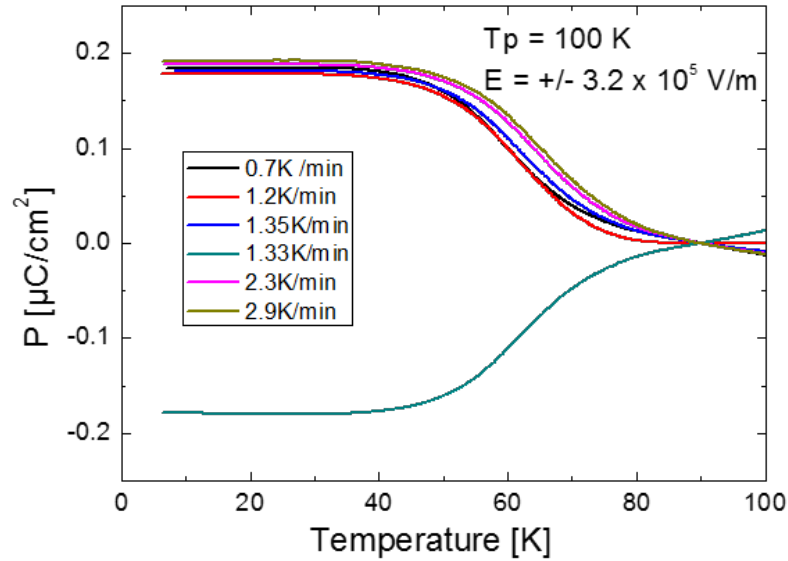


Figure 6.2: Polarizations obtained by integration from pyroelectric current measurements performed under various warming rates of 0.7, 1.2, 1.35, 1.33, 2.3 and 2.9 K/min.

hysteresis loop have been unsuccessful. This is attributed to the comparatively low P -value as compared to the values of ordinary ferroelectrics, such as BiFeO_3 . Larger single-crystals would be required to perform these alternative measurements.

In the lack of such direct measurement of the ferroelectric hysteresis cycle, it is a widely use method to complete pyroelectric measurements with the measure of capacitance (C) as a function of temperature, since a ferroelectric material must present an anomaly in the dielectric constant at the ferroelectric transition. The capacitance of $(\text{YMn}_3)\text{Mn}_4\text{O}_{12}$ disks vs. temperature at various frequencies is reported in Fig 6.4. As explained in [111] a Schottky barrier can occur on the electrodes because of metal-semiconductor junctions, as a consequence the value of C is not indicative but we can comment on its thermal dependence. The curves exhibit two anomalies, one peak and one discontinuity of the slope, at $T_1=72$ K and at $T_2=45$ K, respectively. This supports our previous hypothesis of two critical temperatures for polarization in the material. The position of these anomalies is independent of frequency, but the intensity of the first one (T_1) is enhanced with increasing frequency and is not visible at the lowest frequency measured (1 kHz). We also have reported the curve of the ZFC magnetiza-

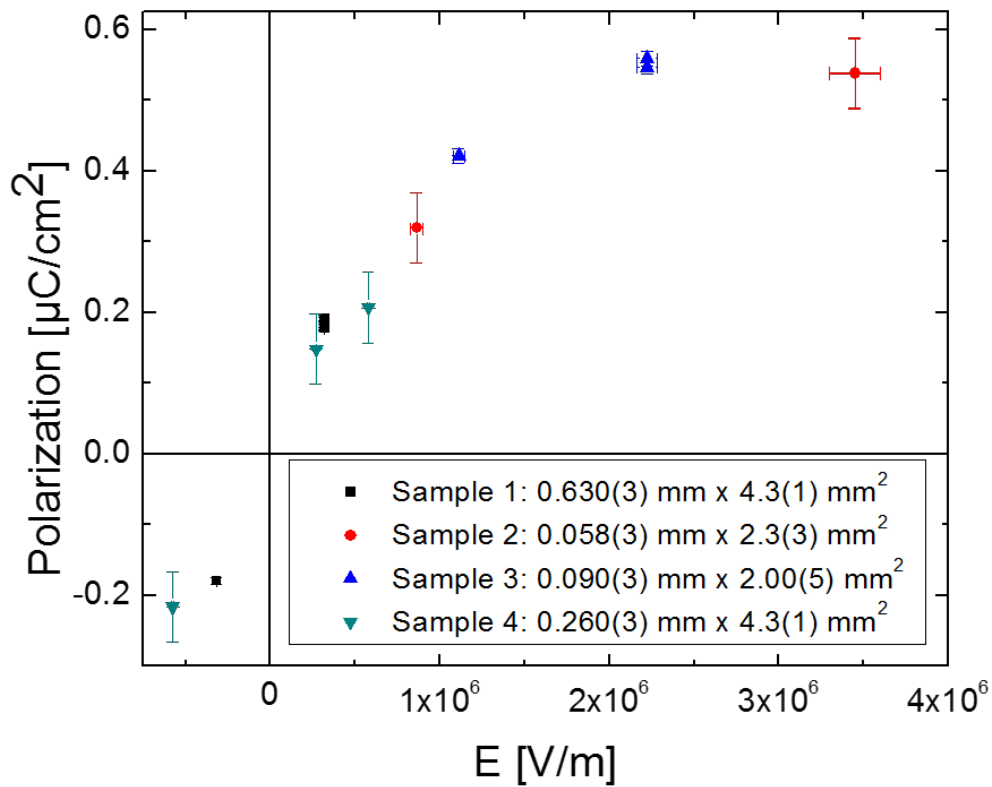


Figure 6.3: Low temperature (7 K) P -values obtained as a function of poling electric field E from pyroelectric measurements performed on four samples under various warming rate with a same temperature of poling $T_p = 100$ K.

tion measured with an applied field of 100 Oe and already reported in [108]. What is remarkable is that the two anomalies of C are located at the beginning and the end of the field-induced anomaly reported in M . On the other hand at $T_{N,B}$, the temperature of magnetic orientation of B -sites, there is no anomaly in C for all frequencies.

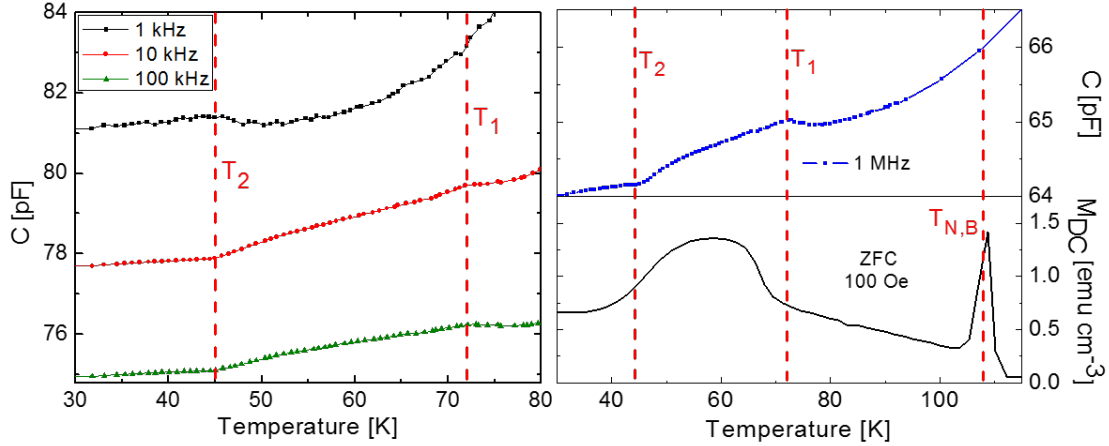


Figure 6.4: Capacitance vs temperature plot from impedance measurements performed with AC voltage of 200 mV with frequencies 1kHz, 10 kHz, 100 kHz and 1 MHz.

Transport properties The resistivity, $\rho(T)$, on $(\text{YMn}_3)\text{Mn}_4\text{O}_{12}$ polycrystalline disks contacted on both sides was investigated by the van der Pauw method and with the two points method. The measurements show the insulating behavior of $(\text{YMn}_3)\text{Mn}_4\text{O}_{12}$; with a room temperature value of 43 Ohm m (see Fig. 6.5) and the contribution of contacts to the total resistivity is negligible. In the 300-108 K range, the data follow a thermally activated behavior, as shown by the Arrhenius plot in the inset of the figure. With this analysis, we could find an activation energy $E_a=168$ meV, which confirms the insulating properties of $(\text{YMn}_3)\text{Mn}_4\text{O}_{12}$. At lower temperatures, the data deviate from the above Arrhenius-like trend but neither polarons thermally activated, nor variable range hopping at one, two or three dimensions can be identify preferentially to explain the low temperature data. No anomaly or discontinuity is found as a function of temperature.

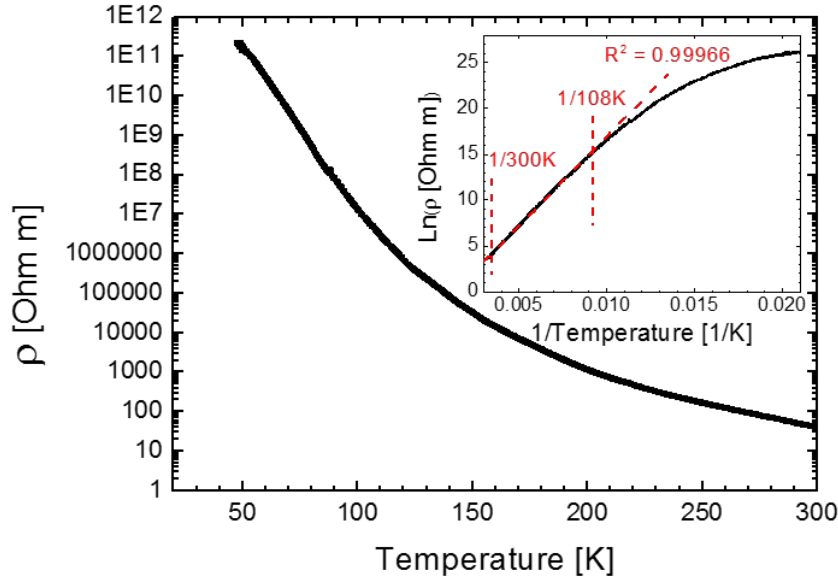


Figure 6.5: Electrical resistivity $\rho(T)$ of (YMn₃)Mn₄O₁₂. Inset: semilogarithmic $\ln(\rho)$ vs $1/T$ plot showing the thermally activated behavior predicted by the Arrhenius law. Dashed lines indicate the T range of the fit.

Synchrotron X-ray diffraction Because of the polar nature of the polarization vector, symmetry constraints impose to a ferroelectric phase to break the inversion center. From the neutron powder diffraction study reported in a recent work [108], we were not able to identify any symmetry lowering as a function of temperature and the data were refined in the centrosymmetric space group $I2/m$ from 300 K to 4 K. The discovery of ferroelectric properties in (YMn₃)Mn₄O₁₂ pushed us to perform further experiments in order to identify the expected loss of inversion center. In order to reach this purpose, we have performed X-ray synchrotron diffraction on a small (YMn₃)Mn₄O₁₂ single-crystal of few μm at room temperature and at 50 K. As we can see in Fig 6.6, additional reflections are visible at 50 K and 150 K, and can be explained by integrating the data with the cell-parameters $a' = 10.41 \text{ \AA}$, $b' = 14.58 \text{ \AA}$, $c' = 10.69 \text{ \AA}$ and $\beta' = 90.14^\circ$ which corresponds to a super-cell, commensurate with the high temperature one ($a = 7.44 \text{ \AA}$, $b = 7.33 \text{ \AA}$, $c = 7.44 \text{ \AA}$ and $\beta = 91.1566^\circ$). The super-cell is obtained from the high temperature unit cell by the following transformation $2\mathbf{b} \rightarrow \mathbf{b}'$; $(\mathbf{a} + \mathbf{c}) \rightarrow \mathbf{a}'$; $(\mathbf{c} - \mathbf{a}) \rightarrow \mathbf{c}'$ as represented in Fig. 6.7 and corresponding to a wavevector $k = (1/2, 1/2, -1/2)$.

A preliminar refinement has been performed in the super-cell and the space-group is found to be Ia at 50 and 150 K and the corresponding structure is represented in Fig. 6.6. The space-group is non-centrosymmetric and allows ferroelectricity. Results of a preliminar refinement of data at 50 K are reported in Table 6.2 but further improvements in the integration of saturated reflections needs to be done in order to improve the refinement and deduce accurate information on the distortion of the structure and on the direction of P .

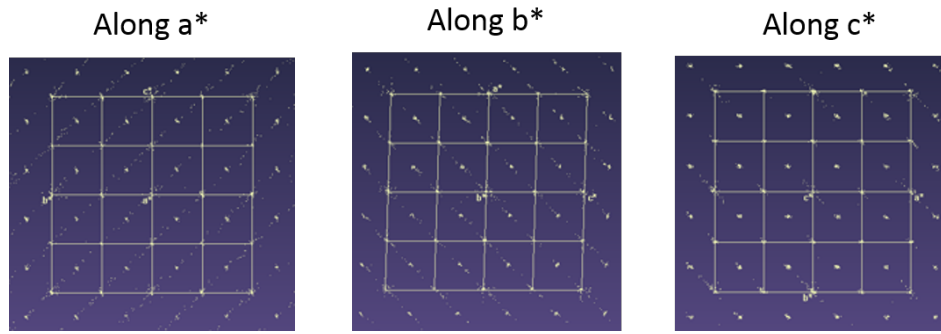


Figure 6.6: single-crystal diffraction patterns obtained at 50 K and integrated in the high-temperature (a,b,c) cell. Note the additive satellites peaks not explained by the high-temperature cell.

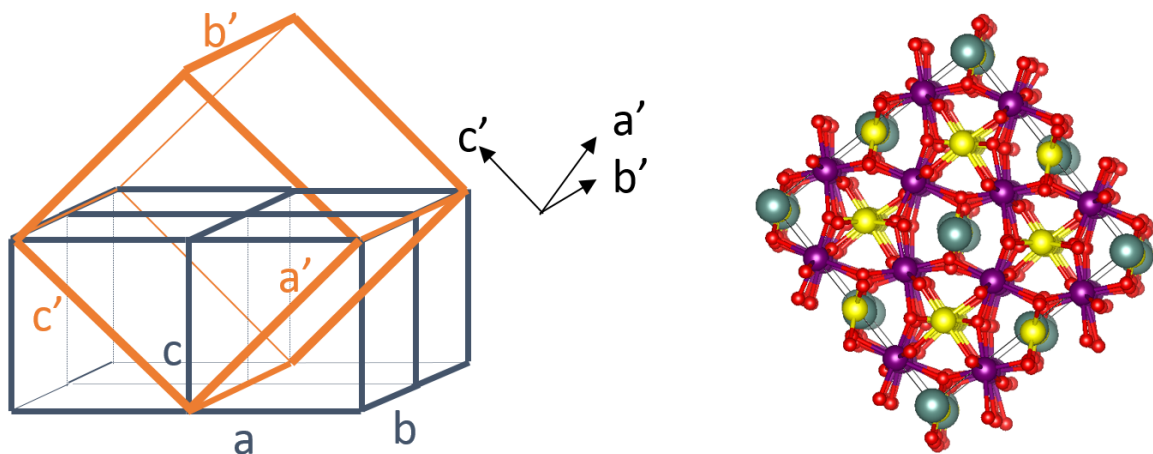


Figure 6.7: Left: Scheme of the super-cell in red with respect to the high-temperature cell in blue. Right: distorted crystal structure obtained from refinement of data in Ia at 50 K. Green: Y; Yellow: square-planar Mn; Purple: octahedral Mn. Red: O.

Empirical formula	Y₂Mn₁₄O₂₄
Formula weight	1330.98
Temperature	50 K
Crystal system	monoclinic
Space group	<i>Ia</i>
a'	10.4059(4) Å
b'	14.5762(6) Å
c'	10.6913(3) Å
α	90°
β'	90.137(3)°
γ	90°
Volume	1621.64(10) Å ³
Z	4
ρ _{calc}	5.452 g/cm ³
μ	15.305 mm ⁻¹
F(000)	2480.0
Crystal size	? × ? × ?
Radiation	18.46 keV (λ = 0.6717)
2θ range for data collection	4.466° to 49.64°
Index ranges	-12 ≤ h ≤ 12, -18 ≤ k ≤ 15, -13 ≤ l ≤ 13
Reflections collected	6504
Independent reflections	3066 [R _{int} = 0.0774, R _{sigma} = 0.0824]
Data/restraints/parameters	3066/2/362
Goodness-of-fit on F ²	1.760
Final R indexes [I ≥ 2σ (I)]	R ₁ = 0.1325, wR ₂ = 0.3670
Final R indexes [all data]	R ₁ = 0.1427, wR ₂ = 0.3935
Largest diff. peak/hole	3.87/-6.57 e Å ⁻³
Flack parameter	0.476(12)

Table 6.1: Single-crystal synchrotron data and structure refinement for (YMn₃)Mn₄O₁₂ at 50 K.

Atom	x	y	z	U(eq)
Y00	0.8159(4)	0.3659(4)	0.3828(6)	0.0123(14)
Mn1	0.3184(3)	0.5043(3)	0.6137(6)	0.0001(15)
Mn2	0.3180(4)	0.3768(5)	0.3669(4)	0.0001(15)
Mn3	0.5662(3)	-0.0002(4)	0.3665(3)	0.0004(17)
Mn4	0.5661(3)	0.2517(3)	0.3717(7)	0.0003(14)
Mn5	0.5657(4)	0.3727(5)	0.6186(7)	0.0015(14)
Mn6	0.8160(4)	0.31235(5)	0.63694(4)	0.0005(16)
Mn7	0.0659(3)	0.34986(4)	0.3650(4)	0.0007(17)
Mn8	0.3168(3)	0.2534(4)	0.6208(4)	0.0003(15)
Mn9	0.0681(4)	0.1245(5)	0.6222(7)	0.0001(13)
Mn10	0.0681(4)	0.3737(5)	0.6178(6)	0.0006(13)
Mn11	0.0696(3)	0.2481(3)	0.3731(7)	0.0009(14)
Mn12	0.3173(4)	0.0057(4)	0.6132(6)	0.0012(16)
Mn13	0.8163(3)	0.2433(4)	0.6238(4)	0.0003(14)
Mn14	0.0657(4)	-0.1213(5)	0.6186(7)	0.0003(14)
O00H	0.5460(20)	0.1247(14)	0.4310(20)	0.006(4)
O00I	0.0520(19)	0.3738(13)	0.4330(20)	0.004(4)
O00J	0.1540(20)	0.2273(14)	0.5540(20)	0.011(5)
O00K	0.9550(20)	0.1983(17)	0.7190(20)	0.017(5)
O00L	0.4610(20)	0.2938(15)	0.7170(20)	0.010(5)
O00M	0.3850(20)	0.6317(14)	0.6110(20)	0.007(4)
O00N	0.3830(20)	0.1322(15)	0.6190(20)	0.006(4)
O00O	0.2350(20)	0.2681(14)	0.3050(20)	0.010(5)
O00P	0.7260(20)	0.2264(13)	0.2940(20)	0.005(4)
O00Q	0.6650(20)	0.2803(15)	0.5400(20)	0.007(4)
O00R	0.7210(20)	0.0337(15)	0.2820(20)	0.011(5)
O00S	0.4670(20)	0.4661(16)	0.6940(30)	0.024(7)
O00T	0.2535(19)	0.3797(14)	0.6210(20)	0.003(4)
O00U	0.2110(20)	0.4549(16)	0.2740(20)	0.018(5)
O00V	0.4210(20)	0.2926(17)	0.4580(30)	0.021(6)
O00W	0.9120(20)	0.2177(15)	0.4480(30)	0.015(5)
O00X	0.4730(20)	-0.0229(17)	0.6840(30)	0.026(6)
O00Y	0.2500(20)	-0.1175(16)	0.6070(30)	0.015(5)
O00Z	0.0520(19)	0.3738(13)	0.4330(20)	0.004(4)
O010	0.4010(20)	0.4815(17)	0.4260(30)	0.021(6)
O2	0.6710(20)	0.4537(15)	0.5240(30)	0.014(5)
O3	0.1740(20)	0.0500(16)	0.5160(30)	0.029(8)
O0AA	0.0830(20)	-0.1245(13)	0.7950(20)	0.003(4)
Y0A	0.3177(4)	0.1189(4)	0.3540(6)	0.0189(19)

Table 6.2: Fractional atomic coordinates and equivalent isotropic displacement parameters, U_{eq} , obtained from the refinement of the single-crystal synchrotron diffraction data. U_{eq} is defined as 1/3 of the trace of the orthogonalized U_{ij} tensor.

IV. DISCUSSION AND CONCLUSION

The pyrocurrent curves reported in this work present two peaks as a function of temperature, both corresponding to an anomaly of the capacitance at $T_2 = 45$ K and $T_1 = 72$ K. It is quite remarkable that these two temperatures correspond to the beginning and the end of the magnetic field-induced anomaly identified in a previous work [108] and reported in Fig. 6.4. This result supports the scenario of a magnetic ferroelectricity in (YMn₃)Mn₄O₁₂. Very surprisingly, no long-range magnetic order of A' -sites corresponds to the magnetic anomaly and, to the best of our knowledge, this is the first time that such a phenomena is reported in a ferroelectric compound. From literature, we found that magnetic frustration can prevent for long-range magnetic orders like in spin-glass or spin-liquids [112, 113]. However, in spin-frustrated magnets like RMn₂O₅ (R=Tb, Ho, Dt) ferroelectric distortions are known to release the geometric magnetic frustration and thus tend to stabilize a long-range magnetic order [11, 31, 33]. Besides, (YMn₃)Mn₄O₁₂ loses its inversion center with the occurrence of the supercell at 200 K, as evidenced by the synchrotron data that could be refined in the Ia polar group at 50 and 150 K. In parent compounds like TbMnO₃ and (CaMn₃)Mn₄O₁₂, modulation of ionic positions of the order 10^{-15} m were reported by means of x-ray synchrotron diffraction without clear loss of inversion center [87, 86, 67] and for frustrated ferroelectrics, even x-ray synchrotron diffraction failed to evidence the expected symmetry lowering [66]. Thus, the case of (YMn₃)Mn₄O₁₂ is unique and needs further investigations in order to understand if local magnetic interactions (fluctuations) with $\langle M \rangle = 0$ can stabilize a non-zero macroscopic polarization ($\langle P \rangle \neq 0$) in the non-centrosymmetric structure (space group Ia).

In conclusion, we have found that the new quadruple perovskite (YMn₃)Mn₄O₁₂ exhibits a large polarization of $0.54 \mu\text{C cm}^{-2}$ occurring below $T_1 = 72$ K corresponding to the beginning of the anomaly in the magnetization. From pyroelectric current and capacitance measurements, we found that the ferroelectric phase presents also a second critical temperature at $T_2 = 45$ K corresponding to the end of the magnetic anomaly. By means of synchrotron X-ray diffraction, we were able to identify the structural transition leading to the polar space-group Ia which allows ferroelectricity. This transition is characterized by the establishment of a super-cell commensurate with the high-

temperature one and occurs at $T_s = 200$ K, 128 K above the ferroelectric transition. This scenario needs an extensive investigation of the particular distortion occurring at 200 K and the determination of the local magnetic interactions by means of RMN measurements. If such a scenario were confirmed, $(\text{YMn}_3)\text{Mn}_4\text{O}_{12}$ would be a suitable candidate for multiferroic applications as they require high P -value and strong coupling between P and M .

Conclusions and perspectives

In the present Thesis, we have addressed the open issue of the origin of the unusually large magnetic ferroelectricity observed in the quadruple perovskite (AMn₃)Mn₄O₁₂. Previous results were obtained on (CaMn₃)Mn₄O₁₂, which displays a complex incommensurate magnetic ordering combined with mixed-valence (Mn³⁺/Mn⁴⁺) properties. This complexity has hindered to establish a clear correlation between the magnetic ordering and the electric polarization, hence the microscopic mechanism remains controversial. In view of this difficulty, our research has been focused on two related compounds, (LaMn₃)Mn₄O₁₂ (LMO) and (YMn₃)Mn₄O₁₂ (YMO), with much simpler magnetic orderings and with simple single-valence Mn³⁺ properties. Specifically, the magnetic structures of these compounds are commensurate, so the analysis of the separate contributions of antisymmetric and exchange interactions is possible. Moreover, the isovalent La/Y chemical substitution allowed us to single out the effect of chemical pressure on the magnetic structures and on the multiferroic properties, which gives a hint as the structural and electronic properties relevant to magnetic ferroelectricity in the (AMn₃)Mn₄O₁₂ family. Below, we summarize the specific results of our research which has been conducted in collaboration with several groups (see acknowledgment section), based on the a wide range of experimental methods including high-pressure synthesis, x-ray and neutron diffraction, thermodynamic, magnetic and transport measurements, and infrared and Raman spectroscopies.

- In polycrystalline LMO samples, we have found a very high P -value of $0.54 \mu\text{C cm}^{-2}$ induced by the the C -type magnetic ordering of the Mn³⁺ B sites at $T_{N,B}=78$ K. To the best of our knowledge, this is the highest value hitherto reported in magnetic ferroelectrics even considering that the second highest value of $0.27 \mu\text{C cm}^{-2}$ previously reported in (CaMn₃)Mn₄O₁₂ was obtained in single crystals. The present result is very promising for multiferroic applications as 6-10 times larger values are typically expected in single crystals or thin films [64].
- In LMO, our measurement of the temperature dependence of the unit cell parameters gives evidence of a large magnetostriction along the ac -diagonal, suggesting that the polarization lies along this direction.

- The above result combined with the symmetry properties of the C -type structure is consistent with a dominant contribution of the exchange-striction to the ferroelectricity, consistent with the fact that this mechanism is required to induce large spontaneous polarizations.
- Similar to the case of previously reported perovskitelike magnetic ferroelectrics, such as $(\text{CaMn}_3)\text{Mn}_4\text{O}_{12}$ or ReMnO_3 , we found no evidence of inversion symmetry breaking in the ferroelectric phase of LMO below $T_{N,B}$ since synchrotron diffraction, Raman and IR data are consistent with the centrosymmetric $I2/m$ structure down to 50 K.
- In order to investigate the effect of chemical pressure on the above multiferroic properties of LMO, we have succeeded in the reproducible synthesis of $(\text{YMn}_3)\text{Mn}_4\text{O}_{12}$ (YMO) under high pressure at 9 GPa. To the best of our knowledge, this is a new compound where chemical pressure is exerted by the isovalent substitution of La^{3+} with Y^{3+} on the A -sites.
- As expected, the above substitution leads to a significant shrinking of the $I2/m$ unit cell, which explains a significant 30 K enhancement of the B -site ordering temperature up to $T_{N,B} = 108$ K.
- On the other hand, YMO is found to display unexpected features not found in any other $(\text{AMn}_3)\text{Mn}_4\text{O}_{12}$ compounds, namely a structural phase transition at $T_s = 200$ K associated with a commensurate structural modulation described by a $(1/2\ 1/2\ -1/2)$ propagation vector. A preliminary structural refinement also suggests a noncentrosymmetric Ia space group consistent with the appearance of ferroelectricity (see below). Furthermore, three independent measurements, i.e. magnetization, specific heat and powder neutron diffraction, give evidence of no long-range order of the A' sites at low temperature, contrary to the case of LMO and of all other $(\text{AMn}_3)\text{Mn}_4\text{O}_{12}$ compounds.
- On the other hand, a pronounced anomaly in the magnetization is observed at $T^* = 70$ K, which is the temperature range where the A' sites ordering is typically

found in other (AMn₃)Mn₄O₁₂ compounds, upon application of an arbitrarily weak field, which suggests a latent magnetic ordering.

- Interestingly, in YMO, a spontaneous electric polarization is observed at T^* , which suggests a surprising scenario of ferroelectricity driven by magnetism even in the absence of long range order.
- Within the experimental error, the value of spontaneous polarization measured in YMO turns out to be identical ($0.54 \mu\text{C cm}^{-2}$) to that found in LMO (see above). Given the close similarity of structural and electronic properties of the two compounds LMO and YMO, this would not be surprising. On the other hand, by considering the completely different magnetic characteristics of the two compounds, a different ferroelectric behavior would be expected within a scenario of magnetic ferroelectricity.

The above results respond to some of the open questions raised at the beginning of the present Thesis:

- The finding of large polarizations in both, LMO and YMO, twice as large as that previously found in (CaMn₃)Mn₄O₁₂ seems to support the idea that ferroelectricity in the $\mu\text{C cm}^{-2}$ range is a common feature of the (AMn₃)Mn₄O₁₂.
- The above result has been obtained in single-valent Mn³⁺ systems, which indicates that charge ordering is not required to achieve such a large values of polarization.
- The above conclusion that exchange-striction is the dominant mechanism of magnetic ferroelectricity in LMO confirms that this mechanism is more promising than the antisymmetric exchange interaction to achieve large magnetic ferroelectricity.

In addition, we believe that the present work may clarify some controversial issues and raises new questions that may be the object of further work:

1. The present diffraction, Raman and IR study give no indication of inversion symmetry breaking in unpoled LMO samples, consistent with similar observations in other magnetic ferroelectrics. This apparent inconsistency with the definition of

ferroelectric order may be explained by a picture of ferroelectric domains whose size is smaller than the spatial resolution of the above experimental probes (~ 100 nm in the case of x-ray diffraction). Indeed, the average polarization of a sufficiently large number of domains would be zero in the absence of poling field. This picture is consistent with the prediction by Levanyuk and Sannikov of degenerate solutions for the multi-component order parameter necessarily leads to the formation of domains with different values and different orientations of spontaneous polarization. We envisage that the validity of this hypothesis could be verified by means of experimental probes with improved spatial resolution, such as Coherent Anti-Stokes Raman (CARS) spectroscopy.

2. In YMO, the unexpected observation of ferroelectric order in the absence of long-range magnetic order of the A' -sites (or of any other type of long range order) raises a similar question as above as to the minimum size of magnetic domains required to induce a polarization of the lattice. In the case of YMO, we put forward the hypothesis that the polar distortion of the crystal structure occurring at T_s may force the alignment of ferroelectric domains that would be otherwise randomly oriented because of the random orientation of the magnetic domains.
3. In order to investigate the origin of the anomalous magnetic response at T^* , that may explain the absence of long-range order of the A' sites, we envisage that a combines study of inelastic neutron scattering (INS) and of NMR spectroscopy may unveil the spin dynamics and the range of the magnetic correlations involving these sites. This would give a hint as to the possible role of small magnetic domains in the formation of a macroscopic polarization stabilized by a polar crystal structure. The proposed study would require the synthesis of sufficiently large single crystals for INS experiments. This appears to be very challenging owing to the extreme conditions required to form the YMO phase.
4. Further low-temperature x-ray diffraction studies are required to establish a precise structural model of the structural modulation occurring at T_s , which is required to determine the orientation of the ferroelectric polarization.
5. The growth of larger crystals of both LMO and YMO would enable not only the

above INS study but also the direct measurement of the polarization direction. This measurement is required to confirm the preliminary indication of polarization along the *ac*-direction in LMO and to unveil the polarization direction in YMO, which remains to be determined.

6. The availability of larger crystals (or of epitaxial thin films) may also confirm the expectation of significantly larger polarizations with respect to the values $\sim 1\mu\text{C cm}^{-2}$ measured in polycrystalline samples. By taking into account previous studies [64], we expect 6-10 times larger values, which would definitely be very promising for practical applications.

Bibliography

- [1] M. P. Curie, “Phénomènes physiques: les considérations sur la symétrie familières aux cristallographes.,” *Journal de physique théorique et appliquée*, vol. 3, no. 1, pp. 393–415, 1894.
- [2] D. N. Astrov, “The magnetoelectric effect in antiferromagnetics,” *Sov. JETP*, vol. 11, no. 3, pp. 708–709, 1960.
- [3] I. Dzyaloshinsky, “On the magneto-electrical effect in antiferromagnets,” *Sov. JETP*, vol. 37, pp. 628–629, 1960.
- [4] L. Landau and E. Lifshitz, *Electrodynamics of Continuous Media (vol 8)*.
- [5] H. Schmid, “Multi-ferroic magnetoelectrics,” *Ferroelectrics*, vol. 162, pp. 317–338, 1994.
- [6] N. A. Hill, “Why Are There so Few Magnetic Ferroelectrics?,” *The Journal of Physical Chemistry B*, vol. 104, pp. 6694–6709, July 2000.
- [7] K. Wang, J.-M. Liu, and Z. Ren, “Multiferroicity: the coupling between magnetic and polarization orders,” *Advances in Physics*, vol. 58, pp. 321–448, July 2009.
- [8] J. Wang, J. B. Neaton, H. Zheng, V. Nagarajan, S. B. Ogale, B. Liu, D. Viehland, V. Vaithyanathan, D. G. Schlom, U. V. Waghmare, N. A. Spaldin, K. M. Rabe, M. Wuttig, and R. Ramesh, “Epitaxial BiFeO₃ multiferroic thin film heterostructures,” *Science*, vol. 299, pp. 1719–1722, 2003.
- [9] T. Choi, S. Lee, Y. J. CHoi, V. Kiryukhin, and S.-W. Cheong, “Switchable ferroelectric diode and photovoltaic effect in BiFeO₃,” *Science*, vol. 324, no. 5923, pp. 63–66, 2009.

- [10] T. Kimura, T. Goto, H. Shintani, K. Ishizaka, T. Arima, and Y. Tokura, “Magnetic control of ferroelectric polarization,” *Nature*, vol. 426, pp. 55–58, Nov. 2003.
- [11] N. Hur, S. Park, P. Sharma, A. Ahn, S. Guha, and S.-W. Cheong, “Electric polarization reversal and memory in a multiferroic material induced by magnetic fields,” *Nature*, vol. 429, pp. 392–395, 2004.
- [12] D. Khomskii, “Classifying multiferroics: Mechanisms and effects,” *Physics*, vol. 2, Mar. 2009.
- [13] A. P. Levanyuk and D. G. Sannikov, “Improper ferroelectrics,” *Soviet Physics Uspekhi*, vol. 17, no. 2, p. 199, 1974.
- [14] S.-W. Cheong and M. Mostovoy, “Multiferroics: a magnetic twist for ferroelectricity,” *Nature Materials*, vol. 6, pp. 13–20, Jan. 2007.
- [15] N. Ikeda, H. Ohsumi, K. Ohwada, K. Ishii, T. Inami, K. Kakurai, Y. Murakami, K. Yoshii, S. Mori, Y. Horibe, and H. Kitô, “Ferroelectricity from iron valence ordering in the charge-frustrated system LuFe_2O_4 ,” *Nature*, vol. 436, pp. 1136–1138, Aug. 2005.
- [16] J. van der Brink and D. I. Khomskii, “Multiferroicity due to charge ordering,” *Journal of Physics: Condensed Matter*, vol. 20, no. 43, p. 434217, 2008.
- [17] K. Yamauchi and P. Barone, “Electronic ferroelectricity induced by charge and orbital orderings,” *Journal of Physics: Condensed Matter*, vol. 26, no. 10, p. 103201, 2014.
- [18] Y. J. Choi, H. T. Yi, S. Lee, Q. Huang, V. Kiryukhin, and S.-W. Cheong, “Ferroelectricity in an Ising Chain Magnet,” *Physical Review Letters*, vol. 100, p. 047601, Jan. 2008.
- [19] L. Landau and E. Lifshitz, *Statistical physics (vol 5)*.
- [20] S. Goshen, D. Mukamel, H. Shaked, and S. Shtrikman, “Mechanism leading to ferroelectricity induced in centrosymmetric crystals by antiferromagnetic transitions,” *Physical Review B*, vol. 2, no. 11, p. 4679, 1970.

- [21] M. Mostovoy, “Ferroelectricity in Spiral Magnets,” *Physical Review Letters*, vol. 96, p. 067601, Feb. 2006.
- [22] M. Kenzelmann, A. B. Harris, S. Jonas, C. Broholm, J. Schefer, S. B. Kim, C. L. Zhang, S.-W. Cheong, O. P. Vajk, and J. W. Lynn, “Magnetic Inversion Symmetry Breaking and Ferroelectricity in TbMnO_3 ,” *Physical Review Letters*, vol. 95, p. 087206, Aug. 2005.
- [23] G. Lawes, A. B. Harris, T. Kimura, N. Rogado, R. J. Cava, A. Aharony, O. Entin-Wohlman, T. Yildirim, M. Kenzelmann, C. Broholm, and A. P. Ramirez, “Magnetically Driven Ferroelectric Order in $\text{Ni}_3\text{V}_2\text{O}_8$,” *Physical Review Letters*, vol. 95, p. 087205, Aug. 2005.
- [24] I. Dzyaloshinsky, “A thermodynamic theory of “weak” ferromagnetism of antiferromagnetics,” *Journal of Physics and Chemistry of Solids*, vol. 4, no. 4, pp. 241–255, 1958.
- [25] T. Moriya, “Anisotropic Superexchange Interaction and Weak Ferromagnetism,” *Physical Review*, vol. 120, pp. 91–98, Oct. 1960.
- [26] H. Katsura, N. Nagaosa, and A. V. Balatsky, “Spin Current and Magnetoelectric Effect in Noncollinear Magnets,” *Physical Review Letters*, vol. 95, p. 057205, July 2005.
- [27] P. Bruno and V. K. Dugaev, “Equilibrium spin currents and the magnetoelectric effect in magnetic nanostructures,” *Physical Review B*, vol. 72, p. 241302, Dec. 2005.
- [28] H. Katsura, A. V. Balatsky, and N. Nagaosa, “Dynamical Magnetoelectric Coupling in Helical Magnets,” *Physical Review Letters*, vol. 98, p. 027203, Jan. 2007.
- [29] I. A. Sergienko and E. Dagotto, “Role of the Dzyaloshinskii-Moriya interaction in multiferroic perovskites,” *Physical Review B*, vol. 73, p. 094434, Mar. 2006.
- [30] M. Mochizuki, N. Furukawa, and N. Nagaosa, “Theory of spin-phonon coupling in multiferroic manganese perovskites RMnO_3 ,” *Physical Review B*, vol. 84, p. 144409, Oct. 2011.

- [31] G. R. Blake, L. C. Chapon, P. G. Radaelli, S. Park, N. Hur, S.-W. Cheong, and J. Rodríguez-Carvajal, “Spin structure and magnetic frustration in multiferroic RMn_2O_5 ($\text{R} = \text{Tb}, \text{Ho}, \text{Dy}$),” *Physical Review B*, vol. 71, p. 214402, June 2005.
- [32] L. C. Chapon, G. R. Blake, M. J. Gutmann, S. Park, N. Hur, P. G. Radaelli, and S.-W. Cheong, “Structural Anomalies and Multiferroic Behavior in Magnetically Frustrated TbMn_2O_5 ,” *Physical Review Letters*, vol. 93, p. 177402, Oct. 2004.
- [33] X. Fabreges, S. Petit, I. Mirebeau, S. Pailhes, L. Pinsard, A. Forget, M. T. Fernandez-Diaz, and F. Porcher, “Spin-Lattice Coupling, Frustration, and Magnetic Order in Multiferroic RMnO_3 ,” *Physical Review Letters*, vol. 103, p. 067204, Aug. 2009.
- [34] S. Picozzi, K. Yamauchi, B. Sanyal, I. A. Sergienko, and E. Dagotto, “Dual Nature of Improper Ferroelectricity in a Magnetoelectric Multiferroic,” *Physical Review Letters*, vol. 99, p. 227201, Nov. 2007.
- [35] A. Muñoz, M. T. Casáis, J. A. Alonso, M. J. Martínez-Lope, J. L. Martínez, and M. T. Fernández-Díaz, “Complex Magnetism and Magnetic Structures of the Metastable HoMnO_3 Perovskite,” *Inorganic Chemistry*, vol. 40, pp. 1020–1028, Feb. 2001.
- [36] I. A. Sergienko, C. Şen, and E. Dagotto, “Ferroelectricity in the Magnetic E - Phase of Orthorhombic Perovskites,” *Physical Review Letters*, vol. 97, p. 227204, Nov. 2006.
- [37] B. Lorenz, Y.-Q. Wang, and C.-W. Chu, “Ferroelectricity in perovskite HoMnO_3 and YMnO_3 ,” *Physical Review B*, vol. 76, p. 104405, Sept. 2007.
- [38] N. Lee, Y. J. Choi, M. Ramazanoglu, W. Ratcliff, V. Kiryukhin, and S.-W. Cheong, “Mechanism of exchange striction of ferroelectricity in multiferroic orthorhombic HoMnO_3 single crystals,” *Physical Review B*, vol. 84, p. 020101, July 2011.

- [39] M. Nakamura, Y. Tokunaga, M. Kawasaki, and Y. Tokura, "Multiferroicity in an orthorhombic YMnO_3 single-crystal film," *Applied Physics Letters*, vol. 98, no. 8, p. 082902, 2011.
- [40] G. Zhang, S. Dong, Z. Yan, Y. Guo, Q. Zhang, S. Yunoki, E. Dagotto, and J.-M. Liu, "Multiferroic properties of $\text{CaMn}_7\text{O}_{12}$," *Physical Review B*, vol. 84, p. 174413, Nov. 2011.
- [41] R. D. Johnson, L. C. Chapon, D. D. Khalyavin, P. Manuel, P. G. Radaelli, and C. Martin, "Giant Improper Ferroelectricity in the Ferroaxial Magnet $\text{CaMn}_7\text{O}_{12}$," *Physical Review Letters*, vol. 108, p. 067201, Feb. 2012.
- [42] M. Marezio, D. Dernier, J. Chenavas, and J.-C. Joubert, "High Pressure Synthesis and Crystal Structure of $\text{NaMn}_7\text{O}_{12}$," *Journal of Solid State Chemistry*, vol. 6, pp. 16–20, 1973.
- [43] A. Deschanvres, B. Raveau, and F. Tollemer *Bull. Soc. Chim. Fr.*, no. 11, p. 4077, 1967.
- [44] B. Bochu, J. Chenavas, J. C. Joubert, and M. Marezio, "High pressure synthesis and crystal structure of a new series of perovskite-like compounds $\text{CMn}_7\text{O}_{12}$ (C = Na, Ca, Cd, Sr, La, Nd)," *Journal of Solid State Chemistry*, vol. 11, pp. 88–93, Oct. 1974.
- [45] J. B. Goodenough, "Theory of the Role of Covalence in the Perovskites-Type Manganites $[\text{La},\text{M}(\text{II})]\text{MO}_3$," *Physical Review*, vol. 100, pp. 564–573, Oct. 1955.
- [46] A. Prodi, E. Gilioli, R. Cabassi, F. Bolzoni, F. Licci, Q. Huang, J. W. Lynn, M. Affronte, A. Gauzzi, and M. Marezio, "Magnetic structure of the high-density single-valent eg Jahn-Teller system $\text{LaMn}_7\text{O}_{12}$," *Physical Review B*, vol. 79, p. 085105, Feb. 2009.
- [47] A. Prodi, E. Gilioli, A. Gauzzi, F. Licci, M. Marezio, F. Bolzoni, Q. Huang, A. Santoro, and J. W. Lynn, "Charge, orbital and spin ordering phenomena in the mixed valence manganite $(\text{NaMn}_3^{3+})(\text{Mn}_2^{3+}\text{Mn}_2^{4+})\text{O}_{12}$," *Nature Materials*, vol. 3, pp. 48–52, Jan. 2004.

- [48] R. D. Johnson, D. D. Khalyavin, P. Manuel, A. Bombardi, C. Martin, L. C. Chapon, and P. G. Radaelli, “Modulated spin helicity stabilized by incommensurate orbital density waves in a quadruple perovskite manganite,” *Physical Review B*, vol. 93, p. 180403, May 2016.
- [49] X. Z. Lu, M.-H. Whangbo, S. Dong, X. G. Gong, and H. J. Xiang, “Giant Ferroelectric Polarization of $\text{CaMn}_7\text{O}_{12}$ Induced by a Combined Effect of Dzyaloshinskii-Moriya Interaction and Exchange Striction,” *Physical Review Letters*, vol. 108, p. 187204, May 2012.
- [50] A. Jayaraman, P. Dernier, and L. D. Longinotti, “Study of the valence transition in SmS induced by alloying, temperature, and pressure,” *Physical Review B*, vol. 11, no. 8, p. 2783, 1975.
- [51] J. Wittig *Physical Review Letters*, vol. 21, no. 17, p. 1250, 1968.
- [52] D. Walker, M. Carpentier, and C. M. Hitch, “Some simplifications to multianvil devices for high pressure experiments,” *American Mineralogist*, vol. 75, pp. 1020–1028, 1990.
- [53] E. Gilioli, G. Calestani, F. Licci, C. Paorici, A. Gauzzi, F. Bolzoni, and A. Prodi, “High-pressure growth of $\text{NaMn}_7\text{O}_{12}$ crystals,” *Journal of Solid State Chemistry*, vol. 179, pp. 3839–3848, Dec. 2006.
- [54] E. Gilioli, G. Calestani, F. Licci, A. Gauzzi, F. Bolzoni, A. Prodi, and M. Marezio, “P–T phase diagram and single crystal structural refinement of $\text{NaMn}_7\text{O}_{12}$,” *Solid State Sciences*, vol. 7, pp. 746–752, June 2005.
- [55] J. Rodriguez-Carvajal, “Fullprof suite,” *Physica B*, vol. 192, no. 55, 1993.
- [56] H. M. Rietveld, “A profile refinement method for nuclear and magnetic structures,” *Journal of applied Crystallography*, vol. 2, pp. 65–71, 1969.
- [57] L. Chapon, “An introduction to the use of representation analysis for studying magnetoelectrics and multiferroics,” *EPJ Web of Conferences*, vol. 22, p. 00013, 2012.

- [58] L. J. van der Pauw, “A method of measuring specific resistivity and hall effect of discs of arbitrary shape,” *Philips Research Report*, vol. 13, no. 1, pp. 1–9, 1958.
- [59] C. C. Homes, M. Reedyk, D. A. Cradles, and T. Timusk, “Technique for measuring the reflectance of irregular, submillimeter-sized samples,” *Applied Optics*, vol. 32, no. 16, pp. 2976–2983, 1993.
- [60] W. Eerenstein, N. D. Mathur, and J. F. Scott, “Multiferroic and magnetoelectric materials,” *Nature*, vol. 442, pp. 759–765, Aug. 2006.
- [61] T. Aoyama, K. Yamauchi, A. Iyama, S. Picozzi, K. Shimizu, and T. Kimura, “Giant spin-driven ferroelectric polarization in TbMnO₃ under high pressure,” *Nature Communications*, vol. 5, p. 4927, Sept. 2014.
- [62] J. Zhang, X. Lu, J. Zhou, H. Sun, F. Huang, and J. Zhu, “Magnetic properties and origins of ferroelectric polarization in multiferroic CaMn₇O₁₂,” *Physical Review B*, vol. 87, p. 075127, Feb. 2013.
- [63] H. Okamoto, M. Karppinen, H. Yamauchi, and H. Fjellvåg, “High-temperature synchrotron X-ray diffraction study of LaMn₇O₁₂,” *Solid State Sciences*, vol. 11, pp. 1211–1215, July 2009.
- [64] S. Ishiwata, Y. Kaneko, Y. Tokunaga, Y. Taguchi, T.-h. Arima, and Y. Tokura, “Perovskite manganites hosting versatile multiferroic phases with symmetric and antisymmetric exchange strictions,” *Physical Review B*, vol. 81, p. 100411, Mar. 2010.
- [65] F. Mezzadri, G. Calestani, M. Calicchio, E. Gilioli, F. Bolzoni, R. Cabassi, M. Marezio, and A. Migliori, “Synthesis and characterization of multiferroic BiMn₇O₁₂,” *Physical Review B*, vol. 79, p. 100106, Mar. 2009.
- [66] S. Matsumoto, M. Tanaka, I. Kagomiya, K. Kohn, and S. Nakamura, “Mössbauer spectrum and spin structure of weakly ferroelectric YMn₂O₅ and HoMn₂O₅,” *Ferroelectrics*, vol. 286, pp. 185–195, 2003.

- [67] H. C. Walker, F. Fabrizi, L. Paolasini, F. de Bergevin, J. Herrero-Martin, A. T. Boothroyd, D. Prabhakaran, and D. F. McMorrow, “Femtosecond magnetically induced lattice distortions in multiferroic TbMnO₃,” *Science*, vol. 333, no. 6047, pp. 1273–1276, 2011.
- [68] A. Gauzzi, G. Rousse, F. Mezzadri, G. L. Calestani, G. Andre, F. Bouree, M. Calicchio, E. Gilioli, R. Cabassi, F. Bolzoni, and others, “Magnetoelectric coupling driven by inverse magnetostriction in multiferroic BiMn₃Mn₄O₁₂,” *Journal of Applied Physics*, vol. 113, no. 4, pp. 043920–043920, 2013.
- [69] V. L. Indenbom *Sov. Phys. Crystallogr.*, vol. 5, p. 106, 1960.
- [70] A. P. Levanyuk and D. G. Sannikov *Sov. Phys. JETP*, vol. 28, p. 134, 1969.
- [71] V. Dvořák *Phys. Stat. Sol. (b)*, vol. 45, p. 147, 1971.
- [72] A. P. levanyuk and D. G. Sannikov *Sov. Phys. Solid State*, vol. 12, p. 2418, 1971.
- [73] M. Fiebig, T. Lottermother, D. Fröhlich, A. Goltsev, and R. Pisarev, “Observation of coupled magnetic and electric domains,” *Nature*, vol. 419, pp. 818–820, Oct. 2002.
- [74] T. Lottermother, T. Lonkai, U. Amann, D. Hohlwein, J. Ihringer, and M. Fiebig, “Magnetic phase control by an electric field,” *Nature*, vol. 430, pp. 541–544, July 2004.
- [75] M. Fiebig, “Revival of the magnetoelectric effect,” *Journal of Physics D: Applied Physics*, vol. 38, pp. R123–R152, Apr. 2005.
- [76] S. Lee, A. Pirogov, M. Kang, K.-H. Jang, M. Yonemura, T. Kamiyama, S.-W. Cheong, F. Gozzo, N. Shin, H. Kimura, Y. Noda, and J.-G. Park, “Giant magneto-elastic coupling in multiferroic hexagonal manganites,” *Nature*, vol. 451, pp. 805–808, Feb. 2008.
- [77] K. Ramesha, A. Llobet, T. Proffen, C. R. Serrao, and C. N. R. Rao, “Observation of local non-centrosymmetry in weakly biferroic YCrO₃,” *Journal of Physics: Condensed Matter*, vol. 19, p. 102202, Mar. 2007.

- [78] S. H. Chun, Y. S. Chai, B.-G. Jeon, H. J. Kim, Y. S. Oh, I. Kim, H. Kim, B. J. Jeon, S. Y. Haam, J.-Y. Park, S. H. Lee, J.-H. Chung, J.-H. Park, and K. H. Kim, “Electric Field Control of Nonvolatile Four-State Magnetization at Room Temperature,” *Physical Review Letters*, vol. 108, Apr. 2012.
- [79] J. Laverdière, S. Jandl, A. A. Mukhin, V. Y. Ivanov, V. G. Ivanov, and M. N. Iliev, “Spin-phonon coupling in orthorhombic RMnO_3 ($R = \text{Pr, Nd, Sm, Eu, Gd, Tb, Dy, Ho, Y}$): A Raman study,” *Physical Review B*, vol. 73, no. 21, p. 214301, 2006.
- [80] J. Vermette, S. Jandl, and M. M. Gospodinov, “Raman study of spin–phonon coupling in ErMnO_3 ,” *Journal of Physics: Condensed Matter*, vol. 20, p. 425219, Oct. 2008.
- [81] R. Schleck, R. L. Moreira, H. Sakata, and R. P. S. M. Lobo, “Infrared reflectivity of the phonon spectra in multiferroic TbMnO_3 ,” *Physical Review B*, vol. 82, p. 144309, Oct. 2010.
- [82] D. J. Lockwood and M. G. Cottam, “The spin-phonon interaction in FeF_2 and MnF_2 studied by Raman spectroscopy,” *Journal of Applied Physics*, vol. 64, no. 10, p. 5876, 1988.
- [83] R. Schleck, Y. Nahas, R. P. S. M. Lobo, J. Varignon, M. B. Lepetit, C. S. Nelson, and R. L. Moreira, “Elastic and magnetic effects on the infrared phonon spectra of MnF_2 ,” *Physical Review B*, vol. 82, p. 054412, Aug. 2010.
- [84] W. Baltensperger and J. Helman, “Influence of magnetic order in insulators on the optical phonon frequency,” *Helvetica Physica Acta*, vol. 41, pp. 668–673, 1968.
- [85] E. Granado, A. García, J. A. Sanjurjo, C. Rettori, I. Torriani, F. Prado, R. D. Sánchez, A. Caneiro, and S. B. Oseroff, “Magnetic ordering effects in the Raman spectra of $\text{La}_{1-x}\text{Mn}_{1-x}\text{O}_3$,” *Physical Review B*, vol. 60, pp. 11879–11882, Nov. 1999.
- [86] H. C. Walker, F. Fabrizi, L. Paolasini, F. de Bergevin, D. Prabhakaran, A. T. Boothroyd, and D. F. McMorrow, “Circularly polarized x-ray scattering inves-

- tigation of spin-lattice coupling in TbMnO_3 in crossed electric and magnetic fields,” *Physical Review B*, vol. 88, p. 214415, Dec. 2013.
- [87] W. Sławiński, R. Przeniosło, I. Sosnowska, M. Bieringer, I. Margiolaki, and E. Suard *Acta Crystallographica Section B Structural Science*, vol. 65, pp. 535–542, Oct. 2009.
- [88] C. C. Homes *Appl. Opt.*, vol. 32, p. 2976, 1993.
- [89] M. N. Iliev, M. V. Abrashev, H.-G. Lee, V. N. Popov, Y. Y. Sun, C. Thomsen, R. L. Meng, and C. W. Chu, “Raman spectroscopy of orthorhombic perovskitelike YMnO_3 and LaMnO_3 ,” *Physical Review B*, vol. 57, no. 5, pp. 2872–2877, 1998.
- [90] M. N. Iliev, V. G. Hadjiev, M. M. Gospodinov, R. P. Nikolova, and M. V. Abrashev, “Raman study of phonons in $\text{CaMn}_7\text{O}_{12}$: Effects of structural modulation and structural transition,” *Physical Review B*, vol. 89, p. 214302, June 2014.
- [91] M. Balkanski, R. F. Wallis, and E. Haro, “Anharmonic effects in light scattering due to optical phonons in silicon,” *Physical Review B*, vol. 28, no. 4, p. 1928, 1983.
- [92] M. N. Iliev and M. V. Abrashev, “Raman phonons and Raman Jahn-Teller bands in perovskite-like manganites,” *Journal of Raman Spectroscopy*, vol. 32, pp. 805–811, Oct. 2001.
- [93] A. Nonato, B. S. Araujo, A. P. Ayala, A. P. Maciel, S. Yanez-Vilar, M. Sanchez-Andujar, M. A. Senaris-Rodriguez, and C. W. A. Paschoal, “Spin-phonon and magnetostriction phenomena in $\text{CaMn}_7\text{O}_{12}$ helimagnet probed by Raman spectroscopy,” *Applied Physics Letters*, vol. 105, p. 222902, Dec. 2014.
- [94] R. Shannon, “Revised effective ionic radii and systematic studies of interatomic distances in halides and chalcogenides,” *Acta. Cryst.*, vol. A32, pp. 751–767, 1976.
- [95] F. Mezzadri, M. Calicchio, E. Gilioli, R. Cabassi, F. Bolzoni, G. Calestani, and F. Bissoli, “High-pressure synthesis and characterization of $\text{PrMn}_7\text{O}_{12}$ polymorphs,” *Physical Review B*, vol. 79, p. 014420, Jan. 2009.

- [96] R. Clark and J. reid, “The analytical calculation of absorption in multifaceted crystals,” *Acta Crystallogr. A*, vol. 51, pp. 887–897, 1995.
- [97] *CrysAlis PRO. Agilent Technologies Ltd, Yarnton, England.*
- [98] O. Dolomanov, L. Bourhis, R. Gildea, J. Howard, and H. Puschmann *Appl. Crystallogr.*, vol. 42, pp. 339–341, 2009.
- [99] G. Sheldrick *Acta Cryst.*, vol. A71, pp. 3–8, 2015.
- [100] K. Gautam, D. K. Shukla, S. Francoual, J. Bednarcik, J. R. L. Mardegan, H.-P. Liermann, R. Sankar, F. C. Chou, D. M. Phase, and J. Stremper, “Large negative thermal expansion in the cubic phase of $\text{CaMn}_7\text{O}_{12}$,” *Physical Review B*, vol. 95, p. 144112, Apr. 2017.
- [101] B. Bochu, J. Buevoz, J. Chenavas, A. Collomb, J. Joubert, and M. Marezio, “Bond length in $\text{CaMn}_3\text{Mn}_4\text{O}_{12}$: A new jahn-teller distortion of Mn^{3+} octahedra,” *Solid state communications*, vol. 36, pp. 133–138, 1980.
- [102] H. Etani, I. Yamada, K. Ohgushi, N. Hayashi, Y. Kusano, M. Mizumaki, J. Kim, N. Tsuji, R. Takahashi, N. Nishiyama, T. Inoue, T. Irifune, and M. Takano, “Suppression of Intersite Charge Transfer in Charge-Disproportionated Perovskite $\text{YCu}_3\text{Fe}_4\text{O}_{12}$,” *Journal of the American Chemical Society*, vol. 135, no. 16, pp. 6100–6106, 2013.
- [103] I. V. Solovyev, M. V. Valentyuk, and V. V. Mazurenko, “Magnetic structure of hexagonal YMnO_3 and LuMnO_3 from a microscopic point of view,” *Physical Review B*, vol. 86, p. 054407, Aug. 2012.
- [104] J. Hopkinson, “Magnetic and other physical properties of iron at a high temperature,” *Philosophical transactions of the Royal Society of London*, vol. A180, pp. 443–465.
- [105] T. Locherer, R. Dinnebier, R. Kremer, M. Greenblatt, and M. Jansen, “Synthesis and properties of a new quadruple perovskite: A-site ordered $\text{PbMn}_3\text{Mn}_4\text{O}_{12}$,” *Journal of Solid State Chemistry*, vol. 190, pp. 277–284, June 2012.

- [106] Y. S. Glazkova, N. Terada, Y. Matsushita, Y. Katsuya, M. Tanaka, A. V. Sobolev, I. A. Presniakov, and A. A. Belik, “High-Pressure Synthesis, Crystal Structures, and Properties of $\text{CdMn}_7\text{O}_{12}$ and $\text{SrMn}_7\text{O}_{12}$ Perovskites,” *Inorganic Chemistry*, vol. 54, pp. 9081–9091, Sept. 2015.
- [107] D. Delmonte, F. Mezzadri, C. Pernechele, G. Calestani, G. Spina, M. Lantieri, M. Solzi, R. Cabassi, F. Bolzoni, A. Migliori, C. Ritter, and E. Gilioli, “Thermally activated magnetization reversal in bulk $\text{BiFe}_{0.5}\text{Mn}_{0.5}\text{O}_3$,” *Physical Review B*, vol. 88, no. 1, p. 014431, 2013.
- [108] M. Verseils, F. Mezzadri, D. Delmonte, B. Baptiste, Y. Klein, S. Shcheka, L. C. Chapon, T. Hansen, E. Gilioli, and A. Gauzzi, “Effect of chemical pressure induced by the $\text{La}^{3+}/\text{Y}^{3+}$ substitution on the magnetic ordering of $(\text{AMn})_3\text{Mn}_4\text{O}_{12}$ quadruple perovskites,” *Physical Review Materials*, December 2017. To be published.
- [109] N. Terada, Y. S. Glazkova, and A. A. Belik, “Differentiation between ferroelectricity and thermally stimulated current in pyrocurrent measurements of multiferroic $\text{MMn}_7\text{O}_{12}$ ($\text{M} = \text{Ca}, \text{Sr}, \text{Cd}, \text{Pb}$),” *Physical Review B*, vol. 93, p. 155127, Apr. 2016.
- [110] R. Ramesh and N. A. Spaldin, “Multiferroics: progress and prospects in thin films,” *Nature materials*, vol. 6, no. 1, pp. 21–29, 2007.
- [111] R. Cabassi, F. Bolzoni, A. Gauzzi, E. Gilioli, A. Prodi, and F. Licci, “Dielectric properties of doping-free $\text{NaMn}_7\text{O}_{12}$: Origin of the observed colossal dielectric constant,” *Physical Review B*, vol. 74, p. 045212, July 2006.
- [112] L. Balents, “Spin liquids in frustrated magnets,” *Nature*, vol. 464, pp. 199–208, Mar. 2010.
- [113] A. P. Ramirez, “Strongly geometrically frustrated magnets,” *Annual Review of Materials Science*, vol. 24, no. 1, pp. 453–480, 1994.

Remerciements

Cette thèse a été réalisée en cotutelle entre l'institut de minéralogie, de physique des matériaux et de cosmochimie (IMPMC) de l'université Pierre et Marie Curie et l'istituto dei materiali per l'elettronica ed il magnetismo (IMEM-CNR) à l'université de Parma. Ce projet européen a été possible grâce au financement "Leonardo da Vinci" de l'université Franco-Italienne que je tiens à remercier. Je remercie Guillaume Fiquet et Salvatore Iannotta, les directeurs des deux laboratoires, de m'avoir accueillie.

Je remercie Andrea de m'avoir donné l'opportunité de faire une thèse et de m'avoir transmis sa passion pour la recherche. Je le remercie pour sa disponibilité et son soutien et surtout pour l'optimisme qu'il a su insuffler à chacune de nos discussions. Je le remercie aussi d'avoir eu l'idée de m'envoyer à Parme!

Ringrazio Edi per avermi accolto durante quest'anno parmigiano e di avermi fatto scoprire i misteri delle sintesi ad alta pressione. Grazie di avermi sostenuto durante tutto il mio dottorato. Grazie anche di aver accettato la stuffeta in ufficio e mi scuso se non ti ho insegnato bene il francese !

Un grand merci à Benoit pour les heures qu'il a passées à essayer de trouver la structure des mes échantillons bizarres ! Merci à Christophe pour les jours et les nuits passées au Raman à essayer de trouver du signal !

Un merci tout particulier à Paola, ma maman du Labo, pour sa gentillesse et ses conseils précieux. Merci à Ricardo L de nous avoir ouvert son labo et merci aussi pour son humour décapant !

Un ringraziamento speciale a Dédé e Francesco per il loro insostituibile aiuto scientifico e personale. Dédé ti ringrazio per la tua pazzia che mi ha fatto tanto ridere e Francesco per la pazienza con la quale hai sempre risposto alle domande compulsive che ti mandavo via skype (grazie anche per la ricetta dei gnocchi) !

Ringrazio particolarmente Fulvio e Riccardo per il loro aiuto nel progetto. Grazie a Fulvio per le gare in bici andando all' IMEM la mattina !

Grazie a tutti gli altri che hanno fatto dell' IMEM un posto gradevole dove lavorare anche se i soldi non ci sono... Cito tra altri: L'Eli, Il Bronz, Il Zamb, Il Ben, Maurizio, Manu, Il Coppe, Zappettini, Il Cale, La Giulia, Paola, Filippo, Marco, Martina, Francesco B, Stefano, Francesco P, Luca...

Grazie a tutti gli altri amici che ho incontrato durante quest'anno meraviglioso: Claudia e Andrea i miei romani preferiti, Claudia L, Luciana, Angela, Domna, Pietro, Gaetano, Nicola C...

Je remercie enfin tous les non-permanents de l'IMPMC pour leur amitié et le soutien moral qu'ils m'ont apporté au cours des nombreux repas à la cafet autour d'une assiette de graines: Sara L, Louisiane, Niéli, Sara R, Aisha, Nicolas, David, Johan, Andrea, Mario, Edoardo, Julie, Maud, Mélanie, Zailan, Haiwa, Vinícius. Merci à Blair pour son aide en programmation python.

Je remercie également ma famille et mes amis qui partagent mon quotidien. Je remercie tout particulièrement mes parents qui m'ont donné le goût d'apprendre et ont toujours cru en moi. Je remercie ma sœur qui est toujours persuadée que je découvre des choses extraordinaires ! Enfin je remercie Aladdin qui me supporte tous les jours et qui m'a soutenue sans réserve du premier jour où je lui ai annoncé que je partais en Italie au dernier jour où je lui demandais de quitter la pièce pour pouvoir répéter mon oral ...

Paris, Vendredi 17 Novembre 2017

Marine Verseils